A model integrating satellite-derived shoreline observations for predicting fine-scale shoreline response to waves and sea-level rise across large coastal regions

Sean Vitousek[1,2], Kilian Vos[3], Kristen D. Splinter [3], Li Erikson[1], and Patrick L. Barnard[1]

Author Affiliations

1. U.S. Geological Survey
2. University of Illinois at Chicago
3. UNSW Sydney

Abstract

Satellite-derived shoreline observations combined with dynamic shoreline models enable fine-scale predictions of coastal change across large spatiotemporal scales. Here, we present a satellite-data-assimilated, "littoral-cell"-based, ensemble Kalman-filter shoreline model to predict coastal change and uncertainty due to waves, sea-level rise, and other natural and anthropogenic processes. We apply the developed ensemble model to the entire California coastline (approximately 1,350 km), much of which is sparsely monitored with traditional survey methods (e.g., Lidar/GPS). Water-level-corrected, satellite-derived shoreline observations (obtained from the CoastSat toolbox) offer a nearly unbiased representation of in-situ surveyed shorelines (e.g., Mean Sea Level elevation contours) at Ocean Beach, San Francisco. We demonstrate that model calibration with satellite observations during a 20-year hindcast period (1995 to 2015) provides a nearly equivalent model forecast accuracy during a validation period (2015 to 2020) compared to model calibration with monthly in-situ observations at Ocean Beach. When comparing model-predicted shoreline positions to satellite-derived observations, the model

achieves an accuracy of <10 m RMSE for nearly half of the entire California coastline for the validation period. The calibrated/validated model is then applied for multi-decadal simulations of shoreline change due projected wave and sea-level conditions while holding the model parameters fixed. By 2100, the model estimates that 25 to 70% of California's beaches may become completely eroded due to sea-level rise scenarios of 0.5 to 3.0 m, respectively. The satellite-data-assimilated modeling system presented here is generally applicable to a variety of coastal settings around the world owing to the global coverage of satellite imagery.

Plain Language Summary (PLS)

We present a computer model to predict shoreline change due to waves, sea-level rise, and other local processes. We apply the model to the entire California coastline (approximately 1,350 km), much of which is not well monitored using traditional survey methods. Observations of historical shoreline position obtained from satellite images can be used in lieu of traditional shoreline survey data to estimate erosion/accretion trends as well as to calibrate and validate models. By 2100, the model estimates that 25 to 70% of California's beaches may become completely eroded due to sea-level rise scenarios of 0.5 to 3.0 m, respectively.

1. Introduction

Accurate predictions of coastal erosion in response to sea-level rise, changing wave conditions, and reduced natural sediment supplies are increasingly sought by coastal managers to assess the impacts of climate change on beaches (Masselink et al., 2016; Vitousek et al., 2017a; Le

Cozannet et al., 2019). Several well-tested and emerging models are capable of simulating coastal erosion (Roelvink, 2011; Montaño et al., 2020; Toimil et al., 2020a, Ranasinghe 2020, Hunt et al., 2023). However, most models inherently capture a limited number of processes occurring at a narrow geographic scope, because of computational or data availability constraints. Although there are many different paradigms of coastal evolution models, two main classifications often emerge: (1) physics-based numerical models and (2) reduced-complexity (or process-based) models. On the one hand, physics-based models numerically solve equations of conservation of mass and momentum of fluid and sediment with the aim to resolve all (or nearly all) of the important oceanographic/hydrodynamic processes resulting in sediment transport and coastal change. However, the high computational effort of physics-based models often hinders simulation of large-scale (e.g., 100's m to 100 km) or long-term (e.g., annual and longer) coastal change. On the other hand, reduced-complexity models (Murray 2007) seek to parameterize a limited number of dominant coastal-change processes or trends, usually without explicitly resolving the underlying hydrodynamic processes responsible for sediment transport. The biggest drawback of reduced-complexity models is that they generally require observational data to parameterize, calibrate, and/or validate the model (Vitousek et al., 2017; Montaño et al., 2020), at least when used in a predictive sense rather than an exploratory sense (Murray et al., 2016). Although they do not explicitly resolve all relevant physical processes, data-driven reduced-complexity models can often implicitly account for the most dominant processes via calibration to local observations (Vitousek et al., 2017). However, time series of coastal-change observations over multiple years are often sparse or narrow in geographic scope.

The field of coastal morphodynamics has, until recently, been 'data poor,' with long-term monitoring data existing only at a limited number sites (Vitousek et al., 2022). However,

reliable forecasts of coastal erosion on decadal to centennial timescales over large geographic regions (e.g., state and country scale) are increasingly sought, even in 'data-poor' environments. Recent progress has been made to improve the temporal frequency of coastal observations over large spatiotemporal scales (e.g., 1 m - 100 km and days - decades) using satellites (Pardo-Pascual et al., 2012; Hagenaars et al., 2017; Luijendijk et al., 2018; Vos et al., 2019a,b; Nelson & Miselis, 2019, Vos et al., 2023). Since the 1980's, Earth-observing satellites (e.g., the Landsat missions) have collected a massive archive of coastal imagery data that have only recently been leveraged for science and engineering applications (Turner et al., 2021). Recent advances in satellite remote-sensing analysis provide a window into the recent past and current state of the world's beaches (Luijendijk et al., 2018) and their large-scale vulnerability to climatic forces like El Niño (Vos et al., 2023). By leveraging the large streams of data offered from satellites, reduced-complexity coastal-change models seem poised for success in a challenging field of study owing to the newly found 'treasure trove' of data (Hunt et al., 2023, Vitousek et al., 2023, Barnard & Vitousek 2023).

For more than two decades, satellite-data have been effectively assimilated into predictive atmosphere and ocean models (e.g., ERA5 – Hersbach et al., 2020 and CFSR – Saha et al., 2010). Yet, integration of satellite-data with large-scale, dynamic coastal-change models have remained underdeveloped, until now. Most applications of satellite-derived shorelines investigate shoreline trends (e.g., Luijendijk et al., 2018, Calkoen et al., 2021, Castelle et al., 2022) or interannual variability (Vos et al., 2023), rather than synoptic shoreline variability with wave and storm events. Recently, Alvarez-Cuesta et al., (2021a,b) integrated satellite-derived across 40 km of the Spanish Mediterranean Coast into a dynamic shoreline model. Similarly, in this paper, we demonstrate how decades of satellite imagery can be leveraged to accurately

calibrate and validate coastal evolution models, enabling predictions/projections of coastal change in historically data-poor environments over vast geographic scales.

2. Methods

2.1 Shoreline model

The shoreline-change model, used here, is an update of CoSMoS-COAST (Vitousek et al., 2017; Vitousek et al., 2021), a transect-based, data-assimilated 'one-line' model that integrates longshore and cross-shore transport processes. The CoSMoS-COAST model was initially developed as the long-term shoreline change component of the USGS Coastal Storm Modeling System (CoSMoS; Barnard et al., 2014), and the model's novel developments as part of the current work are presented in Figure 1. In summary, the notable and novel aspects of the current work include: (1) integration with satellite-derived shorelines [which provides nearly a thousand-fold increase in assimilation data over the previous iteration in Vitousek et al., (2017)], (2) the development of a novel "littoral-cell based" data-assimilation method (detailed in Appendix B), and (3) projections across the entire state of California (approximately 1,350 km) compared to the previous iteration in Vitousek et al., (2017), which spanned only 500 km of southern California.

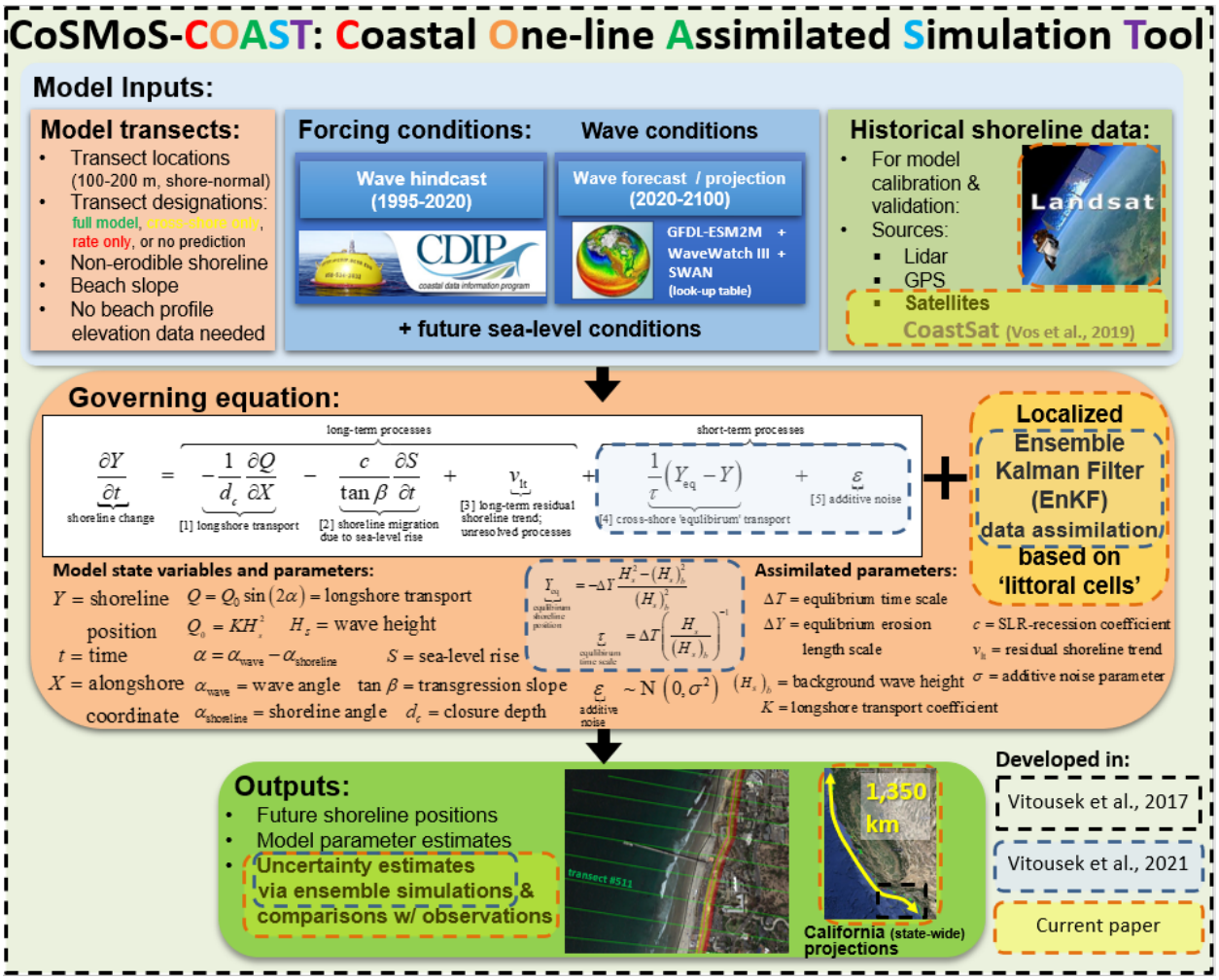

Figure 1 – An overview of the CoSMoS-COAST model, including the model inputs/outputs, variables/parameters, and governing equation for the current application in California. The figure also depicts advancements in the model from its initial development (Vitousek et al. 2017 – black dashed lines) to Vitousek et al., 2021 (blue dashed lines) and to the current paper (orange dashed lines).

2.1.1 Model governing equation

The model governing equation, which is based on the one-dimensional conservation of sediment volume in the alongshore direction and initially developed in Vitousek et al., (2017, 2021), is given by

$$\underbrace{\frac{\partial Y}{\partial t}}_{\text{shoreline change}} = \overbrace{\underbrace{-\frac{1}{d_c}\frac{\partial Q}{\partial X}}_{\text{[1] longshore transport}} - \underbrace{\frac{c}{\tan\beta}\frac{\partial S}{\partial t}}_{\text{[2] shoreline migration due to sea-level rise}} + \underbrace{v_{\text{lt}}}_{\text{[3] long-term residual shoreline trend; unresolved processes}}}^{\text{long-term processes}} + \overbrace{\underbrace{\frac{1}{\tau}\left(Y_{\text{eq}} - Y\right)}_{\text{[4] cross-shore 'equlibirum' transport}}}^{\text{short-term processes}} + \underbrace{\varepsilon}_{\text{[5] additive noise}} \quad (1)$$

Each term in Eq. (1) is defined in Figure 1 and detailed in Appendix A, alongside the presentation of numerical methods to solve Eq. (1). In brief, Eq. (1) synthesizes several popular individual-process models including: [1] a 'one-line' model for longshore transport (Pelnard-Considere, 1956); [2] a cross-shore beach profile change model due to sea-level rise (Bruun, 1962; Davidson-Arnott, 2005; Anderson et al., 2015); [3] a long-term residual shoreline trend v_{lt} that represents long-term processes like sources and sinks of sediment, e.g., fluvial inputs, headland bypassing, beach nourishments, etc., which is estimated via assimilation of local shoreline observations; [4] a wave-driven cross-shore equilibrium shoreline change model that has been modified (without changing the underlying dynamics) from Yates et al., (2009), as discussed in Vitousek et al., (2021); and finally [5] a noise term. Here, the noise term represents (normally distributed) random, short-term, unresolved processes that cause fluctuations in shoreline position with zero mean and user-prescribed standard deviation σ. The model includes an ensemble Kalman filter data-assimilation method based on 'littoral cells' (discussed below and detailed in Appendix B) that sequentially adjusts the model parameters (given in Figure 1) to best match local observations at each time step (when data are available).

2.1.2 Model transects and littoral-cell-based data assimilation

The California model is comprised of 11,539 transects spaced approximately 100-200 m apart (see Figure 2). Each transect is designated as either "full model", "cross-shore only", "rate only", "cliff only" or "no prediction" based on geologic characteristics (which occur for 31.9%,

18.2%, 30.6%, 12%, and 7.3% of the California coastline, respectively). Based on the transect designation, the shoreline model retains or neglects certain physical processes and the corresponding terms in the governing equation, Eq. (1), as described in Appendix A.2. For example, "cross-shore only" transects neglect term [1] in Eq. (1), and "rate only" transects neglect terms [1] and [4].

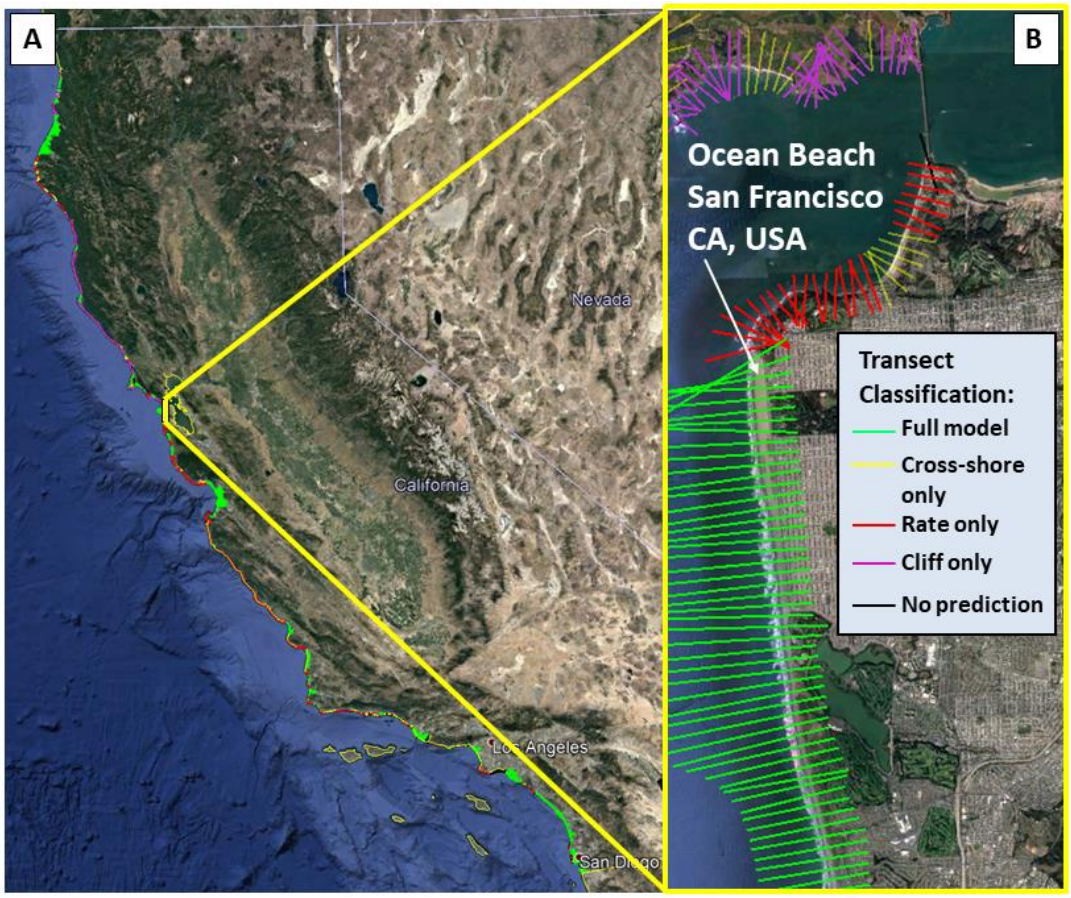

Figure 2 – The (~100-200 m spaced) model transects for the coast of California shown in panel A. Panel B shows a zoomed-in plot of the transects at Ocean Beach, San Francisco. Transects that are designated as "full model", "cross-shore only", "rate only", "cliff only", and "no prediction" are shown in green, yellow, red, purple, and black, respectively. (Basemaps from Google Earth).

148 The model transects are grouped into so-called ‘littoral cells’, which represent the basis for the
149 novel data-assimilation method, which is fully detailed in Appendix B. The grouping of
150 transects into littoral cells can be either user-specified or done automatically, by grouping all
151 neighboring transects with the same transect designation into a littoral cell (i.e., all adjacent “full
152 model” transects constitute a littoral cell), as is done here. The original data-assimilation method
153 used in CoSMoS-COAST (Vitousek et al. 2017) operated independently for each transect;
154 meaning that any transects without coincident (e.g., intersecting) shoreline observations did not
155 receive any parameter adjustments. The current littoral-cell based data-assimilation method uses
156 all observations within a littoral cell (at a given time step) to assimilate the model parameter
157 values for all transects within that littoral cell (while simultaneously prioritizing the influence of
158 local observations at each transect). This littoral-cell based method provides some significant
159 advantages over individual-transect method, which primarily stem from using more assimilation
160 data and allowing those data to have a greater spatial influence on nearby transects. For
161 example, the new method facilitates assimilation of sparsely spaced beach-profile data (e.g.,
162 from GPS or total-station surveys) onto more densely spaced model transects. Further
163 advantages and the technical details of the littoral-cell based data-assimilation method are
164 discussed in Appendix B.

165 *2.1.3 Model forcing and scenarios*

166 Shoreline evolution is often critically linked to oceanographic forcing from waves and sea level
167 (Wright & Short 1984, Ashton et al., 2001, Splinter et al., 2014, Troy et al., 2021). Hence,
168 reliable shoreline modeling generally demands accurate hindcasts and robust projections of wave
169 and sea-level conditions. As shown in Figure 1, the model is forced by time series of parametric

wave conditions (i.e., H_s, T_p, and θ) and sea-level rise, S. In the current application, historic wave conditions (1995-2020) are derived primarily from the CDIP hindcast (O'Reilly et al., 2016), whereas projected wave conditions (2020-2100) are derived from a regional-to-local nested WaveWatch III model (Erikson et al., 2015), which applies wind forcing from the GFDL-ESM2M climate model (Delworth et al., 2006). Sea-level projections are generated from quadratic curves (following Vitousek et al., 2017), which cover a range of physically tenable sea-level outcomes (e.g., 0.5, 0.75, 1.0, 1.25, 1.5, 1.75, 2.0, 2.5, and 3.0 m) in California over the 21st century (e.g., Griggs et al., 2017, Sweet et al., 2022). The specific details on the wave and sea-level forcing conditions are presented in Appendix C.1 and C.2, respectively.

Anthropogenic effects on coastal change are difficult to represent using models. Humans make deliberate, real-time interventions (e.g., beach nourishments, dredging/dumping, bulldozing/berm-building, temporary shoreline armoring) in the coastal zone, especially during major storm events – yet, practically all existing shoreline models do not explicitly account them (Lazarus & Goldstein 2019). However, fine-scale observations (e.g., such as those provided from satellites) offer a means to implicitly account for anthropogenic effects in the context of a data-driven model, at least in so much as their impact is reflected in the local shoreline behavior and observations thereof. Thus, the estimation of long-term residual shoreline trends such as v_{lt} in Eq. (1) via data assimilation provides a means of accounting for processes that are difficult, if not impossible, to account for explicitly.

As in Vitousek et al., (2017), the model considers two binary (i.e., on or off) management scenarios: called the 'hold the line' and 'continued accretion'. The 'hold the line' versus 'no hold the line' scenarios prohibit or allow the modeled shoreline to erode past a so-called 'non-

erodible shoreline' (detailed in Appendix C.3) that delineates the location of non-sandy substrates such as infrastructure, coastal cliffs, or vegetation. The 'continued accretion' versus 'no continued accretion' scenarios allow or prevent the persistence of residual accretion trends ($v_{lt} > 0$), respectively. Justification and further details on the coastal management scenarios used here are given in Appendix C.3.

2.2 Quantifying model performance and uncertainty

Quantifying model performance and uncertainty remains a critical effort in pursuit of reliable coastal-change predictions. In general, methods to assess model performance and uncertainty quantification are somewhat tailored to the model type, e.g., 'simulation' versus 'exploratory' (Murray et al., 2016). 'Simulation' models typically seek to reproduce site-specific behavior and thus generally require characterization of model performance (e.g., compared to observations). Idealized, 'exploratory' models often seek to address uncertainty related to climate scenarios or to the magnitude and/or parametrization of processes or factors (for which direct observations are often lacking). The current modeling application combines elements from both of the 'simulation' and 'exploratory' archetypes: we seek the long-term simulation/prediction of site-specific behavior under different climate and management scenarios. Hence, to align with the simulation archetype, we apply a suite of methods to evaluate model performance and uncertainty, as described below.

2.2.1 Model performance

The most common metric to evaluate model performance is the root-mean-square error (RMSE), which is given by

$$\varepsilon_{\mathrm{RMSE}} = \sqrt{\frac{1}{N}\sum_{i=1}^{N}\left(\left(Y_{\mathrm{obs}}\right)_i - \left(Y_{\mathrm{mod}}\right)_i\right)^2} \tag{2}$$

where Y_{mod} and Y_{obs} are the modeled and observed shoreline positions, respectively, among a time series of N data points.

Another popular model-performance metric is the index of agreement (Willmott 1981), which is given by

$$d = 1 - \frac{\sum_{i=1}^{N}\left(\left(Y_{\mathrm{mod}}\right)_i - \left(Y_{\mathrm{obs}}\right)_i\right)^2}{\sum_{i=1}^{N}\left(\left|\left(Y_{\mathrm{mod}}\right)_i - \overline{\left(Y_{\mathrm{obs}}\right)_i}\right| + \left|\left(Y_{\mathrm{obs}}\right)_i - \overline{\left(Y_{\mathrm{obs}}\right)_i}\right|\right)^2} \tag{3}$$

where the overbar indicates the mean of a quantity. The index of agreement ranges from $0 \le d \le 1$, with values close to zero indicating poor and values close to one indicating excellent performance. The index of agreement was recently used by Montaño et al., (2020) to evaluate the performance of shoreline models in a blind-test competition (at the test site of Tairua Beach, New Zealand with 15 years of calibration data and 3 years of data-blind comparisons), and the best performing shoreline models achieved $d \approx 0.5$ - 0.7. As shown in Results, we assess model-performance metrics including the RMS error ($\varepsilon_{\mathrm{RMSE}}$) and the index of agreement (d), across California with the aid of satellite-derived shoreline observations. We also characterize different types of model uncertainty including structural, epistemic, and intrinsic uncertainty, as described below.

2.2.2 Model uncertainty

Several recent studies have investigated the uncertainty associated with individual (Davidson et al. 2013; Kroon et al., 2020, Zarifsanayei et al., 2021) or combined components (Banno et al., 2015, Le Cozannet et al. 2019; D'Anna et al., 2020, 2021a, 2022, Vitousek et al., 2021, Toimil et al., 2017, 2021) of popular shoreline models (such as those described by processes/terms in Eq. (1)). From these studies, consensus emerges that: (1) waves generally dominate uncertainties at short time scales and sea-level-driven recession or persistent shoreline accretion/erosion trends dominate uncertainties at long time scales, (2) intrinsic uncertainty (e.g., due to unknown model forcing conditions, like scenarios of future wave and sea-level conditions) is generally irreducible unlike epistemic uncertainty (e.g., due to unknown/uncertain model parameters), which is reducible via refining model parameters (using data-assimilation, for example), and (3) climate-driven intrinsic uncertainties (e.g., due to cascading uncertainties in greenhouse gas emissions, global temperature projections, future wave and sea-level conditions and different GCM projections thereof, future sediment supplies, and future coastal management pathways) are both broad and deep (Toimil et al., 2020b).

In the current approach, we investigate the model's epistemic, intrinsic, and structural uncertainty, as described below. Firstly, we address epistemic/parametric uncertainty via applying a range of model parameters in an ensemble simulation and use data assimilation to calibrate site-specific values of model parameters over a large scale, with the aid of large amounts of satellite-derived shoreline observations (described below). Following Vitousek et al. (2021), we also address epistemic uncertainty of the model solution/parameters by applying a calibrated additive-noise parameter σ (which is part of term [5] in Eq. (1) and is described in

Section 2.1). Secondly, we assess intrinsic uncertainty by applying different sea-level and coastal-management scenarios, as described above and in Appendix C. We also assess wave-driven intrinsic/aleatoric uncertainty associated with extreme storm-driven erosion due to annual, 20-year, and 100-year return period wave events, by fitting generalized extreme value (GEV) distributions to annual minima in the wave-driven, cross-shore equilibrium shoreline position, following Davidson et al. (2017) as detailed in Appendix C.1. Thirdly, we investigate the model's structural uncertainty, defined as the inadequacy, bias, or discrepancy between the model and the real world (i.e., observations). The structural uncertainty (which we also refer to as the uncertainty due to 'unresolved processes') is, philosophically, a bit different than the intrinsic or epistemic uncertainty. On the one hand, the intrinsic and epistemic uncertainties represent the model's interpretation of how inaccurate *it might be* given different forcing conditions or parameters, respectively. On the other hand, the structural uncertainty is how inaccurate the model *actually is*, compared with real-world observations. We also note that investigating the structural uncertainty is rare among large-scale shoreline modeling applications, due to data-availability constraints. Here, we investigate structural uncertainty by comparing the model to satellite-observed shorelines across California during the validation period of 2015-2020. We report the model structural uncertainty using the common and conservative approach of reporting $\pm 2\varepsilon_{\mathrm{RMSE}}$ (a.k.a., two-sigma) confidence bands surrounding the model's median projections, which seeks to contain ~ 95% of the possible variations, following Taylor & Kuyatt (1994).

2.3 Satellite-derived shoreline observations

The most intensive local monitoring programs in California have performed ~200 topographic beach surveys over the last two decades (e.g., Barnard et al., 2012, Young et al., 2021), yet satellite imagery can typically provide 500-1000 shoreline observations spanning almost four decades, at any given beach. Here, we apply the CoastSat toolbox (Vos et al., 2019a) to derive historical shoreline observations from individual, cloud-free satellite images in the Landsat archive. The satellite-derived, historical shoreline position data used as part of this study are available via Vos (2022) [data set]. Although historical Lidar and GPS data are also assimilated in the model, these CoastSat-derived shoreline observations represent the vast majority (i.e., 99.9%) of assimilated data, which is described further in Appendix B.

2.3.1 CoastSat

The CoastSat image-processing methodology, used in the current application, derives shoreline position using the marching-squares algorithm (Lorensen & Cline 1987) that contours the threshold of the Modified Normalized Difference Water Index (MNDWI) that optimally splits the image-segmentation classes of 'water' and 'sand' using Otsu's (1979) method (as detailed in Vos et al., 2019a). CoastSat also provides methodology to estimate beach-face beach slopes (based on Vos et al., 2020), which are subsequently used to correct satellite-derived observations for tidal stage (e.g., using Eq. (4)). CoastSat has been validated against traditional shoreline surveys in a variety of coastal settings worldwide including Truc Vert, France; Moruya, Australia; Narrabeen-Collaroy, Australia; Tairua, New Zealand; Duck, North Carolina, United States, and generally provides accuracy (i.e., root-mean-square error) on the order of 7-14 meters (Vos et al., 2019b) compared with in-situ surveys. For the current application, we compare

CoastSat-derived shoreline observations against in-situ GPS surveys at Ocean Beach, San Francisco, California, U.S., a well-monitored site with over 200 monthly surveys since 2004 (Hansen and Barnard, 2010; Barnard et al., 2012). Here, we compare the accuracy of satellite-derived shoreline positions to the 'ground-truthed' GPS surveys of centimeter-scale accuracy. The primary difference between the GPS versus satellite-derived shoreline data sets is that the latter is based on a visual-detection proxy for the shoreline that is influenced by the local water level, whereas the GPS surveys are elevation-based (or datum-based) and thus are independent of the local water level. Below and in Appendix D, we address differences between GPS- versus satellite-derived shorelines and the so-called 'proxy-datum bias' (Moore et al., 2006; Ruggiero & List, 2009), respectively.

The shoreline positions in both GPS and satellite data sets at Ocean Beach are measured as the distance Y from a fixed onshore baseline to the location of the mean sea-level (MSL) elevation contour. Although more surveyed shoreline contours (e.g., mean high water - MHW) can be extracted from the GPS-derived elevation point-cloud data available at Ocean Beach, we use the MSL shoreline contour in order to maintain consistency with the satellite-derived water line. In both data sets, observations over ~5 km of beach are interpolated onto shore-perpendicular model transects spaced approximately 200 m in the alongshore direction.

As discussed in Appendix C, we find that CoastSat-derived MSL shorelines at Ocean Beach are generally biased landward of the GPS-derived MSL shorelines, and that the shoreline error ($Y_{\mathrm{GPS}} - Y_{\mathrm{sat}}$), is highly correlated with wave height (as shown in Figure 21 in Appendix D). This finding suggests that the satellite-derived shoreline positions are affected by wave setup (i.e., the persistent elevation of nearshore water levels inshore of breaking waves), which causes a

landward shift of the identified water-line/shoreline, and which might be bias-corrected with knowledge of synoptic wave conditions, wave setup elevation, and foreshore beach slope.

2.3.2 Tide, wave-setup, and residual water-level correction to satellite-derived shorelines

To remove bias due to synoptic water-level conditions, we correct the satellite-derived shoreline position along each transect according to

$$Y_{\text{corrected}}(t) = Y_{\text{raw}}(t) + \frac{1}{\beta_f}\underbrace{\left(\underbrace{\eta_{\text{tide}}(t)}_{\substack{\text{[1] tide}\\ \text{correction}}} + \underbrace{\bar{\eta}(t)}_{\substack{\text{[2] wave setup}\\ \text{correction}}} + \underbrace{\eta_{\text{MMSLA}}(t)}_{\substack{\text{[3] montly mean}\\ \text{sea-level}\\ \text{anomaly}\\ \text{correction}}} + \underbrace{\eta_{\text{opt}}}_{\substack{\text{[4] residual}\\ \text{correction}}}\right)}_{\text{the total, nearshore still-water level}} \quad (4)$$

where each (time-varying) correction component is due to different processes affecting the total, nearshore still-water level, including [1] tide, [2] wave setup, [3] monthly mean sea-level anomalies, as well as [4] any remaining/residual bias. Corrections are made using Eq. (4) for each of the model's shore-normal transects with known, time-invariant foreshore beach slopes. At Ocean Beach, the beach slope $\beta_f = 1/28$ for all transects, which is estimated from Lidar data. Here, CoastSat's built-in tidal corrections (i.e., term [1] in Eq. (4)) come from time series of astronomic water-levels (η_{tide}) predicted using the Finite-Element Solution (FES14) ocean model (Lyard et al., 2021). Here, we apply CoastSat's built-in tidal corrections derived from the FES14 tide model rather than observed water levels (including water-level anomalies) from tide stations so that the method is applicable to sites/transects lacking nearby water-level observations. However, there are pros and cons (namely portability and accuracy, respectively) to utilizing modeled over observed water levels.

We correct for wave setup (term [2] in Eq. (4)) using the Stockdon et al., (2006) empirical parameterization of wave setup for dissipative beaches,

$$\bar{\eta} = 0.016\sqrt{H_0 L_0} \quad . \tag{5}$$

In Eq. (5), deep-water wave height (H_0) and wave period (T_0), from which wavelength $L_0 = \frac{gT_0^2}{2\pi}$ is calculated using linear wave theory, can come from model hindcasts or buoy records. In the accuracy analysis presented here in Figure 3, we use wave conditions from the San Francisco wave buoy (#46026), located 33 km offshore from Ocean Beach. We also tested slope-dependent wave-setup parameterizations (from Stockdon et al. (2006)), and the results (not shown) provided slightly less skill than the dissipative-beach-specific formulations. The time series of monthly mean sea-level anomalies (MMSLA), η_{MMSLA} term [3] in Eq. (4), comes from estimates from the NOAA Tides & Currents database's San Francisco tide-gauge station (#9414290) located approximately 6 km away from Ocean Beach. Finally, we estimate an optimal, 'best-fit' water-level correction (term [4] in Eq. (4)) of $\eta_{\mathrm{opt}} = 12.72$ cm, which is required for the satellite-derived shorelines to obtain unbiased estimates of shoreline position and is discussed further in Appendix D.

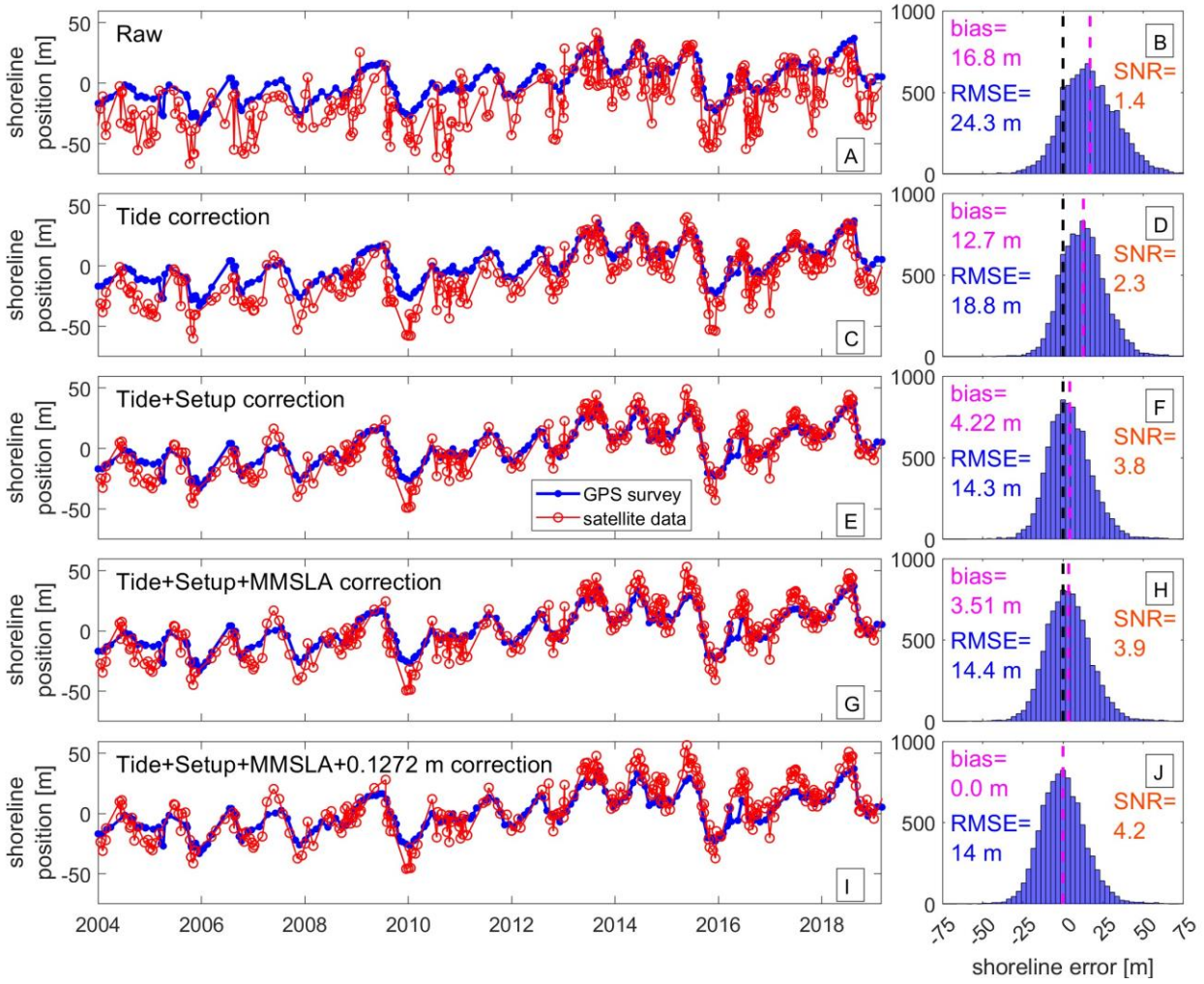

Figure 3 – The alongshore-averaged shoreline position with the (time-averaged) mean removed for the GPS surveys compared to the satellite-derived observations at Ocean Beach, San Francisco, California for different correction methods (i.e., different terms in Eq. (4)). Left panels show time series of comparisons, and right panels show the histogram of the error (GPS-derived minus satellite-derived shoreline position) as well as the bias, root-mean-square error (RMSE), and signal-to-noise ratio (SNR).

We compare a sequence of corrections (based on Eq. (4)) to the raw satellite-derived shoreline position compared with the GPS data in Figure 3. Panels A, C, E, G, and I on Figure 3 show the alongshore-averaged, satellite-derived shoreline position (red) compared to the alongshore-

averaged GPS shoreline position (blue) across the surveyed portion of Ocean Beach with different correction methods applied (which are described below). Note that the shoreline positions shown in Figure 3 are given relative to the mean of the time series. Panels B, D, F, H, and J on Figure 3 show histograms of the error in the shoreline position ($Y_{GPS} - Y_{sat}$) when using different correction methods. When calculating the shoreline error, the satellite-derived shoreline positions (collected approximately weekly, i.e., every 16 days across two overlapping Landsat missions) are linearly interpolated onto the dates of the (monthly) GPS surveys so that direct comparisons can be made. Figure 3 B demonstrates that the raw satellite-derived shoreline positions have a mean (landward) bias of 16.8 m and a root-mean-square error (RMSE) of 24.3 m. Both the bias and the RMSE are sequentially reduced each time a new correction term is applied (via Eq. (4)). After applying CoastSat's built-in tidal corrections, the (landward) bias of the satellite-derived shorelines is reduced to 12.7 m and the RMSE is reduced to 18.8 m (see Figure 3 C and D). Nevertheless, a fairly large bias remains. The ineffectiveness of the tidal correction on reducing the overall bias is perhaps expected. The tide oscillates somewhat evenly around mean sea level, and thus does not contribute significantly to the systematic landward bias of the satellite observations found here. Wave setup, on the other hand, represents a persistent still-water-level change that is likely responsible for much of the landward bias between the satellite's visual proxy interpretation of the shoreline position compared to the GPS's elevation-based (datum-based) interpretation of the shoreline position, which is uninfluenced by the presence of waves or the stage of the local water level. Figure 3 E and F show that correcting for time-varying wave setup (via term [2] in Eq. (4)) significantly reduces the bias of the satellite data from 12.7 to 4.2 m. However, the RMSE still remains sizable before (18.8 m) and after (14.3 m) the setup correction. Subsequent corrections for monthly mean sea-level anomalies

385 (MMSLA), observed at the San Francisco tide-gauge station (#9414290), do relatively little to
386 reduce the remaining bias (compare Figure 3 G and H). The residual landward bias of the
387 satellite-derived shoreline position can be completely eliminated by applying an additional
388 'water level' correction of $\eta_{\text{opt}} = 12.72$ cm, obtained via optimization. We believe that this static
389 correction between the GPS data and the satellite-derived data, corresponding to an effective
390 $\eta_{\text{opt}} = 12.72$ cm water-level difference or to a 3.5 m horizontal landward offset (as shown in
391 Figure 3 H), may represent the 'proxy-datum bias' between the visual and elevation-based
392 shoreline data (cf. Moore et al., 2006; Ruggiero & List, 2009) for Ocean Beach. As discussed
393 further in Appendix D and depicted in Figure 22, we believe that more than half of this
394 remaining bias is due to mismatches in modeled and observed water level.

395 After applying the full sequence of corrections in Eq. (4) to obtain an unbiased estimate of the
396 satellite-derived shoreline position, the RMSE of the satellite-derived shorelines is
397 approximately 14 m, which is equivalent to approximately half of the 30 m pixel resolution of
398 the Landsat imagery, which also closely resembles the 15 m pixel resolution of the pan-
399 sharpened Landsat imagery used in CoastSat. The level of accuracy, found here, is consistent
400 with numerous previous findings (e.g., Hagenaars et al., 2017, Luijendijk et al., 2018, Vos et al.,
401 2019a,b, Nelson & Miselis 2019).

402 In Figure 3 B, D, F, H, and J, we also report the signal-to-noise ratio (SNR), which is here
403 defined as the ratio of the variance of the satellite-derived shoreline 'signal' to the variance of the
404 'noise' (represented by the RMSE) and is given by

$$\mathrm{SNR} = \frac{\frac{1}{N}\sum_{i=1}^{N}\left(\left(Y_{\mathrm{sat}}\right)_i - \overline{Y_{\mathrm{sat}}}\right)^2}{\frac{1}{N}\sum_{i=1}^{N}\left(\left(Y_{\mathrm{GPS}}\right)_i - \left(Y_{\mathrm{sat}}\right)_i\right)^2} = \frac{\sigma_{\mathrm{SAT}}^2}{\varepsilon_{\mathrm{SAT}}^2} \quad (6)$$

We find, as shown in Figure 3, that the complete water-level correction method (described above) triples the signal-to-noise ratio from 1.3 for raw satellite-derived shorelines to 4.2 for the fully corrected shorelines. Furthermore, this analysis (stemming from Eq. (6)) shows that beaches that experience larger 'signals' of erosion and accretion will generally be more amenable to observation from satellites according to the SNR metric given here.

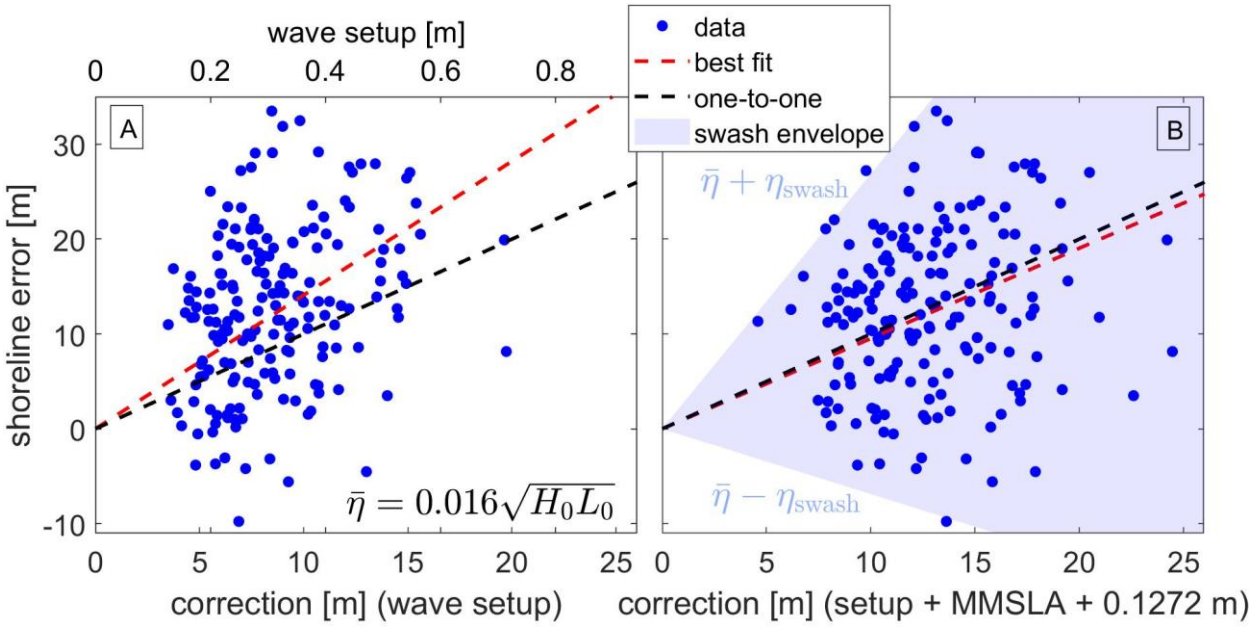

Figure 4 – The satellite-derived shoreline error (GPS-satellite) vs. the error after different combinations of corrections. Panel A shows the error after correcting for wave setup only. Panel B shows the error after correcting for wave setup, mean sea-level anomalies (MMSLA), and an optimized water-level correction. The swash envelope (shaded blue region) illustrates how the remaining shoreline excursions appear to be a consequence of wave swash.

417 *2.3.3 The potential influence of wave swash on satellite-derived shorelines*

418 Figure 4 A compares the shoreline error (after tide correction; y-axis) to the wave setup (on the
419 upper x-axis) and to the shoreline correction due to wave setup only (on the lower x-axis).
420 Figure 4 B likewise compares the shoreline error (y-axis) to the complete shoreline correction
421 (due to wave setup and water level) on the x-axis. Notice that the best-fit relationships (red
422 dashed lines) between the shoreline error and the shoreline correction are not exactly one-to-one
423 (black dashed lines) for the wave-setup-only correction (shown on Figure 4 A). However, the
424 shoreline error and the complete shoreline correction (i.e., all terms in Eq. (4)) on Figure 4 B (red
425 dashed lines) are nearly one-to-one (black dashed lines). We also depict the wave-swash
426 envelope (light blue band) on Figure 4 B, which represents the theoretical, horizontal extent of
427 wave swash along a transect where the instantaneous swash line may occur at an arbitrary instant
428 in time (i.e., for an arbitrary phase of the swash). The swash envelope is centered on the wave
429 setup, $\bar{\eta}$, and the upper and lower bounds are calculated as the inverse beach slope (β_f^{-1})
430 multiplied by $\bar{\eta} \pm \eta_{\text{swash}}$, where the maximum swash excursion is calculated as $\eta_{\text{swash}} = 1.69\bar{\eta}$,
431 which is a consequence of the relative magnitude of the empirical swash parameterization (for
432 dissipative beaches) of Stockdon et al. (2006),

433 $$\eta_{\text{swash}} = 0.027\sqrt{H_0 L_0} \quad , \qquad (7)$$

434 which is a factor of $0.027 / 0.016 \approx 1.69$ larger that the empirical setup parameterization in Eq.
435 (5). Hence, in Figure 4 B, the swash envelope has a lower bound slope of -0.69 (which
436 represents $\bar{\eta} - \eta_{\text{swash}} = \bar{\eta} - 1.69\bar{\eta} = -0.69\bar{\eta}$) and an upper bound slope of 2.69 (which represents
437 $\bar{\eta} + \eta_{\text{swash}} = \bar{\eta} + 1.69\bar{\eta} = 2.69\bar{\eta}$), and is centered on one-to-one (black dashed lines, which

represent the mean setup correction ($\bar{\eta}$). As demonstrated in Figure 4 B, most of the observations (blue dots) of the shoreline error (i.e., the difference between the ground-truth, elevation-based GPS shorelines and the image-based satellite shorelines) fall within the swash envelope, shown in light blue, which indicates that the magnitude of the post-correction residual error in shoreline position is similar with the magnitude of potential swash excursions. Further, the analysis presented in Figure 4 B potentially explains why the largest (20 to 30 m) shoreline errors (based on the tide-only correction) are generally positive, since the upper bound of the swash envelope has a much larger slope (i.e., 2.69) than the lower bound (with slope -0.69).

The strong role played by the wave setup (shown in Figure 3) and the swash envelope shown on Figure 4 suggests that time-dependent wave swash greatly influences the visual detection of the shoreline in satellite imagery. Unlike wave setup, swash is oscillatory. Hence, its phase cannot easily be corrected. Therefore, the presence of sizable wave swash in satellite imagery may represent an accuracy bottleneck, which may persist despite the increasing resolution of satellite imagery. As is a common practice in shoreline identification with ground-based cameras, a wave-height threshold might be applied to retain only the observations occurring during low wave conditions. However, the relative infrequency of satellite revisits (especially when compared with ground-based camera observations) would perhaps demotivate the decision to favor observational accuracy over observational frequency. In the application presented here, we do not apply a wave-height thresholding approach and instead retain all satellite-derived shoreline observations for data assimilation. For the following large-scale modeling application, we uniformly apply the site-specific error analysis and bias correction method (described above) to the rest of the California coastline, where we have satellite data but lack traditional beach survey data. We offer the proposed satellite-data-assimilated modeling approach as a means to

achieve reliable forecasts in otherwise ‘data-poor’ environments where in-situ observations are sparse or non-existent.

3. Results

3.1 Long-term shoreline change rates

As a preliminary analysis, we estimate the historical rate of shoreline change by fitting linear trends to observed shoreline positions from 1995-2020. The shoreline trend analysis presented here provides a modern update, benefitting from decades of satellite-derived shoreline observations, to the historical rates for California presented in Hapke et al., (2006). Although we apply unweighted regressions to all available shoreline observations from different sources (e.g., Lidar, GPS, satellite) at each transect, 99.9% of the observations come from satellites, hence they dominate the trend analysis, as expected. Trends fit to satellite-derived shoreline observations have been repeatedly shown to reproduce observed trends (derived from traditional sources of shoreline data for overlapping time periods) in many different settings (e.g., Smith et al., 2021, Castelle et al., 2022). In the current application, the shoreline trends are fit to the full set of tide-, wave- and water-level-corrected satellite-derived shoreline observations (see Section 2.3). However, Castelle et al., (2022) showed that using raw, uncorrected satellite-derived shorelines is generally sufficient for long-term trend analyses.

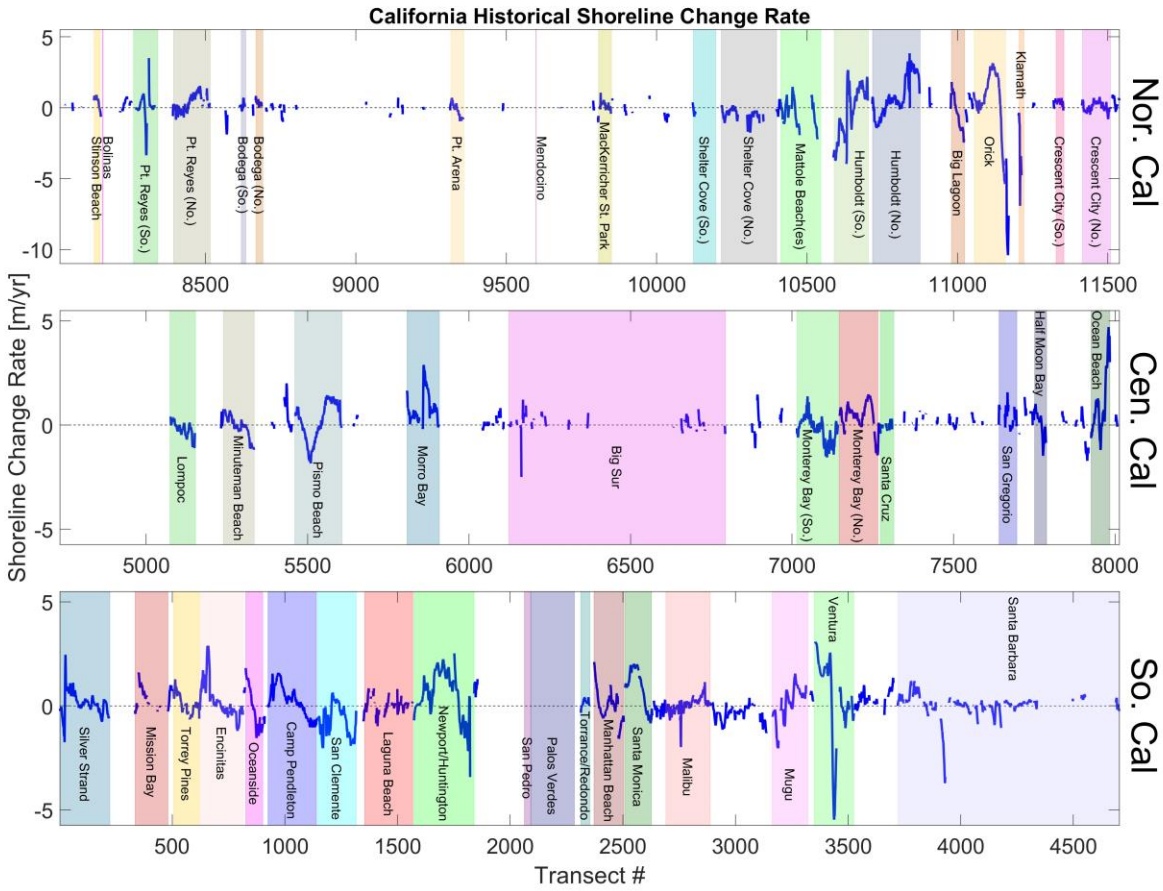

479

480 Figure 5 – Long-term, historical shoreline change rates ($(v_{lt})_0$) for southern California (bottom
481 panel), central California (middle panel), northern California (top panel) from 1995 - 2020
482 (negative = erosion and positive = accretion). The colored bands identify large littoral regions,
483 which are enclosed by harbors, headlands, river mouths, etc.

484

485 Figure 5 plots the long-term shoreline change rate (in m/yr with positive and negative values
486 indicating accretion and erosion, respectively) versus transect number. Figure 5 is split into
487 three portions, i.e., lower, middle, and upper, which represent southern, central, and northern
488 California, respectively. The colored bands in Figure 5 identify large littoral regions, which are
489 enclosed by harbors, headlands, river mouths, etc. Across all of California, we find that 24% of

beaches have been eroding ($\text{rate} < -0.25$ m/yr), 52% have been accreting ($\text{rate} > 0.25$ m/yr), and 24% have been stable ($|\text{rate}| \leq 0.25$ m/yr). Likewise, for southern California only, which generally exhibits more vulnerability to erosion, we find that 30% of beaches show historical erosion, 42% show accretion, and 28% have been stable. By themselves, the shoreline trends, shown in Figure 5, do not identify the causal mechanisms of shoreline accretion or erosion. However, they do suggest a strong anthropogenic signal on the shoreline trend [as was established in Flick (1993) and Hapke et al., (2006)] in certain locations, based on evidence that the largest rates of change occur near harbors or beaches receiving significant sediment input (e.g., from fluvial inputs or nourishments). A notable saw-toothed pattern of erosion and accretion in northern and southern portions of littoral cells, respectively, is visible throughout much of California, but is particularly evident in southern California for the Silver Strand, Mission Bay, Torrey Pines, Encinitas, Oceanside, Camp Pendleton, and San Clemente regions. This saw-toothed pattern is consistent with a mechanism of longshore transport from north to south driven by obliquely incident swell from the North Pacific, which is interrupted (but has partially bypasses) around harbors or headlands. In central and northern California, where nourishments are rare, anthropogenic influences on the shoreline trend can still be seen at harbor entrances (e.g., in Monterey Bay, Half Moon Bay, and Humboldt). Additionally, large signals of shoreline change (in both accretion and erosion) are visible in regions with strong fluvial sediment input (e.g., Humboldt, Orick, Klamath). We observe the largest shoreline trends at the northern portions of Orick and Ocean Beach, with ~10 m/yr of erosion and ~ 5 m/yr of accretion, respectively.

Overall, Figure 5 demonstrates the strong signal of local shoreline trends, which is affected by a multitude of processes such as interrupted longshore transport, headland bypassing, episodic fluvial inputs, beach nourishments, etc. The variability in local shoreline behavior show in Figure 5 also motivates the use of data-assimilation, as locally calibrated residual trends like v_{lt} in Eq. (1) can provides a means of implicitly accounting for processes that are not easy to model or quantify explicitly. As discussed below in Section 3.2.1 and in Appendix B.4, one quarter of the long-term linear trend $(v_{lt})_0$ (shown in Figure 5) is used to provide initial parameter estimates for the residual trend v_{lt}. Using data assimilation, v_{lt} is further refined over the model hindcast period alongside the explicitly resolved shoreline change processes (and their associated parameters), like longshore transport, which are not accounted in the historical trend analysis (Figure 5), but are accounted for in the dynamic model (i.e., Eq. (1)).

3.2 Case study: Ocean Beach

In this section, we provide a case study of the data-assimilated model at Ocean Beach, San Francisco, a well-monitored beach, with a large seasonal signal of episodic erosion as well as persistent erosion and accretion trends in the southern and northern portions, respectively. The case study, presented here, is intended to investigate the performance of the model when assimilating satellite-derived shoreline observations versus monthly GPS-derived shoreline observations (which exist here, but generally do not at other beaches).

3.2.1 Model hindcast

Figure 6 shows time series of wave height, observed versus modeled shoreline position, and the assimilated model parameters at transect #7991 at the southern end of Ocean Beach (which is

adjacent to the San Francisco Zoo and close to the Oceanside Water Pollution Control Plant; see Figure 7 for a map of the precise location of transect #7991). The ensemble median shoreline position and model parameters are shown with red lines in Figure 6. The pink bands in Figure 6 depict the evolving uncertainty at the 95% confidence level, derived empirically from histograms of the assimilated values of the shoreline position and model parameter ensemble. The wave-height time series (Figure 6 A) demonstrates a distinct seasonal pattern of large wave heights in the winter and small wave heights in the summer. The shoreline response (Figure 6 B), which is dominated by wave-driven/equilibrium behavior, is nicely illustrated as nearly the mirror-image of the wave height (in Figure 6 A) with erosion in winter and recovery in summer. Figure 6 B depicts the two different kinds of shoreline observations, which represent the intersection of transect #7991 with satellite-derived shorelines (blue dots + uncertainty) or with GPS-derived mean-sea-level (MSL) shorelines (purple dots). By comparing the assimilated model (red line in Figure 6 B) to the observations (i.e., blue and purple dots Figure 6 B), we see that the model reproduces the observed signal of seasonal shoreline change and the extents of the maximally accreted/eroded beach states in this case study. However, we expect good performance of the model because it is assimilated, i.e., nudged toward the observations. The time series shown in Figure 6 are split into a 'Hindcast (Calibration)' period (1995-2015) and a 'Hindcast (Validation)' period (2015-2020), where data assimilation is turned on and off, respectively. Note that the 'Hindcast (Validation)' is a separate test phase where the agreement between the unassisted model and the observations can provide a fair assessment of the model's skill to faithfully represent shoreline behavior recorded in observations that are previously unseen by the model (as discussed below). Ultimately, its performance during the 'Hindcast (Validation)'

period is perhaps the only thing that affords confidence in the model's predictive capabilities during projection periods (2020-2100).

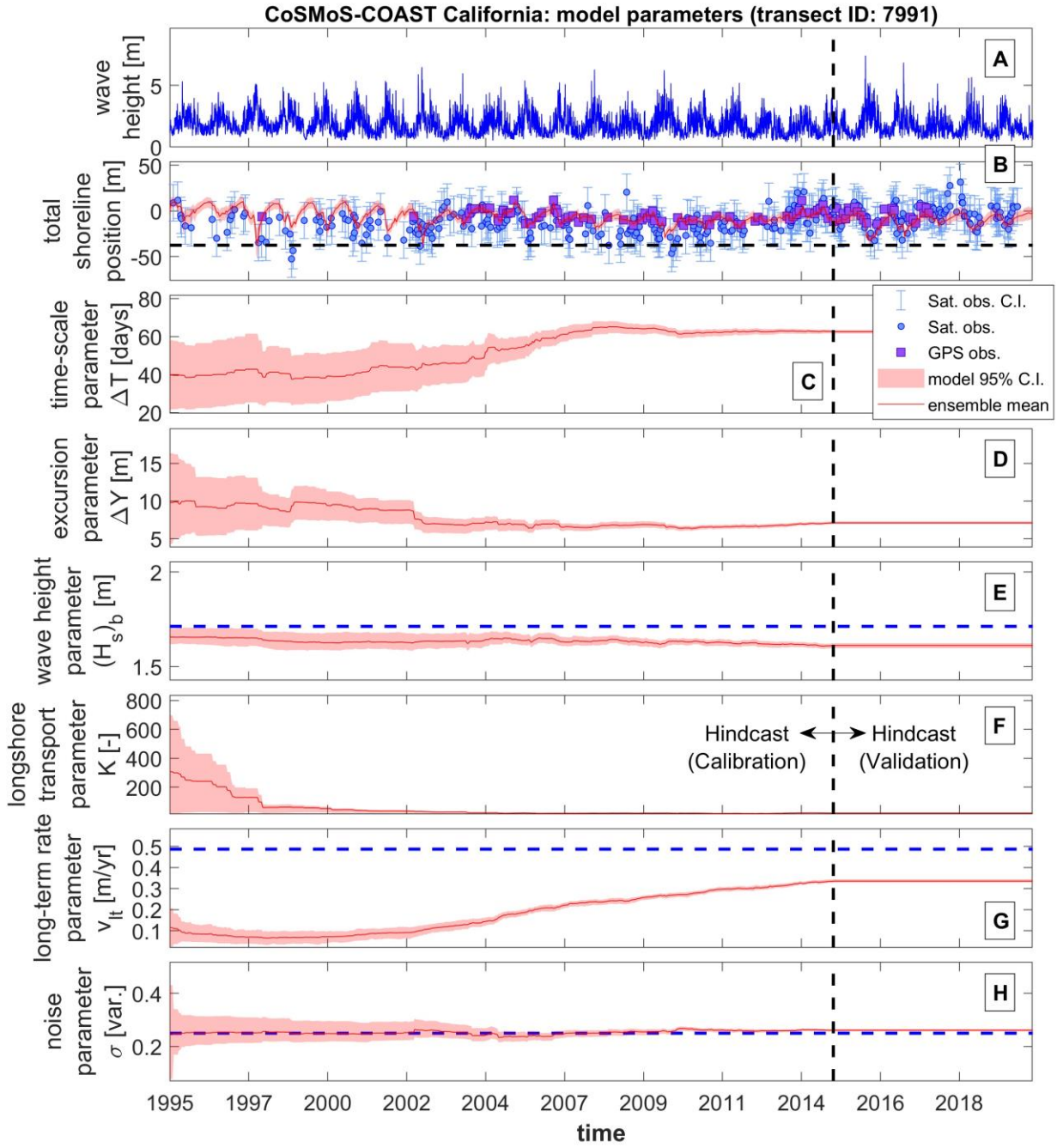

Figure 6 - Time series of model predictions (B) and model parameters (C-H) for transect #7991 at Ocean Beach, San Francisco, California (A) Time series of daily maximum significant wave

height [m], (B) satellite observed (blue dots + uncertainty bands), in-situ GPS observed (purple squares), and simulated shoreline position, Y, (ensemble median shown in red line) and 95% confidence bands (shown in pink bands), (C-H) time series of assimilated model parameters (ensemble median in red line) and uncertainty (shown in pink bands), which are sequentially adjusted via an ensemble Kalman filter as more data are ingested into the model. Note the dashed blue lines on panels E, G, and H represent the local mean of significant wave height time series, the local long-term linear shoreline change rate, and the initial value of the noise parameter, respectively. The dashed black line on panel B represents the location of the non-erodible shoreline on this transect. The time series are split into a 'Hindcast (Calibration)' period (1995-2015) and a 'Hindcast (Validation)' period (2015-2020), when data assimilation is turned on and off, respectively. Note that the model parameters (C-H) remain constant during the Hindcast (Validation) period.

Figure 6 C–H show time series of the assimilated model parameters including the equilibrium time-scale parameter (ΔT), the equilibrium erosion length-scale parameter (ΔY), and the equilibrium wave-height parameter ($(H_s)_b$), the longshore-transport coefficient (K), the long-term residual shoreline-change rate (v_{lt}), and the additive-noise parameter (σ), respectively. Note that the entire 200-member parameter ensemble is sequentially adjusted during each data-assimilation step (i.e., at the times when observations are available), which is reflected in Figure 6 C–H as adjustments in the values and uncertainty bands of each model parameter. During the 'Hindcast (Validation)' period (and for future forecast periods), data assimilation is turned off, and thus the values of all model parameters remain constant (in time, but variable in space). Ideally, when enough data are available during the hindcast period, the assimilated values of the model parameters will be sufficiently converged before the forecast period begins. Figure 6 indicates that the parameter values and particularly the uncertainty appear to converge over the course of the simulation. As demonstrated in Vitousek et al. (2021), the evolution of the width of the uncertainty bands is set by a balancing act between the processes of additive noise and data assimilation (or damping), which expand and contract the spread of the ensemble,

586 respectively. In this case, the parameter ensembles appear to converge to roughly constant-in-
587 time value toward the end of the 'Hindcast (Calibration)' period because the data-assimilation
588 method (and the amount of available data) suppresses/converges the uncertainty faster than the
589 additive noise expands it. During the 'Hindcast (Validation)' and the projection periods, the
590 process of additive noise (i.e., term 5 in Eq. (1)) is completely turned off, and thus the parameter
591 ensemble is completely constant in time. However, retaining additive noise after the 'Hindcast
592 (Calibration)' would lead to a linear growth in the variance of the ensemble (or a square-root-
593 time growth in the uncertainty bands with time) as shown in Vitousek et al., (2021). Note that
594 while the parameter ensemble is held static for the projection period, the model will generally
595 still exhibit a growth of its uncertainty bands over time, which are, for example, associated with
596 the continuation of an uncertain/ensemble long-term trend or sea-level-driven recession
597 coefficient (as shown in the Ocean Beach case study below), or from applied ensemble forcing
598 conditions (e.g., ensemble wave or sea-level rise projections).

599 Finally, we highlight a few salient features of the convergence of the model parameter ensemble
600 as demonstrated in Figure 6. Figure 6 F indicates that the longshore transport coefficient is
601 rather small in this location (i.e., K is calibrated to almost zero at this location). The relatively
602 small magnitude of longshore transport at this location might be controlled by a few factors: (1)
603 most effects of longshore transport generally appear at the ends of littoral cells (e.g., Anderson et
604 al., 2018) and this particular location is in the middle of Ocean Beach, (2) the shoreline is
605 relatively straight in this location, and hence large gradients in longshore transport are not
606 expected, and (3) the wave angle is predominantly perpendicular to the shoreline at this location
607 on the southern portion of Ocean Beach, although the deep-water to nearshore wave refraction at
608 the northern portion of Ocean Beach plays an important role in driving northward longshore

609 transport, as shown in Vitousek & Barnard (2015). In the context of one-line models, the local
610 wave angle relative to the shoreline, which is extremely important in setting the magnitude of
611 longshore transport, can be controlled by correcting oblique offshore conditions to the local
612 shoreline orientation (Chataigner et al., 2022) or by applying wave conditions that are very close
613 to shore (i.e., in very shallow water). Here, the CDIP wave hindcast (detailed Appendix C.1),
614 which is used to propagate wave conditions to shore (i.e., up to about ~10 m depth) and is co-
615 located with the offshore ends of each transect, is a tremendous resource for the current
616 shoreline-modeling application. Although it has not been tested in the current application,
617 applying linear wave theory (as in Dabees (2000), for example) or the corrections described in
618 Chataigner et al., (2022) might account for the additional wave transformation processes taking
619 place inshore of the wave hindcast locations. However, the strong model performance
620 (discussed below) for this case study suggests that additional wave transformation is generally
621 unnecessary for the current application (given the quality and proximity of the existing CDIP
622 wave hindcast).

623 As mentioned above, the ensemble mean of the long-term residual shoreline change rate v_{lt}
624 shown in Figure 6 G is initialized to approximately one quarter of the local long-term, linear
625 shoreline erosion rate $(v_{lt})_0$ (shown in Figure 5), which is depicted in the blue dashed line on
626 Figure 6 G. We initialized the long-term rate v_{lt} to only one quarter of the long-term rate, $(v_{lt})_0$,
627 because we expect that much of the 'signal' contained within the long-term trend, $(v_{lt})_0$, will be
628 parsed into the model's explicitly resolved components of shoreline change (e.g., longshore
629 transport). In this case, as shown in Figure 6 G, the residual is calibrated to be approximately
630 66% of the historical shoreline trend (up from the initial guess of 25%). However, Figure 6 G

demonstrates how the data-assimilation method satisfactorily calibrates v_{lt} over the course of the simulation toward a value that is consistent with the recent shoreline trend at this location. Note that the historical trend represents a time-averaged trend $(v_{lt})_0$ (over the entire span of observations 1995-2020), whereas the residual term v_{lt} represents more of a modern trend, as a consequence of the (sequential) data-assimilation method.

Figure 7 depicts observed versus modeled shoreline positions for different model configurations that assimilate the different types of data, e.g., GPS (in panel B) versus satellite-derived shorelines (in panel C) versus both types (Panel D). Figure 7 A shows the wave-forcing time series at transect #7991, whose precise location is shown in the thick green line in Figure 7 E. As in Figure 6, the time series in Figure 7 A, B, C, and D are split into 'Hindcast (Calibration)' (1995-2015) and a 'Hindcast (Validation)' (2015-2020) periods, where data assimilation is turned on and off, respectively. The goal of this test is to better understand the accuracy of the calibrated model when using several years of high precision, but lower temporal frequency data (e.g., monthly GPS observations) versus using several years of lower precision, but higher temporal frequency data (e.g., satellite-derived data). With this comparison, we seek to determine if (for the purposes of model calibration) satellite-derived shorelines can be used in lieu of in-situ observations, which exist only at a handful of well-monitored beaches and are generally unavailable for perhaps over 99% of other beaches worldwide.

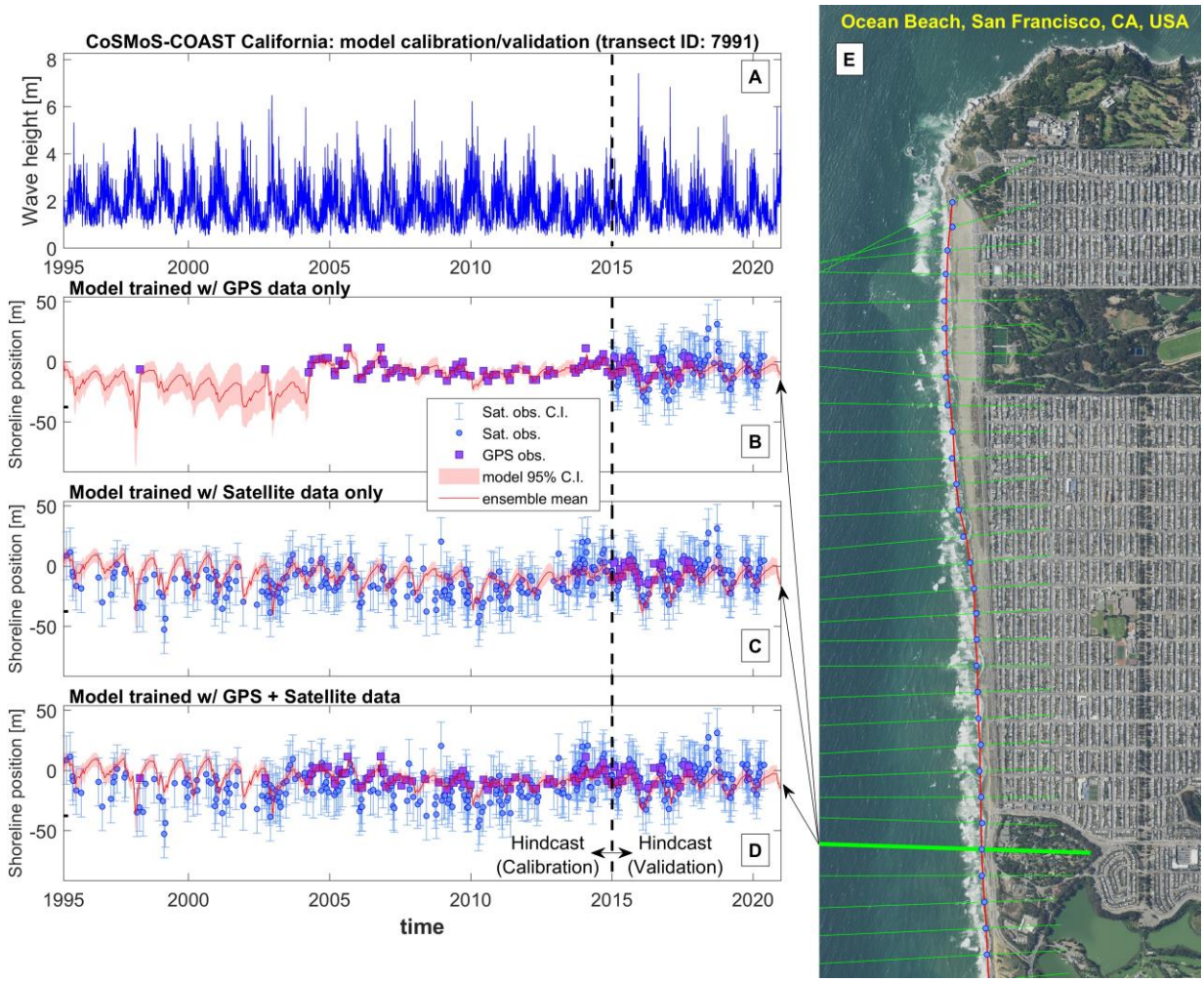

649

650 Figure 7 – Time series of (A) daily maximum significant wave height [m] for transect #7991 at
651 Ocean Beach, San Francisco, California, which is indicated in the thick green line in the high-
652 resolution aerial photo shown in panel E. The figure (panels B, C, and D) also depicts time
653 series of satellite observed (blue dots + uncertainty bands), in-situ GPS observed (purple
654 squares), and simulated shoreline position, Y, (ensemble median shown in red line) and 95%
655 confidence intervals (C.I.) shown in pink bands using different types of assimilated data. Panels
656 B, C, and D show the model calibrated with only GPS data, only satellite-derived data, and both
657 types of data, respectively. The time series are split into a 'Hindcast (Calibration)' period (1995-
658 2015) and a 'Hindcast (Validation)' period (2015-2020), when data assimilation is turned on and
659 off, respectively. In panels B, C, and D, each model achieves an RMS error of approximately 16
660 m compared with the GPS observations during the validation period. (Basemap is from a
661 current, high-resolution aerial photograph of Ocean Beach available through NOAA Digital
662 Coast).

663

Figure 7 B and C show marked differences in the simulated shoreline position and uncertainty (red line and pink bands, respectively) during the calibration period between assimilating GPS data (panel B) versus satellite-derived data (panel C). In particular, in 2005 (at the onset of the regular field monitoring campaign), the GPS-data-assimilated model (panel B) becomes heavily constrained to fit the (highly accurate) observations. The satellite-data-assimilated model (panel C), on the other hand, is adjusted more slowly/cautiously to the satellite-derived shoreline positions (blue dots) owing to their large (blue 'whiskers') uncertainty. However, during the validation period, each of the calibrated models (GPS vs. satellite vs. both, shown in Figure 7 B, C, and D, respectively) demonstrate remarkable similarity, suggesting that calibrations using only satellite observations are on par with calibrations using only GPS data.

Figure 8 shows the root-mean-square error (RMSE), $\varepsilon_{\mathrm{RMSE}}$, defined in Eq. (2), which compares the modeled and observed shoreline positions, as a function of calibration-data type and the number of years of data. The RMSE values reported in Figure 8 is the average across all transects within the Ocean Beach survey bounds (transect #7958 to transect #8016), during the 'Hindcast (Validation)' period (2015-2020). As more years of observations are assimilated, the RMSE will ideally decrease as the model becomes fully calibrated. Note that in Eq. (2), we apply different RMSE metrics if the observations (Y_{obs}) during the validation period come from GPS-derived shorelines (Figure 8 A) or satellite-derived shorelines (Figure 8 B). Figure 8 indicates that assessing model accuracy during the validation period using satellite-derived shorelines (Figure 8 B) has a similar behavior (i.e., RMSE reduces as the amount of calibration data increases) to assessing model accuracy using GPS-derived shorelines (Figure 8 A). However, the assessed model accuracy is generally better when comparing the model to GPS

observations (i.e., the curves in Figure 8 A show lower error than those in Figure 8 B), likely owing to the precision of the GPS observations compared to the satellite-derived shorelines. Figure 8 establishes some consistency in model performance when either calibrating or validating it using satellite-derived shorelines versus GPS-derived shoreline observations at a highly monitored site, as described below.

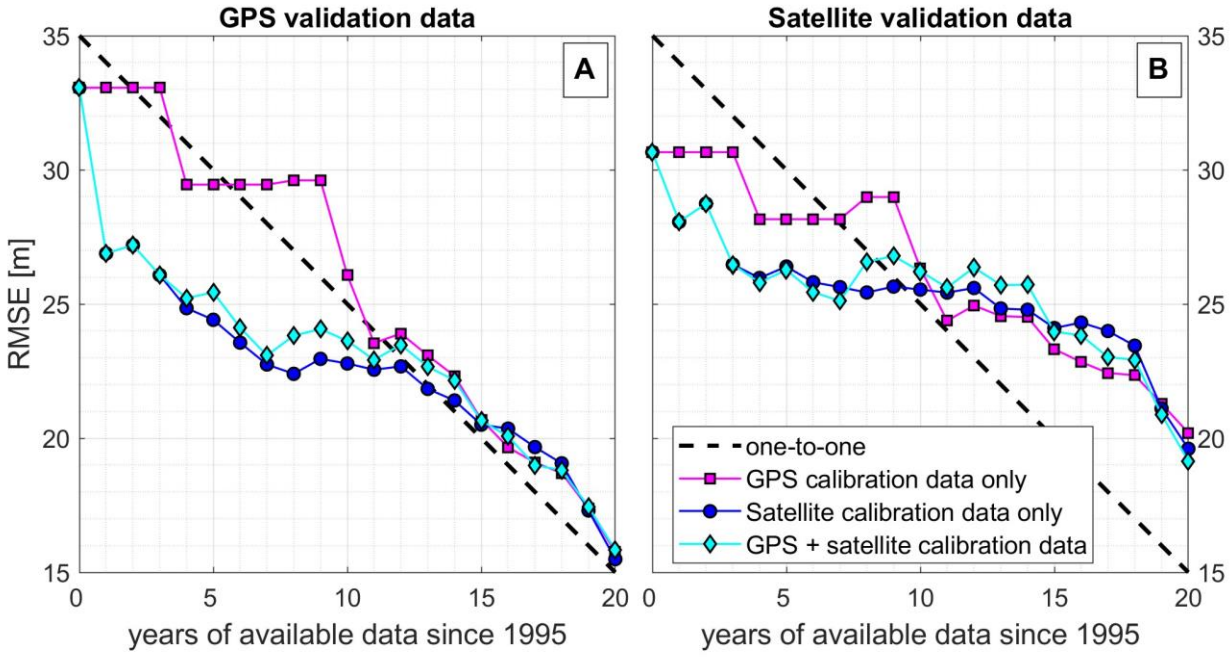

Figure 8 – The spatially averaged root-mean-square error (RMSE) of the model compared to observations spanning Ocean Beach during the 'Hindcast (Validation)' period (2015-2020) vs. the number of years of available data used during model calibration. Panels A and B correspond to applying GPS-derived or satellite-derived shoreline for validation, respectively, during variably sized calibration periods (1995 to 1995+ x, where x is the 'years of available data', plotted on the x-axis). The figure shows different RMSE metrics when calibrating the model with GPS data only (i.e., purple squares), with satellite-derived shorelines (i.e., dark blue dots) or both (i.e., light blue diamonds). The blacked dashed line represents a one-to-one line, in which the RMSE reduces by 1 m with each additional year of data.

Figure 8 also illustrates the differences in model RMSE when calibrating the model using different types of calibration data (GPS data only vs. Satellite data only vs. both data sets, shown in purple, dark blue, and light blue, respectively). We also investigate the effects on RMSE as a function of the length of the calibration period, where we artificially turn off the data-assimilation step prior to the 'Hindcast (Validation)' (2015-2020) period. For example, 10 'years of available data since 1995', shown on the x-axis of Figure 8, indicates a calibrated simulation from the period 1995-2005 (compared the full 20-year calibration period of 1995-2015). In all cases, we apply an unchanging 'Hindcast (Validation)' period of 2015-2020. In general, as more data become available, the RMSE (shown in Figure 8) decreases, but not always consistently (often owing to the temporal inconsistency of the observations). For example, the convergence of the GPS-calibration-data-only (i.e., purple) curves in Figure 8 demonstrates two plateaus as more years of data are added, associated with the availability of only two data points prior to the commencement of the extensive field campaign in 2005, which corresponds to isolated (Lidar) surveys in Spring 1998 and Fall 2002 (as shown in Figure 7 B). Conversely, satellite data (blue dots) are more regularly available over the course of the entire simulation, and thus the RMSE shown in Figure 8 B drops rapidly initially, and then at a slightly slower rate thereafter. In each case, the model RMSE decreases slightly more rapidly as modern data become available (i.e., observations collected just prior to the start of the 'Hindcast (Validation)' in 2012-2014, which correspond to 18-20 'years of available data', respectively). This steeper decrease in RMSE here makes sense (even though the model parameters are mostly converged at this point as shown in Figure 6) since re-initializing the model's state (particularly the starting shoreline position) to a modern observation is important for improving model accuracy. Using all available data, the model achieves an RMSE of approximately 16 m versus 20 m when

validating the model against GPS observations (Figure 8 A) versus when validating the model against satellite-derived observations (Figure 8 B), respectively, at this location. Note that the reported model RMSE is only slightly higher than the RMSE of the satellite-derived shorelines themselves (i.e., 14 m) as demonstrated in Figure 3.

3.2.2 Model projection

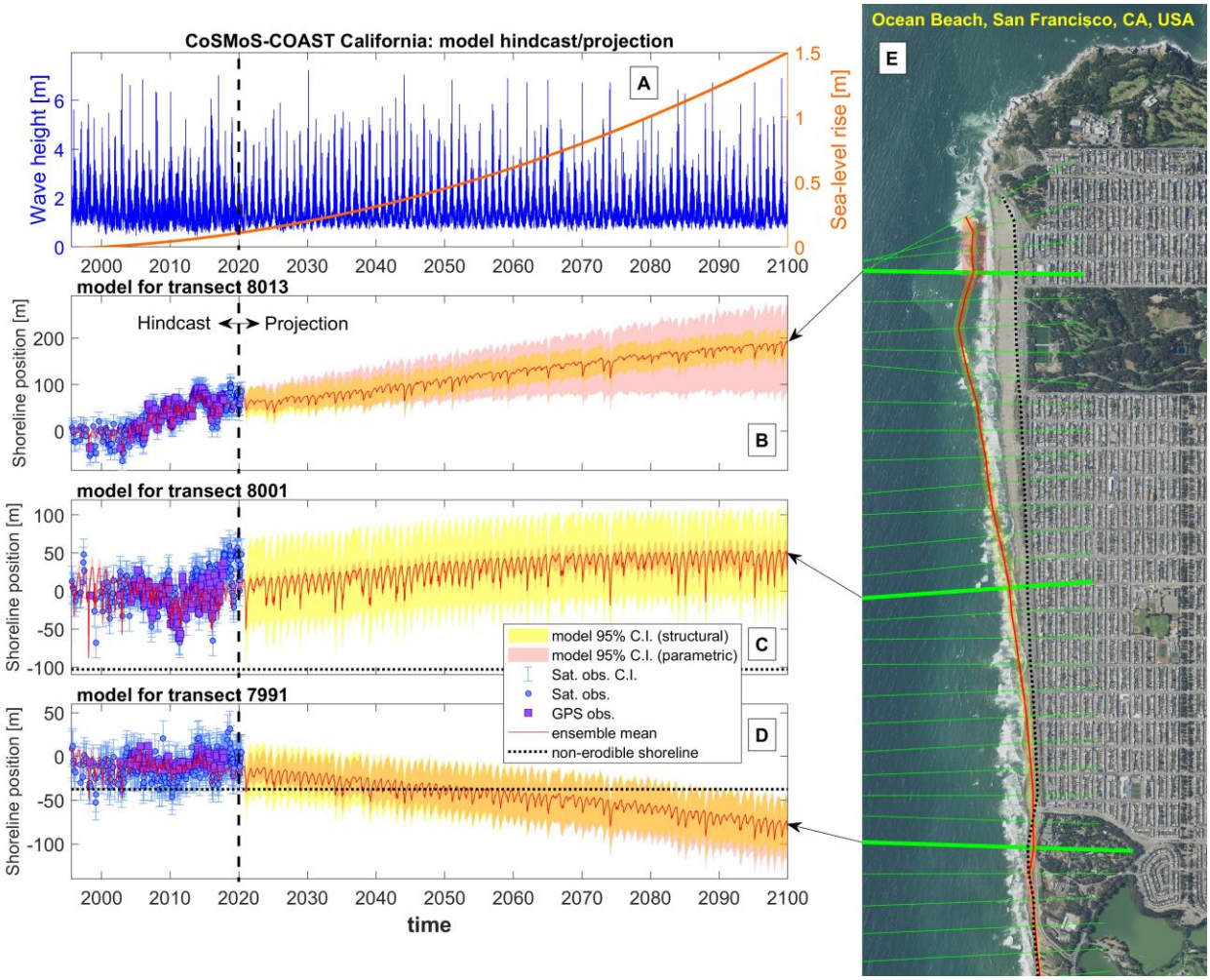

Figure 9 - Time series of (A) daily maximum significant wave height [m] (left axis) and projected sea-level rise [m] (right axis) for transect #7991 at Ocean Beach, San Francisco, California, which is indicated in the bottom-most thick green line in the high-resolution aerial

photo shown in panel E. Panels B, C, and D depict time series (at different Ocean Beach transects) of the long-term projected ensemble median shoreline position (red line), the 95% confidence intervals (C.I.) of the parametric/epistemic uncertainty (red bands) and the structural uncertainty (yellow bands), the satellite-derived shorelines (blue dots) and uncertainty bands (blue 'whiskers'), and the in-situ GPS-observed shorelines (purple squares). Panels C, D, and E also show the location of the non-erodible shoreline (black dotted line). The time series are split (visually, by the black vertical dashed line) into 'Hindcast' (1995-2020) and 'Projection' (2020-2100) periods, where the model is calibrated/validated and run forward, respectively. Note that the dominance of the structural vs. parametric/epistemic uncertainty is transect dependent. (Basemap is from a current, high-resolution aerial photograph of Ocean Beach available through NOAA Digital Coast).

Figure 9 depicts long-term projections (up to 2100) of shoreline position and uncertainty (calibrated with all available data) for the Ocean Beach case study under future wave conditions and 1.5 m of sea-level rise. Panels A, B, C, and D depict time series of the long-term projected wave and sea-level conditions, ensemble median shoreline position (red line), and the 95% confidence intervals of the epistemic/parametric uncertainty (shown in red bands and described in Section 2.2.2) and the structural uncertainty (yellow bands, also described in Section 2.2.2). The panels also show the satellite-derived shorelines (blue dots) and 95% confidence bands (blue 'whiskers'), and the in-situ GPS-observed shorelines (purple squares) used for model calibration during the hindcast period. Figure 9 E shows a high-resolution aerial photograph of Ocean Beach with a map of the modeled shoreline position and uncertainty bands as well as the non-erodible shoreline. Panels C, D, and E also show the location of the non-erodible shoreline (black dotted line). Note that, in panel D, the projected shoreline moves landward of the non-erodible shoreline, indicating loss of sandy beach at this location. Under the 'hold the line' scenario (described in Appendix C.3, which is not shown here), the modeled shoreline is prevented from eroding past the non-erodible shoreline and acts as if no beach sediment is available for longshore transport when the modeled shoreline is coincident with the non-erodible

763 shoreline. In Figure 9, the time series are split (visually, by the black dashed line) into
764 'Hindcast' (1995-2020) and 'Projection' (2020-2100) periods, where the model is calibrated and
765 validated (as in Figure 7) and run forward until 2100, respectively. Note that the model projects
766 long-term accretion, relative stability, and erosion in the northern, central, and southern portions
767 of Ocean Beach, respectively, that are somewhat consistent with modern shoreline trends
768 combined with accelerated sea-level-rise-driven recession, which tends to flatten or reverse
769 historical accretion trends. Much like the variability in projected shoreline trends, the
770 uncertainty bands also demonstrate marked variability across Ocean Beach. At transect #7991
771 (shown in Figure 9 D), the structural and parametric uncertainties are roughly the same size,
772 which represents an ideal case: the model's internal assessment of its uncertainty (i.e., the
773 parametric uncertainty) is roughly equivalent to an external evaluation of its uncertainty (i.e., the
774 structural uncertainty). However, this is not always the case. Instead, it is often the case that the
775 model is either overconfident (e.g., where parametric uncertainty << structural uncertainty, as
776 shown in Figure 9 C) or underconfident (e.g., where parametric uncertainty >> structural
777 uncertainty, as shown in Figure 9 B). At transect #8013 (shown in Figure 9 B), for example, the
778 model's large parametric uncertainty is driven by spread of the long-term, residual shoreline
779 trend, v_{lt} , which is not easily constrained via data assimilation, in this case.

780 In summary, the case study of Ocean Beach (presented here) indicates that the calibrated
781 accuracy of the satellite-data-assimilated model is comparable to that of the GPS-data-
782 assimilated model. This comparable accuracy (of the satellite-data-calibrated model and the
783 GPS-data-calibrated model) increases confidence in our ability to calibrate and validate shoreline
784 models over spatiotemporal scales using satellite data. In the following section, we show
785 projections of future shoreline position and uncertainty across California.

3.3 California state-wide projections

Although Lidar and GPS observations of shoreline position are sparse in space and time, satellite-derived shoreline observations can span the entire California coastline and beyond. Previous studies, relying on only Lidar and GPS data (e.g., Vitousek et al., 2017), have arguably had nearly sufficient data for large-scale model calibration over large spatial scales. However, because model calibration periods must often be long and shoreline-change time series are often sparse, very limited amounts of Lidar/GPS data (if any) remain for model validation. Prolific satellite-derived data enable model calibration *and* validation over large spatiotemporal scales.

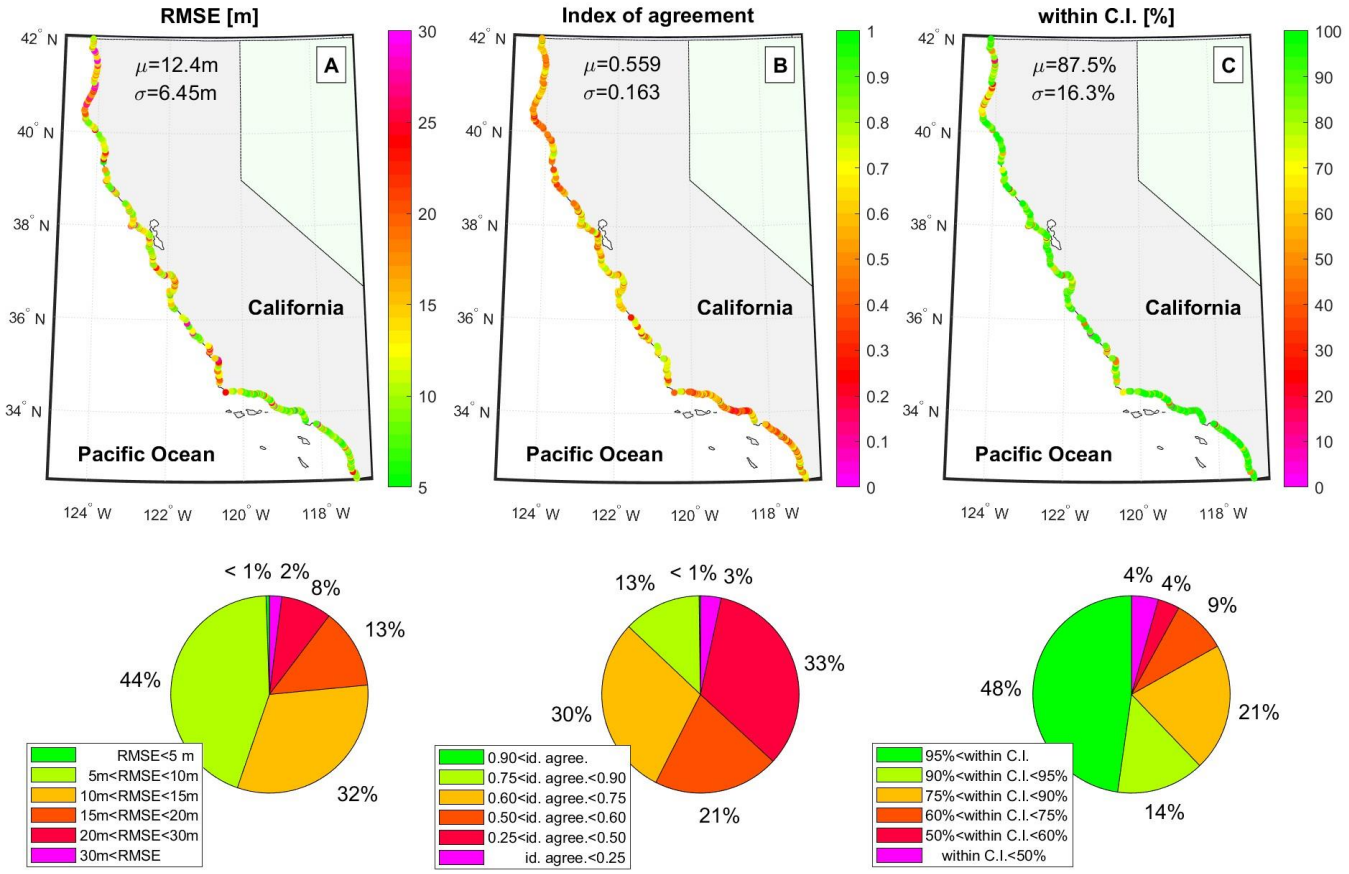

Figure 10 – Spatial variability (across the state of California) in model performance metrics during the 'Hindcast (Validation)' period (2015-2020). Panel A depicts the model's root-mean-

square error (RMSE) (Eq. (2)) against satellite-derived shoreline observations; panel B depicts the index of agreement (Eq. (3)) between model and satellite-derived shoreline observations; and finally, panel C illustrates the percentage of the time that the model predictions during the validation period (2015-2020) fall within the 95% confidence bounds of the satellite-derived shoreline observations. The bottom panels show pie charts (for each of the metrics shown above), which indicate various categories of model performance and their associated percentages across the entire California model domain.

Figure 10 shows the spatial variability across California of three different model performance metrics during the 'Hindcast (Validation)' period (2015-2020), including the (1) RMSE (Eq. (2)), (2) the index of agreement (Eq. (3)), and (3) the percentage of time that the model falls within the confidence bounds of the satellite shorelines (described below) in panels A, B, and C, respectively. The bottom panels of Figure 10 show pie charts that indicate various categories of model performance and their associated percentages across the entire California model domain. The RMSE (calculated via Eq. (2) and shown in Figure 10 A) applies observations (Y_{obs}) that come from satellite-derived shorelines, which are the only source of consistent observational data at the scale of the current analysis. Figure 10 A indicates that, in this application, the model achieves an RMSE of <15 m for 77% of California and a mean RMSE of 12.4 m, which seems to be roughly consistent with the accuracy of the satellite-derived shoreline observations themselves. The mean RMSE metrics across the different model transect types of "full model", "cross-shore only", and "rate only" are 13.3 m, 10.8 m, and 10.3 m, respectively. However, the lower RMSE values for "cross-shore only" and "rate only" are likely due to the more limited shoreline variability of these coastal settings compared to that of the "full model" transects.

The index of agreement (Willmott, 1981), given by Eq. (3), is shown in Figure 10 B. We find that $d > 0.5$ across 57% of California with a mean of $\bar{d} = 0.559$. In a recent blind-test

822 shoreline modeling competition (Montaño et al., 2020; comprised of 15 years of calibration data
823 and 3 years of data-blind comparisons), the best performing shoreline models achieved
824 $d \approx 0.5$ - 0.7 , and the performance metrics achieved here, over a vastly larger scale, seem
825 comparably good.

826 Lastly, the third and final metric we evaluate here is called 'within C.I.' in Figure 10 C, which
827 represents the percentage of the time, during the 'Hindcast (Validation)' period (2015-2020), that
828 the model predicted shoreline position falls within the 95% confidence levels of the satellite-
829 derived shoreline observations, which are assumed to be identical to $\pm 2\varepsilon_{\text{sat}}$, where ε_{sat} is the 14
830 m RMSE derived at Ocean Beach (where dense GPS observations are available) and applied
831 uniformly across the California coast. Although the uniform prescription of satellite-error
832 statistics is not ideal, we note that the general 10-15 RMS accuracy of satellite-derived shorelines
833 has been well established through extensive testing at many well monitored sites (e.g., Hagenaars
834 et al., 2017, Luijendijk et al., 2018, Pardo-Pascual et al., 2018, Vos et al., 2019b, Castelle et al.,
835 2021, and Vos et al., 2023). Figure 10 C indicates that the model predictions are within the
836 confidence intervals of the satellite observations approximately 88% of the time (on average)
837 across California.

838 Across all skill metrics shown in Figure 10, the model seems to achieve the best performance
839 (i.e., the lowest RMSE and the largest index of agreement) in southern California. However, this
840 is perhaps expected since the equilibrium shoreline-change model, i.e., Yates et al. (2009), which
841 dominates the short-term signal of change, was conceived from local shoreline behavior and
842 observations thereof at Torrey Pines Beach in southern California. However, since its initial
843 development in southern California, the Yates et al. (2009) model has been proven to be skillful

844 across diverse coastal settings (Castelle et al., 2014, Montaño et al., 2020, Hunt et al., 2023).
845 Poorer model performance is generally encountered in northern California, particularly across
846 Humboldt County, which we hypothesize is due to large signals of fluvial sediment input and the
847 presence of large-scale sand waves (~200-1,000 m wavelength) in the region, whose dynamics
848 are not well resolved in the context of the model governing equation. The limited model
849 performance, particularly in regions of high fluvial sediment input, highlights an area for
850 improvement. Future modeling efforts could seek to explicitly account for fluvial sediment
851 inputs by coupling with models of terrestrial processes such as wildfire and pluvial flood events,
852 which can significantly affect coastal sediment budgets (e.g., Warrick et al., 2022), as further
853 discussed below.

854 After validating the model's performance against observed behavior, we apply the model to
855 project future changes in shoreline position until 2100. In particular, we explore scenarios of
856 future beach loss (like the example shown in Figure 9 D) due to accelerated sea-level rise over
857 the 21st century following several previous works (e.g., Vitousek et al., 2017, Le Cozannet et al.,
858 2018, Vousdoukas et al., 2020, and D'Anna et al., 2022). Here (in Figure 11) we analyze the
859 percentage of model transects across California that experience seasonal or persistent beach loss
860 as a function of time and under the 9 sea-level scenarios (0.5, 0.75, 1.0, 1.25, 1.5, 1.75, 2.0, 2.5,
861 3.0 m - given in Figure 20 in Appendix C). In Figure 11, we apply the "no hold the line" and
862 "continued accretion" management scenario (as described in Appendix C), which represents the
863 most conservative scenario. However, as shown in Vitousek et al. (2017), the different
864 management scenarios (replicated here) only result in differences of a few percentage points in
865 the future prevalence of beach loss. Figure 11 categorizes future shorelines into four categories
866 and depicts how those categories change over time (panel A) or with different sea-level rise

867 scenarios (panel B). The four categories, namely “wide perennial beach”, “narrow perennial
868 beach”, “ephemeral beach”, and “persistent beach loss”, indicate increasing levels of
869 concern/vulnerability. The latter two categories, “ephemeral beach”, and “persistent beach loss”,
870 are beach transects whose projected shoreline positions erode past the non-erodible shoreline
871 (i.e., the division between sand and cliffs, dunes, or urban backshores as described in Appendix
872 C.3) either temporarily (e.g., seasonally) or persistently, respectively, by 2100. The first two
873 categories, on the other hand, are mostly self-explanatory and represent either a “wide perennial
874 beach” and “narrow perennial beach” at model transects with greater than or less than 50 m in
875 width[1], respectively, that are not projected to erode close to the non-erodible shoreline by 2100.

[1] 50 m is a somewhat commonly chosen as the threshold that separates wide from narrow beaches, e.g., Vousdoukas et al., 2020.

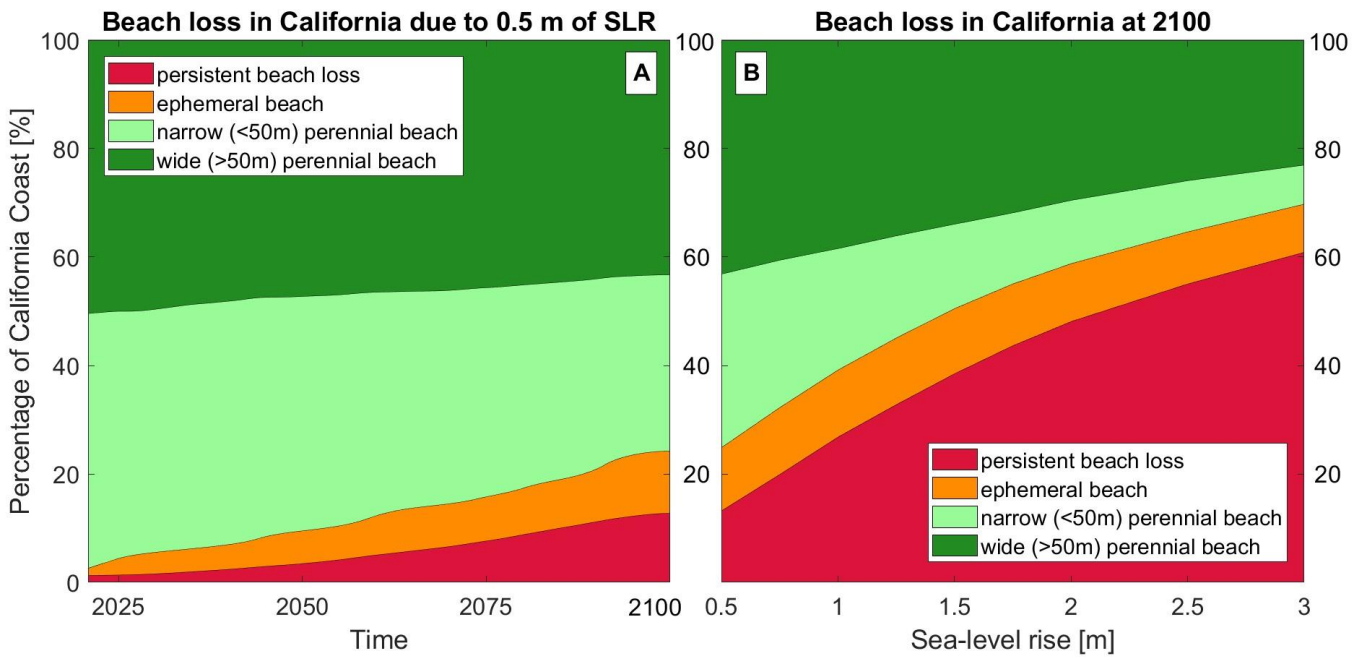

Figure 11 – The percentage of beach loss across California as a function of time, and sea-level-rise scenario of 0.5 m by 2100 (panel A) and as a function of different sea-level rise scenarios by 2100 (panel B; see Figure 20).

The results in Figure 11 A indicate that the number of transects experiencing "ephemeral" or "persistent" beach loss accelerates with time (due to accelerated sea-level rise). As shown in Figure 11 B, the model projects that 13 to 61% of transects across California will experience permanent beach loss (under sea level scenarios of 0.5 to 3.0 m, respectively). Including ephemeral/seasonal erosion increases the percentage of beaches lost to between 25 and 70% of transects across California. Vitousek et al. (2017) projected total beach loss at 31 to 67% of southern California beaches under sea-level scenarios of 0.93 to 2 m of sea-level rise, respectively, and the (updated) projections given here across the entire state are largely consistent with these previous findings. As in Vitousek et al. (2017), the model does not account for erosion through different substrates (e.g., rocky cliffs and concrete structures) but instead

891 treats the entire transect as a sandy substrate during the “no hold the line” scenario. Clearly, this
892 unmodified approach will generally overestimate the landward extent of erosion into cliffs and
893 infrastructure under the “no hold the line” scenario. However, the model predictions of sandy
894 beach erosion extent should generally remain valid up until the beach fully erodes.

895 The model does not explicitly account for sediment supplied to the beach from eroding cliffs,
896 dunes, or rivers, and hence, but instead lumps all of the estimated sediment supply into the long-
897 term residual shoreline trend (e.g., v_{lt}), obtained via data assimilation. Hence, the modeling
898 approach (and the results in Figure 11) may misrepresent the episodic nature of sediment supply
899 in some locations. The current shoreline model could, in theory, be coupled with parameterized
900 models of cliff erosion and/or fluvial input (e.g., Limber et al., 2018, Alessio & Keller 2020,
901 Regard et al., 2022) to mitigate reliance on the long-term residual shoreline trend parameter (e.g.,
902 v_{lt}). However, this endeavor, which has not yet been attempted in the literature, is beyond the
903 scope of the current work and is left as future work.

904

905

906

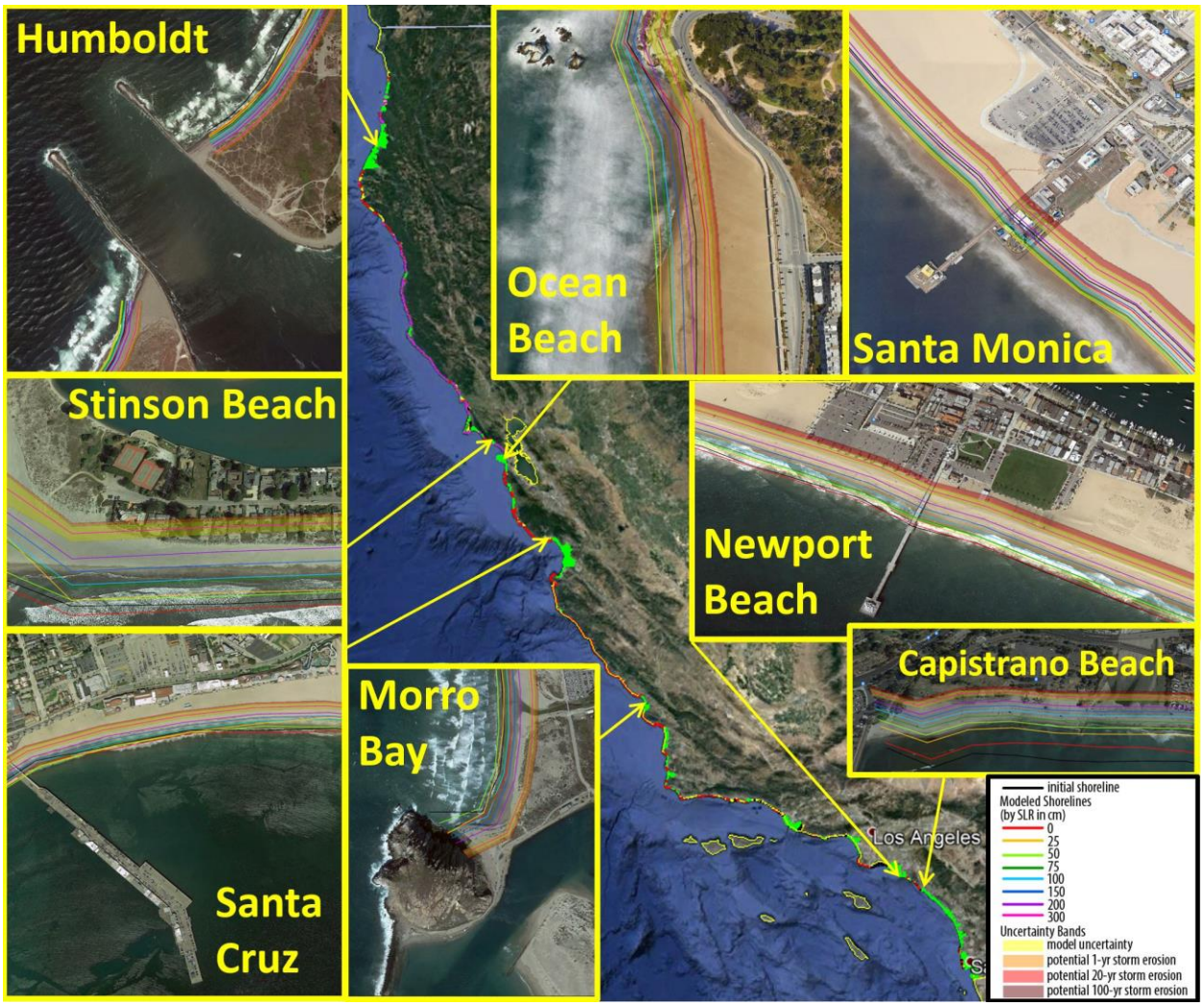

907

908 Figure 12 - Shoreline modeling predictions for ~1,350 km of coastline in California produced by
909 the current CoSMoS-COAST model. The predictions represent the shoreline position in 2100
910 with 1.0 m of sea level rise. The yellow bands represent the projected shoreline position and
911 (parametric) uncertainty. Note that the transect color across the basemap of California (from
912 Google Earth) is shown/described in Figure 2.

913

914 The shoreline projections, given here, foretell potentially serious impacts for many of
915 California's iconic beaches as well as the economic, recreational, and protective benefits they
916 provide. For example, Figure 12 shows that popular beaches such as Newport Beach, Capistrano
917 Beach, and the southern portion of Ocean Beach may experience significant erosion by 2100,

while others like Santa Monica and the northern portion of Ocean Beach are projected to accrete in spite of the impacts posed by sea-level rise. The California statewide shoreline-change projections produced as part of this study are available via a USGS data release that accompanies this paper (Vitousek et al., 2023 [data set]). Although many of California's beaches are vulnerable to future erosion (primarily due to sea-level rise and sediment restrictions), scenarios of future beach loss are not unique to California but may become prevalent for many coastal communities throughout the world. However, as shown here, satellite-based shoreline monitoring and data-assimilated modeling are becoming powerful tools for prediction of coastal climate-change impacts and potentially for monitoring the effectiveness of engineering and nature-based solutions.

4. Discussion

Satellite-derived shoreline observations enable predictions across unprecedented spatiotemporal scales. The proliferation of satellite-derived shoreline observations further motivates modeling approaches that can explicitly resolve variability at increasingly shorter time scales (e.g., wave-driven coastal change) yet can be applied over vast, historically data-poor regions. Additionally, increased availability of spatiotemporally dense observations will also greatly benefit long-term historical trend analyses. Castelle et al. (2022) showed that even raw satellite-derived shorelines (which are not corrected for tide or wave setup) can reproduce long-term shoreline trends obtained from traditional methods (e.g., manually digitized shorelines from orthorectified and georeferenced aerial photographs in their study). Avoiding the need to apply tide and wave corrections is a particularly attractive benefit to simplified shoreline-trend analysis efforts. However, tidal-prediction models, which are widely available and accurate, are already

incorporated in satellite toolboxes like CoastSat (Vos et al., 2019a), which motivates their use. Nearshore wave hindcasts, needed for wave-setup-corrections to satellite derived shorelines, are generally only available for highly developed and monitored coastlines (e.g., the CDIP hindcast – O'Reilly et al., 2016) or in deeper, offshore waters (e.g., ERA-5 reanalysis – Hersbach et al., 2020). Hence, they might represent a limiting resource for correcting satellite-derived shoreline observations. However, as nearshore wave information is also a critical component of data-assimilated shoreline model predictions, the generation of hindcasted nearshore wave data is complementary to both shoreline modeling and satellite monitoring efforts. As both hindcasted and forecasted nearshore wave information becomes increasingly available, the prospect of operational monitoring and prediction of coastal change becomes possible. Further, satellite-derived workflows are becoming increasingly automated, in contrast to workflows relying on GPS or Lidar data. Thus satellite-derived shoreline observations are becoming an increasingly attractive component of operational shoreline prediction systems (Vitousek et al., 2023). The methods and models described herein might serve as an initial concept for components of a future, operational coastal-change monitoring and prediction system.

For the very first time, satellite-derived shoreline observations enable validation of model predictions over large spatial scales. Although the model, developed here, is *applied* over a large-scale, we believe the primary innovation of the study is that it is also *validated* over a large-scale (e.g., >1,000 km), which is unlike any other study to date (to our knowledge). We believe that the satellite-based coastal monitoring renaissance may stimulate a renaissance in model prediction. In the past few decades, innovation in coupled coastal hydrodynamic and morphodynamic models has primarily come in the form of resolving more physical processes, notably wave-driven water levels (in incident and infragravity bands; e.g., Sherwood et al.,

2021). Innovations to improve the fidelity of coastal physics-based models have had a noticeable impact on the skill of coastal-change simulations during individual storm events, but so far have arguably not had the same effect on long-term simulation of beach processes. On the other hand, simplified, parametrized, and increasingly probabilistic coastal change models, which are most often based on the concept of 'equilibrium' (e.g., Wright & Short, 1985, Miller & Dean, 2004, Yates et al., 2009, Davisdon et al., 2013, Hunt et al., 2023), have provided the biggest recent innovation in prediction of long-term (e.g., multi-annual to decadal+) coastal change. Although both physics-based and parameterized (reduced-complexity) coastal-change models will benefit from increased availability of observations, we believe the simplified models will receive the greatest returns from data-integration efforts for a number of different reasons: (1) simplified models can be readily calibrated to real-world, site-specific shoreline observations in contrast to more expensive, monolithic models, which also require full bathymetric and topographic surveys for validation, (2) simplified models, mainly due to their significantly shorter runtimes, can be readily applied in a probabilistic sense (e.g., using Monte Carlo methods), and thus will excel in propagating, quantifying, and balancing uncertainty (in both modeling and observational components) in contrast to more expensive and consequently more deterministic models, (3) simplified models can be readily adapted to produce multi-model ensemble predictions, and (4) simplified models are amenable to data-assimilated operational modeling (e.g., based on ensemble Kalman filter methods) as well as scenario-based modeling of future coastal change.

The hybridization of models and observations for coastal-change prediction is becoming increasingly viable because of earth-observing satellites. For the first time, satellites can provide coastal *data at the scales of models* and *models at the scales of data* (Vitousek et al., 2023). And

eventually, with perhaps another decade of research and development, the field could develop coupled monitoring and modeling systems at national to global scales.

In the current application, the developed CoSMoS-COAST model achieves an average RMSE of ~12 m, obtained by comparing model versus satellite-derived observations during a validation period of 2015-2020, averaged over the entire California coastline. We consider this level of accuracy to be quite remarkable (given the scale of shoreline projections in the current application) since the model's performance metrics seem to be on par with the performance achieved in notable, site-specific modeling applications (e.g., Montaño et al., 2020). Furthermore, the accuracy of the model seems to be on the same order of the accuracy of the satellite observations themselves. It is quite likely that the model's RMSE is even lower than the numbers reported here (in Figure 10) due to the limited accuracy of the satellite-derived shorelines used for validation. However, this is only a speculation, as no other (non-satellite) observations exist over equivalent spatiotemporal scales to verify these potential gains in accuracy. In support of this notion, we turn to the case study at Ocean Beach, a relatively limited area covering ~5 km of coast, but where monthly data have been collected over 2 decades. In the case study, presented here, for the 5-year validation period from 2015 to 2020, the model's error is ~15-20% higher (~3-4 m higher RMSE) when using satellite-derived shoreline observations for validation than when using highly accurate GPS observations for validation (see Figure 8 panels A vs. B).

Even though the satellite-data-calibrated model is roughly as accurate as the GPS-data-calibrated model, the model is still not perfect. It is possible that the post-calibration inaccuracies of the model may have more to do with the limitations of model itself rather than the quality/quantity of

calibration data or lack thereof (especially when two decades of calibration is applied). For example, non-stationarity in the shoreline model parameters, i.e., the potential for model parameters to change over time (e.g., Ibaceta et al., 2020), which is not accounted for here, may lead to drifts between model projections and the real world. Additionally, although the model is proven to be capable of resolving important signals of coastal change, it does not explicitly capture a number of important coastal change processes such as the formation and evolution of large-scale (~200-1,000 m) sand waves, fluvial-discharge events, cliff/bluff failures, headland bypassing, or other processes that can cause either pulses/shocks of coastal change or slow-varying, atypical oscillations. However, these issues are certainly not unique to the current model but persist for nearly all flavors of coastal-change models due to the dogged complexity of nearshore and subaerial sediment transport. Despite some of the recent improvements adopted in the latest CoSMoS-COAST model (including the changes in the governing equations and the adoption of an ensemble-based approach as described in Vitousek et al., 2021 as well as the data-assimilation advancements detailed in Appendix B), the physics of the current modeling application is nearly identical to the initial model development (Vitousek et al., 2017). The three most significant developments of the modeling efforts presented here are: (1) the scale of the model (i.e., southern California vs. all of California), (2) the integration of satellite-derived shoreline observations, and (3) the novel data-assimilation method. Further, these developments are complementary: the scale of data-assimilated modeling efforts is tightly linked with the scale of available data. We believe it is these three developments (and not really any improvement in the model physics) that have enabled *better predictions* (e.g., assimilating far more observations across much larger scales) over previous works.

Although the physics captured in the governing equations of the present model are mostly adequate to capture the dominant beach processes in California, numerous improvements might still be integrated into the current model. We suggest that an important component of coastal change that is not resolved explicitly in the California model is sediment flux from terrestrial sources, notably rivers. Warrick et al.'s (2022) "Fire plus flood equals beach" (using the same CoastSat-derived shoreline observations) analyzed beach accretion events at Big Sur, California following record-setting precipitation events, which followed a wildfire that burned 66% of the adjacent watershed. Warrick et al.'s (2022) paper was one of the first attempts to estimate the fluvial portion of a littoral sediment budget using satellite-derived shoreline observations. A modeling effort to better quantify fluvial sediment input to the coast as a function of terrestrial/watershed processes, while accounting for its significant temporal variability (East et al, 2018), is a particularly compelling endeavor and it could possibly be scaled up over the size of the U.S. West Coast (or even worldwide). Although the current shoreline model is only forced by nearshore hydrodynamic processes, it could possibly be extended to explicitly account for fluvial/terrestrial processes via coupling with terrestrial models. For example, future research might identify signatures of fluvial-discharge events and/or beach nourishments in satellite-derived shoreline observations (e.g., via machine learning) and subsequently parameterize or calibrate their occurrence (in both a hindcast and forecast sense with the aid of terrestrial-process models and GCM projections). The alternative approach (used here), to model fluvial, anthropogenic, or unresolved processes implicitly via a residual, linear shoreline-change rate (see term 3 in Eq. (1)), which can mask chronic erosion of nourished beaches (Armstrong & Lazarus, 2019), was previously taken out of necessity, given the sparsity of coastal observations. However, with the increasing availability of satellite-derived shoreline observations, the

motivation to explicitly resolve both the nearshore hydrodynamic and terrestrial components of coastal change substantially increases. In California, in particular, the sources and magnitudes of sediment input remain critical gaps in littoral sediment budgets and in the long-term survival of beaches (particularly those in natural settings) in response to sea-level rise (Warrick et al., 2023). In highly urban settings/environments (which are generally without significant fluvial-sediment input), we believe that the survival of beaches in urban environments will increasingly rely on beach nourishment and/or sand retention (Griggs et al., 2020). Yet, better satellite observations (with increasingly higher image quality and quantity) and better satellite-data-assimilated modeling predictions (such as those developed in the current paper) will be critical to design and monitor the effectiveness of engineering interventions and nature-based solutions.

5. Conclusions

We have developed and applied a large-scale, long-term shoreline change modeling system across 1,350 km of coast in California, home to a variety of different coastal geomorphic settings. For the first time, the model assimilates data from satellite-derived shoreline observations (derived from the CoastSat toolbox), providing a thousand-fold increase in assimilation data over traditional Lidar and GPS shoreline observations across the California coastline. In a case study at Ocean Beach, California, where extensive in-situ field monitoring efforts have taken place, we demonstrate that the assimilation of satellite-derived shorelines provides comparable predictive accuracy to a model with decades of monthly in-situ surveys. This case study provides confidence that satellite-derived shorelines, available anywhere in the world, can be used to calibrate and validate models of coastal change. Across California, during

a validation period of 2015-2020, the model achieves an average RMSE of ~12 m and an index of agreement of 0.54 when compared to satellite observations. The assessed accuracy of the California model is comparable to many state-of-the-art blind tests of multi-model shoreline prediction capabilities at well-monitored individual sites elsewhere in the world (e.g., Montaño et al., 2020). The model predictions, although subjected to considerable uncertainty, indicate that significant impacts to the shoreline may occur due to accelerated sea-level rise, with 25 to 70% beaches across California lost by 2100 under the 0.5 to 3.0 m SLR projections. It is likely that many beaches in California will require substantial management efforts (e.g., beach nourishments, sand retention, armoring, dune restorations as well as other engineering and nature-based solutions) in order to maintain existing beach widths and the many services they provide.

Acknowledgements

We would like to thank Tiffany Anderson and Mohsen Taherkhani for conducting internal reviews of this manuscript. We thank the three anonymous journal reviewers and the editors for their comments and suggestions, which lead to a significant improvement of this manuscript. This work was funded by the USGS Coastal and Marine Hazards and Resources Program. Any use of trade, firm, or product names is for descriptive purposes only and does not imply endorsement by the U.S. Government.

Data availability statement

The satellite-derived shorelines used in this study are available online at http://coastsat.wrl.unsw.edu.au/ . Data and models, produced as part of this study, are available, for purposes of peer review only, at: https://drive.google.com/drive/folders/1ipaiW9ap9TMJvF-qUQBRTh3CBM6gtO1x?usp=share_link . Upon provisional acceptance of the manuscript and subject to USGS data and software review policies, the data and software produced as part of this study will be made publicly available on USGS ScienceBase and code.usgs.gov, respectively, with a Digital Object Identifier.

Appendix A: Numerical model

This appendix details the numerical solution of the governing equation of the CoSMoS-COAST model, Eq. (1), which closely follows that of Vitousek et al., 2017.

A.1.1 Longshore transport

The first term on the right-hand side of Eq. (1) is the alongshore convergence of the longshore sediment transport, where Q is the longshore sediment-transport rate, X represents the alongshore coordinate, and d_c is the depth of closure. A generalized expression for the longshore-transport rate is

$$Q = Q_0 \sin(2\alpha), \tag{8}$$

where Q_0 represents the magnitude of the longshore sediment-transport rate derived empirically and expressed as a function of wave and sediment properties (e.g., CERC (1984); Kamphuis (1991)). In the current implementation, we approximate the magnitude of the longshore-transport rate as $Q_0 \approx KH_s^2$, where H_s is the significant wave height at the offshore endpoint of

each model transect (which is calculated via nearshore wave models as described below in appendix C.1), and K is an aggregated parameter that is determined via data assimilation. The argument of Eq. (8), $\alpha = \alpha_{\text{wave}} - \alpha_{\text{shoreline}}$, represents the relative angle (in Cartesian convention) between the incident waves (with incoming direction θ in Nautical convention, which corresponds to a Cartesian angle $\alpha_{\text{wave}} = 270 - \theta$ as shown in Figure 13) and the shoreline angle, $\alpha_{\text{shoreline}}$ (Larson et al., 1997). The shoreline angle is given by

$$\alpha_{\text{shoreline}} = \text{atan}\left(\frac{\Delta y}{\Delta x}\right), \tag{9}$$

where x and y represent the real world (e.g., Universal Transverse Mercator - UTM) Cartesian coordinates of the shoreline, and $\Delta x_{k+1/2} = x_{k+1} - x_k$ and $\Delta y_{k+1/2} = y_{k+1} - y_k$ represent the differences (in easting and northing, respectively) between the shoreline-position coordinates on adjacent transects (as shown in Figure 13). Note that some variables exist on directly on the transects themselves (with integer values of subscripts k) and some variables exist at the midpoints between transects (with values $k+1/2$). When necessary, we apply one-dimensional (1-D) linear interpolation to translate variables from transects to midpoints and vice versa.

The model does not consider high-angle wave instability and the growth of shoreline features such as spits, sand waves, and capes (e.g., Ashton et al., 2001; Falques, 2003; van den Berg et al., 2012; Kaergaard and Fredsoe, 2013; Roelvink et al., 2020), which can lead to multivalued solutions to the shoreline position, Y, at a specific time. Further details on the longshore-transport component of the model are given in Vitousek et al. (2017).

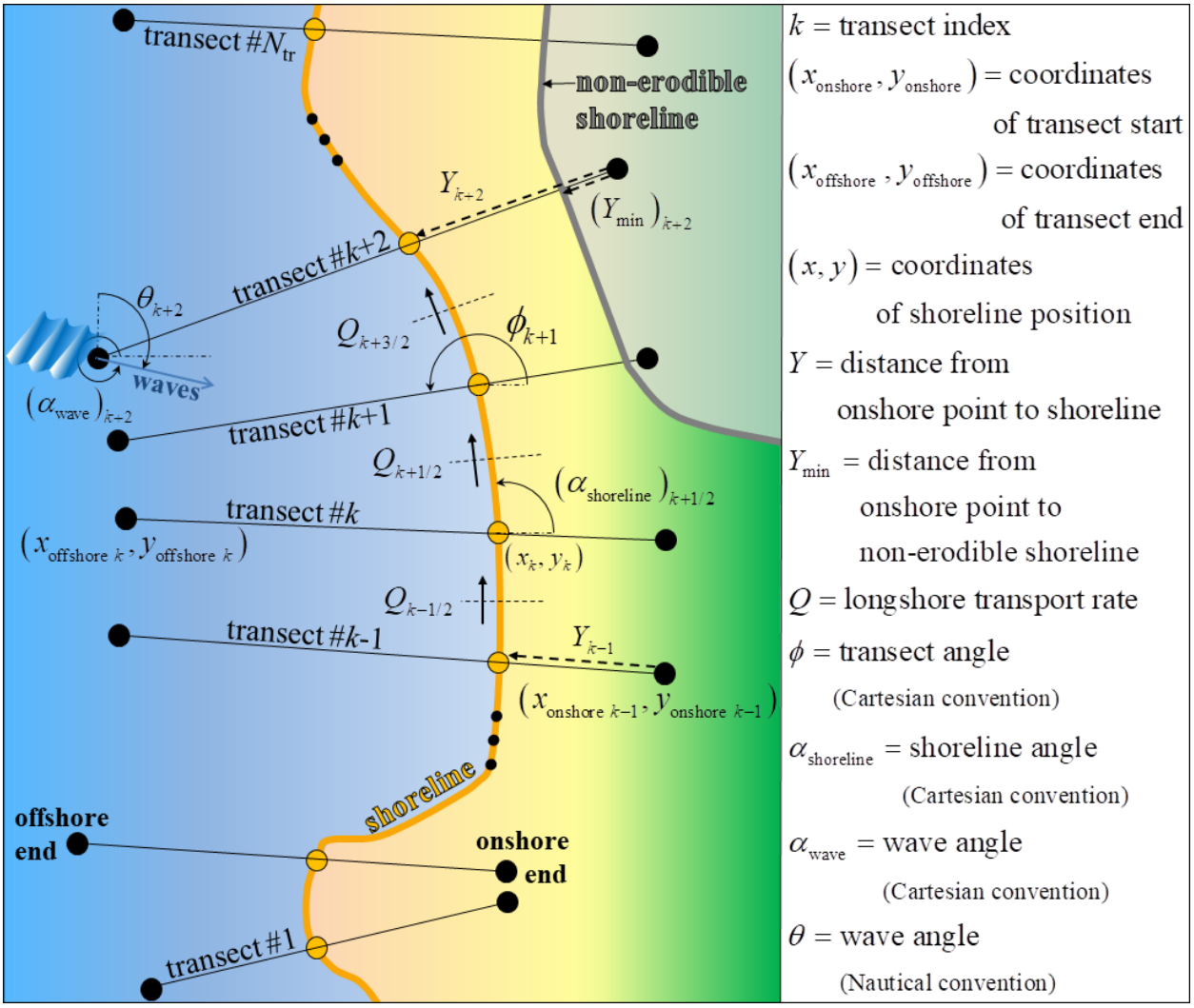

Figure 13 - Schematic showing the setup and some important variables of the transect-based CoSMoS-COAST model.

A.1.2 Shoreline recession due to sea-level rise

The second term on the right-hand side of Eq. (1) models shoreline recession due to sea-level rise (S). The $\tan\beta$ is the so-called the "transgression slope" (e.g., Wolinsky & Murray 2009), which represents the ratio of sea-level rise and the shoreline recession. The transgression slope is typically approximated using beach profile geometry. When $\tan\beta$ is chosen as the foreshore beach slope or the inland beach slope (e.g., Wolinsky & Murray 2009), this term represents the

shoreline recession in response to passive flooding. When the transgression slope is chosen as the average slope of the active beach profile extending to the depth of closure (commonly denoted as $\tan\alpha$), term [2] on the right-hand side of Eq. (1) represents the "classic Bruun rule" (Bruun 1962). The Bruun rule is widely used (Bruun, 1988) and modified (Davidson-Arnott, 2005; Wolinsky & Murray, 2009; Rosati et al., 2013; Young et al., 2014; Anderson et al., 2015, Davidson-Arnott & Bauer 2021), yet widely criticized (Cooper & Pilkey, 2004; Ranasinghe et al., 2012; Cooper et al., 2020) as an oversimplification of shoreline evolution. In the current implementation, the additional terms on the right-hand side of Eq. (1), e.g., terms [1] and [3]-[5], are intended to capture the processes missing from stand-alone applications of the Bruun rule. Despite criticism of the Bruun rule, there model remains widely used because there is "no simple, viable alternative" to it (Rosati, 2013). However, recent work (D'Anna et al., 2021b) proposed that the recession mechanism of the Bruun rule can be separated into two components: (1) shoreline recession due to passive flooding and (2) shoreline recession due to wave reshaping, which represents the cumulative effect of increased wave-driven erosion efficiency on a beach profile with an elevated sea-level state, which is captured via "equilibrium" shoreline-change theory in the fourth term on the RHS of Eq. (1). Recent validation studies of the Bruun rule have been carried out in both laboratory (Atkinson et al., 2018) and field (Troy et al., 2021, Davidson-Arnott & Bauer 2021) settings, which motivate the inclusion on the Bruunian shoreline recession model (along with an accompanying calibration coefficient c obtained from data assimilation) in the current application. Perhaps the biggest uncertainty in the application of the Bruun rule, is: what is the most appropriate "transgression slope" to apply? As in Vitousek et al. 2017, we apply a transgression slope ($\tan\beta$) that represents the foreshore beach slope between approximately -2.0 and +2.0 m around mean sea level, which translates to roughly a

1168 1/32 slope, when spatially averaged. However, in different coastal environments this
1169 transgression slope may differ significantly from that used here.

1170 *A.1.3 Long-term shoreline trend*

1171 The third term on the right-hand side of Eq. (1) is the long-term, residual shoreline trend that
1172 represents persistent processes such as sources and sinks of sediment from fluvial inputs (Inman
1173 and Jenkins, 1999; Willis and Griggs, 2003; Warrick and Mertes, 2009), nourishments (Flick,
1174 1993), cliff-failure (Young et al., 2011; Limber and Murray, 2011), aeolian transport (Bauer et
1175 al., 2009), sand mining (Thornton et al., 2006), and transport from offshore (Schwab et al.,
1176 2013). Regions dominated by these unresolved, residual effects will have locally high values of
1177 v_{lt}.

1178 In Eq. (1), if the long-term trend, v_{lt}, is a constant, then the shoreline migration is linear in time.
1179 Shoreline-change analyses using historical aerial photos often use linear regressions to fit
1180 observed shoreline data and determine long-term annual erosion rates (e.g., USGS National
1181 Assessment of Shoreline Change - Hapke et al., 2006). The data-assimilation method assumes
1182 that v_{lt} is constant, with initial value that is proportional to the linear regression rate $\left(v_{\mathrm{lt}}\right)_0$.
1183 However, when each data-assimilation step takes place, the magnitude of v_{lt} changes and thus
1184 the unresolved, long-term shoreline change is time-dependent. During the model forecast period
1185 when there are no observations available to assimilate, v_{lt} remains constant (as set by the
1186 sequential data-assimilation method at the end of the calibration period), and therefore the
1187 unresolved, long-term shoreline change associated with this term is linear in time. Consequently,

the long-term component is subject to error when chronic, unresolved processes result in a nonlinear, future shoreline response (Armstrong & Lazarus 2019).

A.1.4 Wave-driven cross-shore equilibrium transport

The fourth term on the right-hand side of Eq. (1) represents the Yates et al. (2009) equilibrium shoreline model that simulates episodic beach erosion and recovery during periods of high and low waves, respectively. Vitousek et al. (2021) reformulated the Yates et al. (2009) model to introduce parameters with intuitive meanings and dimensions (e.g., length or time), while retaining exactly the same model dynamics. In Eq. (1), the equilibrium shoreline position is given by

$$Y_{\text{eq}} = -\Delta Y \frac{H_s^2 - \left(H_s\right)_b^2}{\left(H_s\right)_b^2} \tag{10}$$

and the equilibrium time scale is given by

$$\tau = \Delta T \left(\frac{H_s}{\left(H_s\right)_b} \right)^{-1} \tag{11}$$

where $\left(H_s\right)_b$, ΔY, and ΔT, are free parameters, detailed in Vitousek et al. (2021) and briefly summarized below. In Eqs. (10)-(11), $\left(H_s\right)_b$ is the background wave-height parameter, which bears a close resemblance to the average of the wave-height time series. The term ΔY is the characteristic cross-shore erosion/accretion length-scale parameter, which is typically $\mathrm{O}(1-10\ \mathrm{m})$, and ΔT is the background equilibrium time-scale parameter, whose magnitude is typically on the order of several weeks. Note that, in Eq. (11), the instantaneous time scale τ

effectively becomes longer or shorter than the background time scale ΔT during small or large wave conditions, respectively, relative to the background wave height.

A.2 Spatial discretization (model transects)

In the proposed model, the coastline is discretized into a series of nodes that exist on shore-normal transects that are arbitrarily spaced in the alongshore direction. For each transect, the shoreline position at a given time step is measured by the distance, Y, from the onshore end of the transect. The model computes the evolution of Y for each transect. Accordingly, the shoreline evolves as if "on rails" represented by each transect. A schematic of the model domain is shown in Figure 13. Although there are long-term coastal evolution models that are grid based (e.g., the Coastal Evolution Model (CEM) – Ashton & Murray, 2006, LX-shore – Robinet et al., 2018) and vector-based (Hurst et al., 2015) or free-form (Roelvink et al., 2020), the current model is chosen to be transect based to cover long, irregular coastlines and facilitate the composition of the 1-D, process-based models (described above) with data assimilation.

For the current application, the domain is discretized into 11,539 transects spaced approximately 100-200 m apart (Figure 2). Each transect is assigned a designation of either "full model", "cross-shore only", "rate only", "cliff only" or "no prediction" based on geologic characteristics (which occur for 31.9%, 18.2%, 30.6%, 12%, and 7.3% of the California coastline, respectively). Based on the transect designation, the shoreline model retains or neglects certain physical processes and the corresponding terms in the governing equation, Eq. (1). As the name implies, transects designated as "full model" evolve the shoreline using the full governing equation, Eq. (1). "Full model" transects are selected for long, sandy beaches, and all model components are included. Small (< 1 km), sandy barrier islands or pocket beaches are designated as "cross-shore

only" by setting $K = 0$. The model also designates cobble beaches and heterogeneous sandy/rocky beaches as "rate only" transects by neglecting longshore and cross-shore transport due to waves, i.e., setting $K = 0$ and $\Delta Y = 0$. These transects evolve the shoreline using a linear change rate (obtained via data assimilation) plus a recession rate due to excess passive flooding above the current rate of SLR (Anderson et al., 2015). Finally, "cliff only" and "no prediction" transects represent sea-cliffs (without fronting beaches) or armored shorelines, respectively, where no model calculations are performed.

A.3 Temporal discretization

The model uses explicit Euler time stepping (e.g., Moin, 2010) for the cross-shore transport terms due to waves, sea-level, and long-term effects. However, these terms generally do not exhibit much susceptibility to numerical instability. The longshore-transport term, on the other hand, is susceptible to numerical instability based on the Courant number condition $\Delta t < \frac{\Delta X^2 d_c}{4Q_0}$ (Ashton & Murray, 2006; Vitousek & Barnard, 2015). Hence, the transect spacing, ΔX, is generally the most important consideration in selecting the preferred model time step. In general, explicit Euler time stepping suffices for transects spaced approximately 50 m or greater. To avoid potential numerical instability the model optionally uses a split-explicit method (e.g., Debreu et al., 2012) to subcycle the longshore-transport term with an integral time-refinement factor.

A.4 Split model equations

To facilitate model construction and data assimilation, Eq. (1) is split into individual components of shoreline change Y_{lst}, Y_{bru}, Y_{vlt}, and, Y_{st}, which represent shoreline change components on each individual transect driven by the individual terms [1]-[4] in Eq. (1). The total shoreline position is given as

$$Y = Y_{\text{lst}} + Y_{\text{bru}} + Y_{\text{vlt}} + Y_{\text{st}} + Y_0 \quad , \tag{12}$$

where Y_0 is the initial (observed) shoreline position.

This splitting procedure ensures that the equilibrium shoreline position, Y_{eq}, given in Eq. (1), is correctly associated with the variability of the short-term shoreline position, Y_{st}, following Long & Plant (2012). Further, this splitting procedure allows easy identification of the dominant components involved in the overall coastal change.

The split model equations become

$$\frac{\left(Y_{\text{lst}}\right)_k^{n+1} - \left(Y_{\text{lst}}\right)_k^n}{\Delta t} = -\frac{1}{\left(d_c\right)_k} \frac{Q_{k+1/2}^{n+\theta} - Q_{k-1/2}^{n+\theta}}{\Delta X_k} \tag{13}$$

$$\frac{\left(Y_{\text{bru}}\right)_k^{n+1} - \left(Y_{\text{bru}}\right)_k^n}{\Delta t} = -\frac{c_k}{\tan\beta_k} \left(\frac{\partial S}{\partial t}\right)_k^n \tag{14}$$

$$\frac{\left(Y_{\text{vlt}}\right)_k^{n+1} - \left(Y_{\text{vlt}}\right)_k^n}{\Delta t} = \left(\nu_{\text{lt}}\right)_k \tag{15}$$

$$\frac{\left(Y_{\text{st}}\right)_k^{n+1} - \left(Y_{\text{st}}\right)_k^n}{\Delta t} = \frac{1}{\tau_k} \left(\left(Y_{\text{eq}}\right)_k^n - \left(Y_{\text{st}}\right)_k^n\right) \tag{16}$$

where superscripts n represent the time-step index, Δt is the time step, k represents the transect index, and ΔX_k the distance between adjacent transects. In Eq. (13), the superscript variable $\theta = 0$ or $\theta = 1$ represents the use of explicit versus implicit time stepping, respectively, following the method of Vitousek & Barnard (2015). All of the model parameters and variables in Eqs. (13) - (16) are defined at each transect (with index k) except the longshore transport rate, Q, which is located between adjacent transects (with indices $k \pm 1/2$). Although the splitting procedure in Eqs. (13) - (16) seems to result in an "uncoupled" model, the model still accounts for feedbacks between the individual shoreline components since the longshore-transport term (see Eqs. (8) - (9)) is calculated using the shoreline angle associated with the full shoreline position Y.

Appendix B: Data assimilation

The original data-assimilation method used in CoSMoS-COAST (Vitousek et al. 2017) operated independently for each transect. Here, we develop novel data-assimilation method (described in this appendix) that uses all observations within a littoral cell (at a given time step) to assimilate the model parameter values for all transects within that littoral cell. To accomplish this, the data assimilation method uses a global state vector (containing all state variables/parameters) rather than a local (transect specific) state vector as described in B.1, combined with a novel localization method described in B.3.

B.1 Model state vector

Data assimilation automatically adjusts the model state (i.e., the model solution and parameters) during runtime to best fit any available observed data at the concurrent time step. In the current

application, the state vector representing the model solution and parameters (at a given transect k) that is adjusted via data assimilation is given by

$$\vec{x}_k = \left[\left(Y_{\text{lst}}\right)_k \quad \left(Y_{\text{st}}\right)_k \quad \Delta T_k \quad \Delta Y_k \quad \left(\hat{H}_s\right)_k \quad c_k \quad \left(v_{\text{lt}}\right)_k \quad K_k \quad \sigma_k \right]^T . \tag{17}$$

Eq. (17) includes the important model parameters and two model solution variables (Y_{lst} and Y_{st}) for a total of $N_{\text{var}} = 9$ variables, in this case. Note that, in the context of the current model, the assimilation of any parameter in the state vector in Eq. (17) can be effectively turned off by removing the variance of that parameter across the ensemble (i.e., by applying a constant value of the model parameter), which implies perfect confidence in the value of that parameter. Although the total shoreline position (given in Eq. (12)) is composed of other components, i.e., Y_{bru}, and Y_{vlt}, we do not seek to assimilate (i.e., adjust) the values of these components, since, according to Eqs. (14) and (15), they represent quasi-deterministic model components (i.e., they are generally monotonic and their governing equations allow them to be uniquely determined from independent variables such as the amount of sea-level rise or time, respectively) rather than dynamic components (like Y_{lst} and Y_{st}). Note, however, that the model parameters like c and v_{lt} that influence the evolution of Eqs. (14) and (15) are assimilated.

Eq. (17) presents a slight simplification of the state vector used in CoSMoS-COAST. As discussed in Vitousek et al. (2017), the native data-assimilation method does not guarantee that the model parameters retain their requisite sign (for example, $\Delta T, \Delta Y, \hat{H}_s, c, K, \sigma$ are positive quantities). Hence, we modify the state vector slightly (following Vitousek et al., 2017) to assimilate the natural logarithm of positive-valued model parameters, which are then converted (via the exponential function) back to its original form following the data assimilation step.

Following Eqs. (13) - (17), the evolution equation of the state vector is given by

$$\frac{\partial \vec{x}_k}{\partial t} = \frac{\vec{x}_k^{n+1} - \vec{x}_k^{n}}{\Delta t} = \begin{bmatrix} -\frac{1}{(d_c)_k}\frac{Q_{k+1/2}^{n+\theta} - Q_{k-1/2}^{n+\theta}}{\Delta X_k} \\ \frac{1}{\Delta T_k}\left(\left(Y_{\text{eq}}\right)_k^n - \left(Y_{\text{st}}\right)_k^n\right) \\ 0 \\ 0 \\ 0 \\ 0 \\ 0 \\ 0 \\ 0 \end{bmatrix} = \mathbf{f}_k^n \tag{18}$$

Eq. (18) has zero right-hand-side terms, $\frac{\partial \vec{x}}{\partial t} = 0$, for the evolution of the seven model parameters, $\Delta T, \Delta Y, \hat{H}_s, c, v_{\text{lt}}, K, \sigma$, that represent spatially-variable, yet temporally-constant coefficients, which are updated at each data-assimilation step. Note that in Eq. (18), terms with superscript n (i.e., $Q^{n+\theta}$ and $\left(Y_{\text{eq}}\right)^n$, which are functions of the wave forcing conditions, $\left(H_s\right)^n$) are variable in time. On the other hand, terms without superscript n are assumed to be constant with time in the absence of data assimilation (e.g., $\Delta T, \Delta Y, \hat{H}_s, c, v_{\text{lt}}, K, \sigma$ as well as the unassimilated parameters d_c and $\tan\beta$), although in reality the processes that these parameters seek to represent can exhibit some variability in time, inevitably resulting in model error. For the original CoSMoS-COAST model (Vitousek et al., 2017), the data-assimilation method in Eq. (18) took place independently for each transect k, meaning that the model for a given transect only accounted for shoreline observations falling on that individual transect at that instance in time. The current method, however, assimilates an augmented state vector $\vec{x}_a$ for all transects that is given by

$$\vec{x}_a = \left[\vec{x}_1^T \quad \vec{x}_2^T \quad \cdots \quad \vec{x}_k^T \quad \vec{x}_{k+1}^T \quad \cdots \quad \vec{x}_{N_{\text{tr}}}^T \right]^T \tag{19}$$

The (global) augmented state vector $\vec{x}_a$ (which is of size $\left(N_{\text{tr}} \times N_{\text{var}}\right) \times 1$) in Eq. (19) contains the $N_{\text{var}} \times 1$ state vectors (with $N_{\text{var}} = 9$) given in Eq. (17) for all (N_{tr}) model transects.

It is often desirable to assimilate site-specific behavior from site-specific observations. However, assimilating each transect independently does not leverage the spatial coherence that exists between adjacent observations. As discussed below in Section B.3, we seek a compromise between data quantity and data locality by implementing a so-called 'localization' method to prioritize assimilation of coincident and neighboring observations.

B.2 Ensemble Kalman filter data-assimilation method

Here, we utilize an ensemble Kalman filter (EnKF) data-assimilation method following Evensen (1994). The EnKF data-assimilation method evolves an ensemble of the (augmented) model state vector,

$$\mathbf{x} = \left[\left(\vec{x}_a\right)_1 \quad \left(\vec{x}_a\right)_2 \quad \cdots \quad \left(\vec{x}_a\right)_{N_{\text{ens}}} \right], \tag{20}$$

where each (augmented) state vector $\vec{x}_a$ of the N_{ens} member ensemble contains the combination of the model solution and parameters (as in Eqs. (17) and (19)). Note that throughout this appendix, boldfaced quantities (e.g., $\mathbf{x}$) indicate an ensemble quantity or matrix (with dimensions provided where possible). The assembly of the model state vector ensemble (i.e., Eqs. (17), (19), and (20)) is illustrated in Figure 14.

The EnKF method sequentially adjusts the model state during the simulation to best fit any available shoreline observations at the concurrent time step, via an optimal interpolation that accounts for the uncertainty of both model and observations. The procedure of the data-assimilation method is given by:

1. Run the forward model with added noise:

$$\mathbf{x}^{*} = \mathbf{F}\left(\mathbf{x}^{n}\right) + \boldsymbol{\varepsilon}_{\text{mod}} \tag{21}$$

where $\mathbf{x}^{*}$ is the $\left(\left(N_{\text{tr}} \times N_{\text{var}}\right) \times N_{\text{ens}}\right)$ ensemble of the forecasted state vector (e.g., Eq. (17)), $\mathbf{x}^{n}$ is the ensemble of the model state vectors at time step n, $\mathbf{F}$ is the operation of the (forward) model for a single time step (i.e., $\mathbf{F}\left(\mathbf{x}^{n}\right) = \mathbf{x}^{n} + \Delta t \mathbf{f}^{n}$ where $\mathbf{f}^{n}$ is given in Eq. (18)) and $\boldsymbol{\varepsilon}_{\text{mod}} \sim \text{N}\left(0, \sigma^{2}\right)$ is a sample of random, normally-distributed noise with zero mean and user-prescribed standard deviation σ, which can vary for each parameter and is added to the model forecast. Vitousek et al. (2021) demonstrated that the additive noise parameter σ plays an extremely important role in the specification of the epistemic uncertainty (i.e., the user-specified accuracy limits of the model).

In the absence of data to assimilate, $\mathbf{x}^{n+1} = \mathbf{x}^{*}$, and the inverse model (i.e., the data-assimilation method computed via steps 2-5 below) is not computed, and the model state vector at time step $n+1$ is simply that which is predicted by the (forward) model. In the current application, when data are no longer available to assimilate (i.e., during a forecast period), then $\boldsymbol{\varepsilon}_{\text{mod}}$ is set to zero, and the ensemble is propagated forward without additive noise, $\mathbf{x}^{n+1} = \mathbf{F}\left(\mathbf{x}^{n}\right)$, as is nominally the case for unassimilated models.

2. Calculate the background model ($\mathbf{X}^*$) and (model-predicted) observation ($\mathbf{Y}^*$) anomalies about the ensemble average, according to

$$\mathbf{X}^* = \mathbf{x}^* - \bar{\mathbf{x}}^* \tag{22}$$

$$\mathbf{Y}^* = \mathbf{y}^* - \bar{\mathbf{y}}^* \tag{23}$$

where $\bar{\mathbf{x}}^*$ and $\bar{\mathbf{y}}^*$ are the ensemble averages of $\mathbf{x}^*$ and $\mathbf{y}^*$, respectively. In Eqs. (22) and (23), $\mathbf{X}^*$ and $\mathbf{Y}^*$ are ensembles of size $\left(N_{\text{tr}} \times N_{\text{var}}\right) \times N_{\text{ens}}$ and $N_{\text{obs}} \times N_{\text{ens}}$, respectively, where N_{obs} is the number of transects with observations to assimilate at a given time step. It is important to note that here the variable $\mathbf{y}^*$ does not represent actual observations. Instead, $\mathbf{y}^* = H\left(\mathbf{x}^*\right)$ represents the ensemble of model-predicted variables that coincide with the observed variables (e.g., at their given spatial locations), where H is an interpolation operator that ensures that the model output and observations are co-located.

3. Calculate the combined error covariance matrix

$$\mathbf{P} = \underbrace{\rho\left(\frac{1}{N_{\text{ens}} - 1}\mathbf{Y}^*\left(\mathbf{Y}^*\right)^T\right)}_{\substack{\text{(inflated) model} \\ \text{covariance} \\ \text{matrix}}} + \underbrace{\mathbf{R}}_{\substack{\text{observation} \\ \text{covariance} \\ \text{matrix}}} = \rho\,\text{cov}\left(\mathbf{y}^*\right) + \mathbf{R} \tag{24}$$

which is a $N_{\text{obs}} \times N_{\text{obs}}$ matrix that represents the sum of the covariance of the model error and the observation error, where ρ is a so-called 'covariance inflation factor' (typically chosen to be $\rho = 1.1$, as is the case here) and $\mathbf{R}$ is the $N_{\text{obs}} \times N_{\text{obs}}$ covariance matrix of

observation error. Here we apply the approximate error covariance matrix ($\mathbf{R} = \tilde{\mathbf{R}}$) derived below in Eq. (34) of Section B.5. The weighting between model and observations (which accounts for the uncertainty of each source of error) is calculated below in Eq. (25). Compared with the *extended* Kalman filter (EKF) approach (used in Long & Plant, 2012, and Vitousek et al., 2017), Eq. (24) replaces the analytical derivation and advancement of the error covariance matrix $\mathbf{P}$, which is calculated from the Jacobian matrix (i.e., the matrix of partial derivatives) of the forward model $\mathbf{F}$. Hence, the EnKF method requires very little computational overhead and no analytical work to derive the Jacobian matrix, in contrast to the EKF method. However, the EnKF method does require running an ensemble of models as opposed to running a single model realization using the EKF. Running a model ensemble certainly increases the computational requirements, but it also enables modeling of a range of model parameters and forcing conditions, and thus a better accounting of uncertainty, which is often a desirable feature.

4. Calculate the so-called 'Kalman gain', $\mathbf{K}$, according to

$$\mathbf{K} = \frac{1}{N_{\text{ens}} - 1} \mathbf{X}^* \left(\mathbf{Y}^* \right)^T \mathbf{P}^{-1} \tag{25}$$

Here, $\mathbf{K}$ is a $\left(N_{\text{tr}} \times N_{\text{var}} \right) \times N_{\text{obs}}$ matrix (recalling that N_{tr} is the total number of model transects to assimilate, N_{var} is the number of variables in the assimilated state vector [Eq. (17)], and N_{obs} is the number of transects with observations to assimilate at the current time step). Eq. (25) requires the calculation of a matrix inverse (or the solution of a linear system of equations). However, this matrix inversion is typically quite affordable

since $\mathbf{P}$ is an $N_{\text{obs}} \times N_{\text{obs}}$ matrix, where N_{obs} is typically $\mathrm{O}(10-100)$ and is generally much smaller than N_{tr} (which is often $\mathrm{O}(1{,}000-10{,}000)$).

5. Apply a localization routine (described in the following section) to prioritize the influence of nearby observations on the data-assimilation procedure. This step adjusts the (global) Kalman gain, $\mathbf{K}$, according to $\mathbf{K}_{\text{loc}} = \mathbf{L}_{\mathbf{K}} \circ \mathbf{K}$, where $\mathbf{L}_{\mathbf{K}}$ is the localization matrix given in Eq. (28), which is motivated below in Section B.3.

6. Update the ensemble state vector according to

$$\mathbf{x}^{n+1} = \mathbf{x}^{*} + \mathbf{K}_{\text{loc}} \left(\underbrace{\left[\mathbf{y}_{\text{obs}}^{n+1} + \boldsymbol{\varepsilon}_{\text{obs}} \right]}_{\substack{\text{perturbed} \\ \text{observations}}} - \underbrace{\mathbf{y}^{*}}_{\substack{\text{model prediction} \\ \text{for the observed} \\ \text{locations/variables}}} \right) \tag{26}$$

where $\mathbf{x}^{n+1}$ is the final (analysis) state vector. Eq. (26) represents an 'optimal' interpolation between model and observations. Eq. (26) demonstrates that the $\left(N_{\text{tr}} \times N_{\text{var}}\right) \times N_{\text{obs}}$ (localized) Kalman gain matrix $\mathbf{K}_{\text{loc}}$ effectively scales/translates the mismatch between the observation ensemble (of size $N_{\text{obs}} \times N_{\text{ens}}$) and the model into adjustments made to the state vector $\mathbf{x}$ (with size $\left(N_{\text{tr}} \times N_{\text{var}}\right) \times N_{\text{ens}}$). Note that the bracketed term in Eq. (26) represents perturbation of the observed state vector, $\mathbf{y}_{\text{obs}}^{n+1}$, with the representative error/noise sampled from a multivariate normal distribution, $\boldsymbol{\varepsilon}_{\text{obs}} = \mathrm{N}\left(\mathbf{0}, \mathbf{R}\right)$.

The model and data-assimilation methodology are summarized in Figure 14.

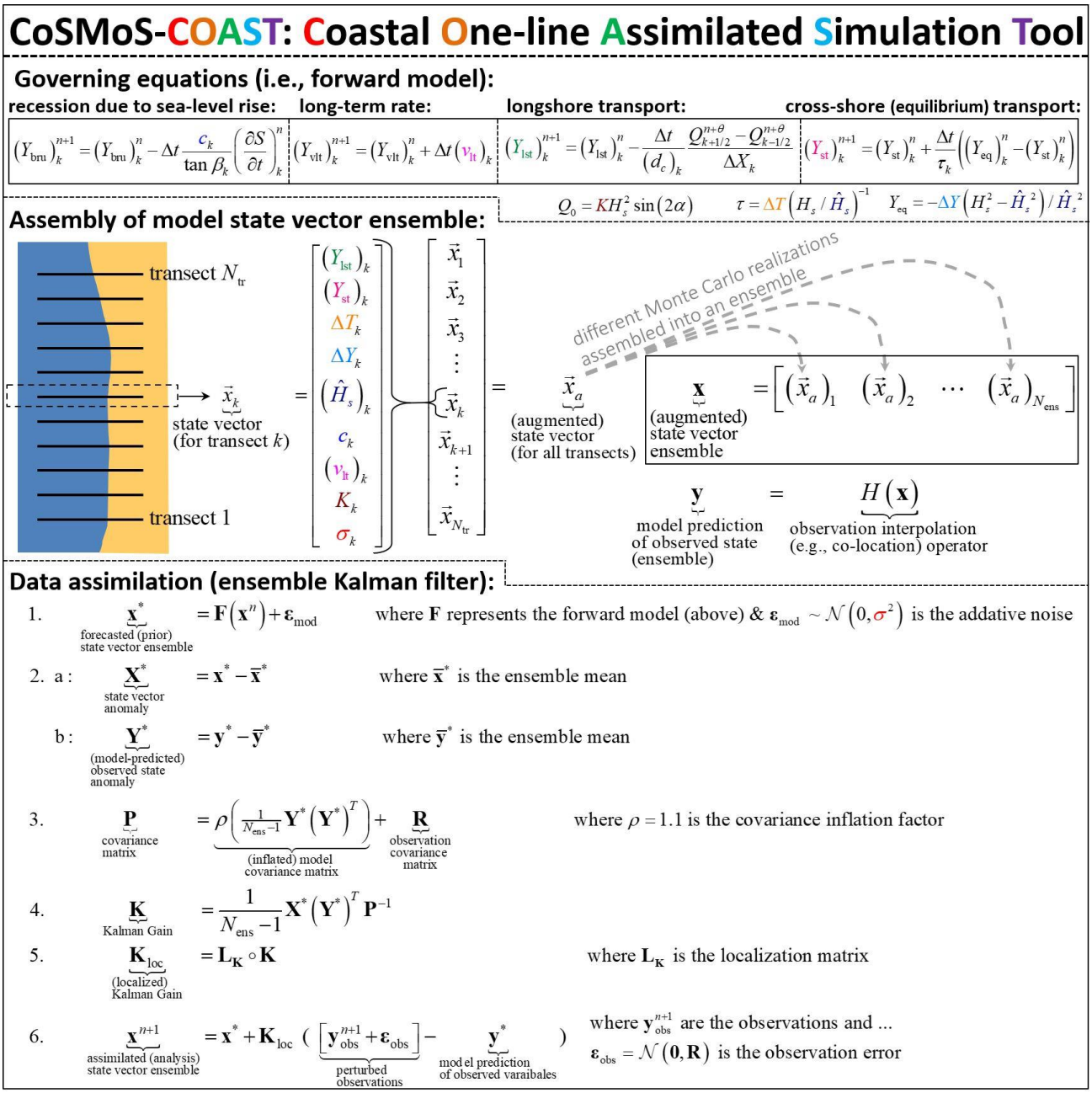

Figure 14 – Summary of the model and data-assimilation methodology, including the assembly of the state vector ensemble.

B.3 Localization

Localization is a commonly used method in data assimilation to prioritize the influence of nearby observations on the assimilated model state (Hamill et al., 2001). For many beaches located along the same broad stretch of coastline, we expect that observations of coastal change will be correlated due to the spatial choerence of the underlying geologic and oceanographic process (e.g., wave conditions) that force change. Localization methods prioritize data locality during the data assimilation step by suppressing the potential for spurious correlations in the model state across large spatial distances. In the context of the current work, localization is attractive because it effectively calibrates local shoreline behavior from local shoreline observations (while still utilizing as much data as possible). Further, because (satellite-derived) observations are generally available (i.e., with comparable temporal resolution) for all transects, we have the option to be "picky" when it comes to prioritizing site-specific data. For modeling applications in regions where beach profile data are available with far greater spacing than model transects (e.g., Ruggiero et al., 2016), the localization method can also provide a means of assimilating parameters for model transects in neighborhood of profile observations, without the need for the (model and observational) transects to overlap, for example.

The two most common localization techniques include *domain localization* and *covariance localization*. The former applies the data assimilation separately for individual, independent subdomains of the model. The latter artificially tapers the model error covariance matrix, i.e., the first term of Eq. (24), to suppress the influence of covariates that occur over large distances. In the present work, we apply a novel 'hybrid' localization method, which applies concepts from both domain and covariance localization methods. The developed localization method replaces

the (global) Kalman-gain matrix, $\mathbf{K}$, of size $\left(N_{\text{tr}} \times N_{\text{var}}\right) \times N_{\text{obs}}$ given in Eq. (26), with a localized Kalman-gain matrix $\mathbf{K}_{\text{loc}}$ (which is of the same size) and is given by:

$$\mathbf{K}_{\text{loc}} = \mathbf{L}_{\mathbf{K}} \circ \mathbf{K} \tag{27}$$

In Eq. (27), the $\circ$ operator represents the Hadamard (or element-wise) product between the original Kalman gain $\mathbf{K}$ (given in Eq. (26)) and $\mathbf{L}_{\mathbf{K}}$, which represents the localization matrix that given by

$$\mathbf{L}_{\mathbf{K}} = \mathbf{L}_{\text{obs}} \otimes e \tag{28}$$

In Eq. (28), $e = [1 \quad 1 \quad \cdots \quad 1]^T$ is a $N_{\text{var}} \times 1$ vector of all ones, and $\otimes$ is an operator representing the Kronecker product, which effectively "tiles" (i.e., replicates) the localization matrix $\mathbf{L}_{\text{obs}}$ for each of the N_{var} elements of the assimilated state vector in Eq. (17). In Eq. (28), $\mathbf{L}_{\text{obs}}$ is a $N_{\text{tr}} \times N_{\text{obs}}$ localization matrix that is derived by selecting only specific columns (corresponding to transects with co-located observations) from a global localization matrix $\mathbf{L}$ of size $N_{\text{tr}} \times N_{\text{tr}}$, which is given by

$$\mathbf{L} = 2^{-\frac{\mathbf{D}}{L_d}} \circ \mathbf{I}_{\text{cell}} \tag{29}$$

The first term in the product on the right-hand side of Eq. (29) applies the concept of covariance localization via a exponentially decaying function $f\left(x\right) = 2^{-x/L_d}$ (with decay distance corresponding to the alongshore distance between two transects, i.e., $L_d = 2$, in the present application) and $\mathbf{D}$ is the $N_{\text{tr}} \times N_{\text{tr}}$ transect separation distance matrix

$$\left(\mathbf{D}\right)_{i,j} = \left|i - j\right| \,, \tag{30}$$

where i and j represent transect indices. Although the same decay function, $f\left(x\right)$, and the same decay distance $L_d = 2$ are applied uniformly for all model parameters and all transects, the hybrid method presented here, permits the possibility that different model parameters or transects might be localized with different treatment (e.g., observations might be specified exert a stronger or weaker spatial influence on certain model parameters). However, the optimization of this approach is beyond the scope of this paper.

Eq. (29) also applies the concept of domain localization by introducing (user-specified or automatically defined) "littoral cells", which represent individual subdomains that isolate (i.e., localize) assimilated changes to the model state to come only from observations falling within the same littoral cell. In Eq. (29), the (global) littoral cell adjacency matrix $\mathbf{I}_{\text{cell}}$ of size $N_{\text{tr}} \times N_{\text{tr}}$ is used to implement domain localization, which represents the explicit introduction of (user-controlled) spatial structure into the data-assimilation method (which is otherwise controlled only by the (global) covariance of the model state, see Eq. (25)). In the current application, $\mathbf{I}_{\text{cell}}$ represents a Boolean matrix that is given by

$$\left(\mathbf{I}_{\text{cell}}\right)_{i,j} = \begin{cases} 1 & \text{if transect } i \text{ is within the same littoral cell as transect } j \\ 0 & \text{otherwise} \end{cases}$$

$\mathbf{I}_{\text{cell}}$ effectively sets many of the elements of the localized Kalman gain $\mathbf{K}_{\text{loc}}$ equal to zero for all model transects located in a different user-defined 'littoral cell' than the cell with observations currently being assimilated. In the context of the California application model, the 'littoral cells' (for the purposes of data assimilation) are defined as sets of transects that share a continuous

stretch of sandy beach with the same model-type designation (e.g., “full model”, “cross-shore only”, etc. as described in Appendix A) that are not interrupted by inlets, headlands, harbors, or large jetties, for example. In short, the method, detailed above, ensures that model parameter values are assimilated using observations that fall within the same littoral cell. Note that when the elements of the Kalman gain $\mathbf{K}_{\text{loc}}$ are zero, then the assimilation step does not alter the model state vector in Eq. (26), i.e., $\mathbf{x}^{n+1} = \mathbf{x}^{*}$, for all transect that are considered “non-local” to a given shoreline observation. Figure 15 depicts idealized versions of the $\mathbf{I}_{\text{cell}}$ matrix, the distance matrix $\mathbf{D}$, and the full localization matrix $\mathbf{L}$ for a subset of the model transects used here (i.e., transects #1-1200) for illustration purposes.

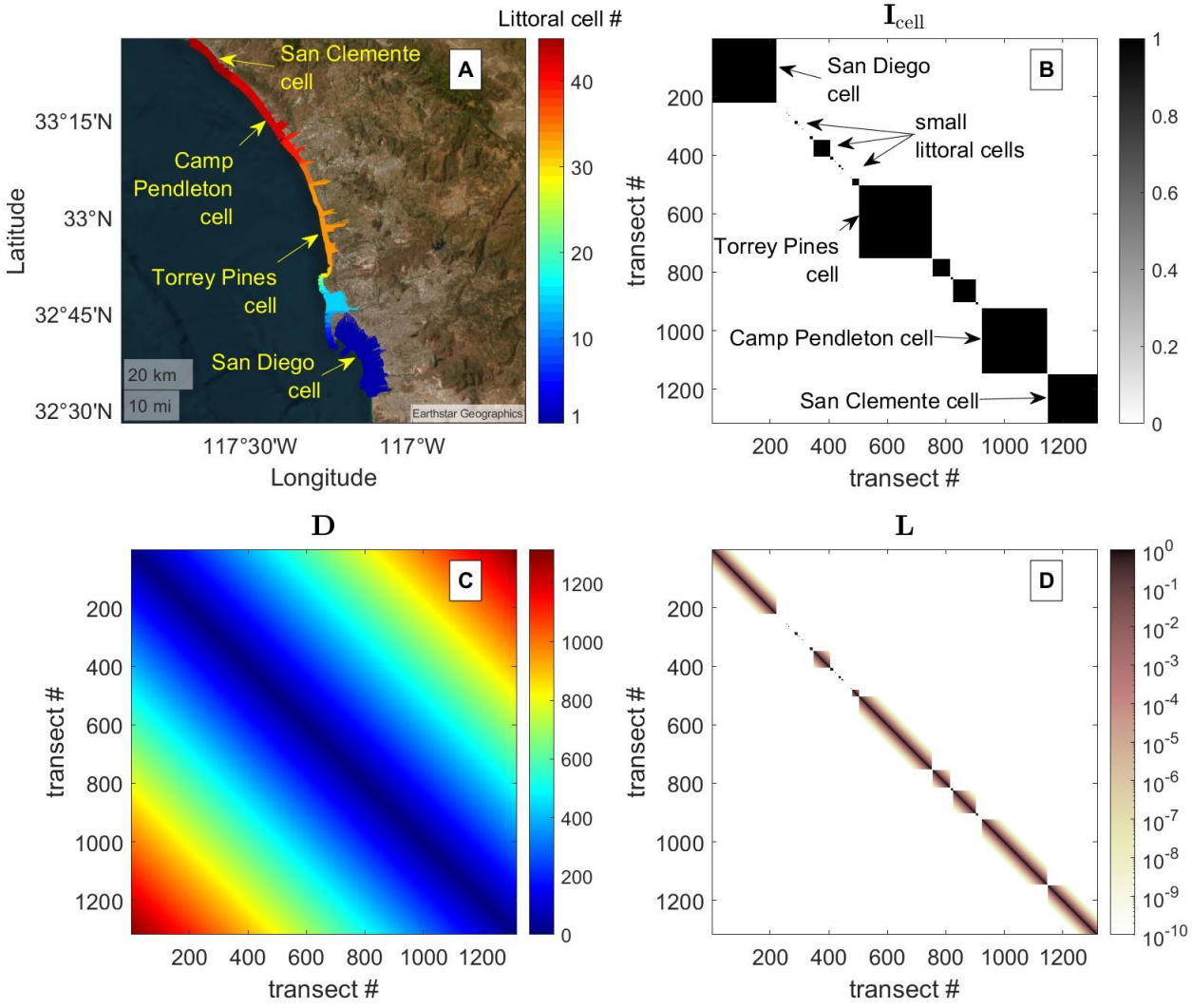

Figure 15 – The components (i.e., a map of the identified littoral cells in panel A, the littoral cell adjacency matrix $\mathbf{I}_{\mathrm{cell}}$ shown in panel B, and the transect-separation distance matrix $\mathbf{D}$ shown in panel C) of the localization matrix ($\mathbf{L}$) shown in panel C for the present application, which is shown only for a limited subset of the transects used here (i.e., transects #1-1200 in southern California). Note that the black blocks in panel B represent the connectivity of major littoral cells identified in the model, which are also shown in panel A.

B.4 Initial conditions for the model ensemble

The ensemble method presented here applies a user-specified range of randomly generated initial conditions of the model state, which are drawn from probability distributions. In general, the

selection process of the range of the initial values for each model parameter is a bit arbitrary and is subject to some uncertainty. Ideally, the initial range of model parameters should be motivated by the corresponding values of other modeling studies reported in the literature at geologically similar sites. Although the initial conditions must be specified directly, we find that a modest mis-specification (e.g., within an order of magnitude) of the initial parameter ensemble does not severely degrade the assimilated parameter estimates over time (Evensen, 2003). For most applications, initial conditions are sampled from normal distributions constructed from a prescribed mean and standard deviation. In the current application, the $N_{\text{ens}} = 200$ ensemble of the model state is initialized with normally-distributed random-number generator with zero mean and standard deviation $\sigma_{Y_{\text{st}}} = 5$ m for the short-term shoreline position, Y_{st}. On the other hand, the long-term shoreline components (namely Y_{lst}, Y_{bru}, and Y_{vlt}) are considered to be known initially and hence are set to be identically zero. The initial shoreline position Y_0 for each transect is also set to a constant value (obtained via nearest neighbor interpolation) that represents the observed shoreline position that is closest in time to the model start time among the complete set of observations for a given transect.

The model parameter ensemble is initialized with normal distributions for ΔT and ΔY with means of $\overline{\Delta T} = 28$ days and $\overline{\Delta Y} = 10$ m, and standard deviations of $\sigma_{\Delta T} = 1$ day and $\sigma_{\Delta Y} = 2$ m, respectively. The background wave height parameter $\hat{H}_s$ is initialized with a normal distribution with the mean wave-height time series on each transect ($\overline{H_s}$) and a standard deviation which is selected as 7.5% of $\overline{H_s}$, based on our judgment as a reasonable initial spread of this parameter. Alongshore smoothing (via a low-pass filter) of the background wave height $\hat{H}_s$ is also applied

in order to remove high frequency noise/variability in the model parameter (in the alongshore direction).

The model parameter ensemble is also initialized with normal distributions for c and σ with means of $\bar{c} = 1$ and $\bar{\sigma} = 0.25$ m, and standard deviations of $\sigma_c = 0.1$ and $\sigma_\sigma = 0.1$ m, respectively. The long-term shoreline change rate parameter v_{lt} is initialized with a normal distribution with a standard deviation of $\sigma_{v_{\mathrm{lt}}} = 0.05$ m/year and a mean of $\overline{v_{\mathrm{lt}}} = 0.25\left(v_{\mathrm{lt}}\right)_0$, where $\left(v_{\mathrm{lt}}\right)_0$ represents the historical erosion rate obtained via a linear regression fit to all available data on each transect (see Section 3.1 and Figure 5 for details). In setting the initial rate parameter to 25% of the historical (linear) erosion rate, we implicitly assume that the other resolved long-term components (e.g., longshore transport and Bruunian response) account for some (i.e., 75%) of the long-term shoreline change signal, as an initial guess. However, of course, the data-assimilation method will subsequently calibrate the relative parameters and the contributions of each shoreline-change component accordingly.

Thus far, we have detailed that all model state and parameter initial conditions are either constant or have been drawn from normal distributions. However, the longshore transport parameter K is treated differently: K is initialized with a uniform distribution between values of 0 and 200. In this case, a uniform distribution is applied to this parameter owing to its underlying uncertainty and spatial variability in contrast to the equilibrium shoreline parameters (ΔT, ΔY, and $\hat{H}_s$), the long-term parameters (c and v_{lt}), and the noise parameter (σ).

In addition to the procedure in specifying the initial conditions given above, we also impose longshore variability to the initial parameters ΔT, ΔY, and K. We introduce longshore

structure into the initial parameter ensembles by multiplying the initially longshore-uniform parameter estimate by a set of simple spatially varying 'basis functions' for each littoral cell. Although the basis functions are rather arbitrary, in the current example, we apply well-known Legendre polynomials (up to fourth order) and Fourier basis functions (half wave and full wave sin/cos functions), which are modified to have a unit mean and are shown in Figure 16 panels A and B, respectively, to construct an overall alongshore structure ensemble (shown in panel C) for each individual littoral cell. We also randomly scale the basis functions by $\sim \pm 25\%$, in order to introduce additional magnitude variability into the alongshore structure ensemble. The alongshore structure ensemble (shown in panel C) is then multiplied by the initial parameter estimates (for ΔT, ΔY, and K) for each separate littoral cell.

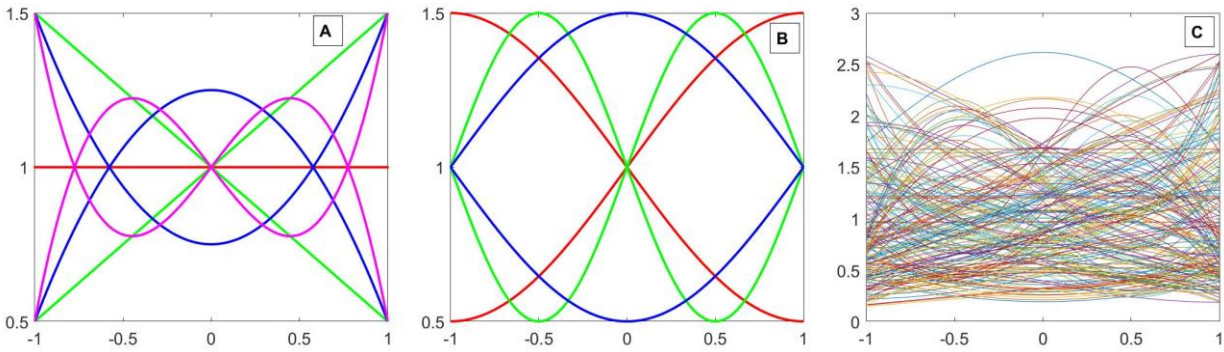

Figure 16 – Simple alongshore basis functions in the form of (modified) Legendre polynomials (panel A) and Fourier (half and full sin/cos) waves (panel B). An alongshore structure ensemble (panel C) is constructed from a random sampling and scaling of the simple basis functions shown in panels A and B. Subsequently, the longshore structure function (shown in panel C) is multiplied by the initial parameter estimates (for parameters ΔT, ΔY, and K only) for each separate littoral cell.

The introduction of a longshore structure ensemble into the initial conditions (as opposed to applying a spatially uniform ensemble) allows the model to encapsulate different possible

realizations of the longshore variability in the model parameters and thus is generally better conditioned to assimilate (i.e., to nudge the model toward) the correct underlying structure to emerge from the initially imposed gradients. Although the proposed method has not been fully tested or optimized (which is beyond the scope of the current paper), we find (from initial tests, which are not shown) that the longshore-structured, initial ensemble generally outperforms the alongshore-uniform initial parameter estimates. Further, we also note that even though the *ad hoc* initial longshore structure is imposed in a specific form (analogous to a best-guess initial condition provided to an optimization routine), the assimilated structure can eventually take on much more arbitrary complexity than that of the simple functions shown in panel C.

B.5 Observation error covariance

A user-defined specification of the spatial correlation (in the alongshore direction) of the error of satellite-derived shoreline observations is needed for the Kalman filter data-assimilation operation (described above). Lacking observations of the shoreline error covariance in the alongshore direction, the observation error covariance matrix $\mathbf{R}$ is often treated as a diagonal matrix (with $\varepsilon_{\mathrm{RMS}}^2$ sitting on each diagonal entry), where the error in observed shoreline position ($\varepsilon_{\mathrm{RMS}}$) at each transect is assumed to be independent from the error at all other transects, near or far. However, here, with aid of direct estimates of the shoreline error in space (provided by the Ocean Beach data described in Section 2.3), we can account for the spatial correlation of the error using the approach described below.

We compute the (symmetric) observed shoreline error covariance matrix as

$$\mathbf{R}_{i,j} = E\left(\boldsymbol{\varepsilon}_i \boldsymbol{\varepsilon}_j\right) \tag{31}$$

where E is the expected value operator (i.e., the mean, in this case), $\boldsymbol{\varepsilon}_i$ is the time series of the shoreline error at transect i (and likewise for transect j). Although $\mathbf{R}$ (Eq. (31)) can, in general, only be calculated at sites where 'ground-truthed' shoreline observations (e.g., GPS-derived shorelines) are available to assess the error in the satellite-derived shorelines (e.g., Ocean Beach, in this example), we seek to derive and apply a parameterized version of this $\mathbf{R}$ matrix for a broad range of sites lacking in-situ observations. In essence, we seek to understand the spatial decay of the shoreline error covariance. To do so, we calculate the covariance decay as a function of transect proximity (i.e., distance), k, given by

$$r_k = \frac{\text{median}(\text{diag}(\mathbf{R}, k))}{\text{median}(\text{diag}(\mathbf{R},0))} \qquad \text{for } k = 0 : N_{\text{transects}} \tag{32}$$

where r_k is the so-called 'shoreline error covariance decay', which represents how the shoreline error is correlated among nearby transects and becomes increasingly uncorrelated with alongshore distance. In Eq. (32), the $\text{diag}(\mathbf{R}, k)$ operation represents the extraction of the k^{th}-diagonal of the covariance matrix $\mathbf{R}$ (where $\text{diag}(\mathbf{R}, 0)$ is the main diagonal of $\mathbf{R}$). In Figure 17, we fit a smoothed curve (shown in red) of the form

$$\tilde{r}(l) = \left(\exp(-l/\sigma_1) + 0.5\tanh(l/\sigma_2)\right)\exp(-l/\sigma_3) \tag{33}$$

as a function of alongshore distance l to the observed shoreline error covariance decay (shown in blue). Eq. (33) represents the sum of a (rapidly) decaying function (exp) and a plateau function (tanh) that is modulated by another (more slowly) decaying function, parameterized with length scales σ_1, σ_2, and σ_3, with values here of 0.2 km, 0.4 km, and 5 km, respectively.

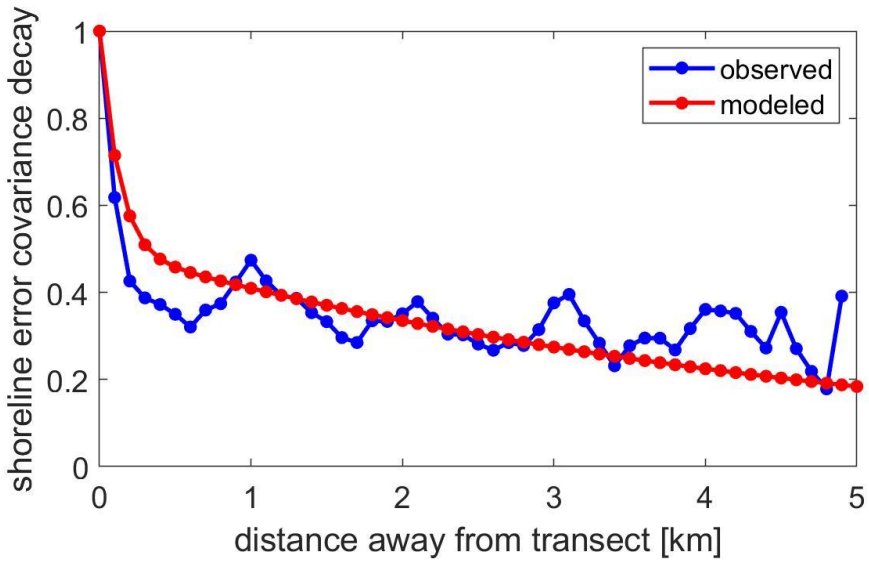

Figure 17 – The variance decay of the shoreline error vs distance away from the transect for the Ocean Beach data (blue) and the parameterized version (red).

As described above, in the current modeling application, in absence of direct, site-specific observations of the error covariance matrix over the entire model domain, we apply the smoothed function $\tilde{r}$ given in Eq. (33) to construct a smoothed error covariance matrix according to

$$\tilde{\mathbf{R}}_{i,j} = \tilde{r}\left(\left|l_i - l_j\right|\right)\varepsilon_{\text{sat}}^2 \tag{34}$$

where $\left|l_i - l_j\right|$ is the absolute value of the distance from transect i to transect j and $\varepsilon_{\text{sat}} = 14$ m is the RMSE of satellite-derived shorelines as reported above.

Appendix C: Model inputs – **future climate and management scenarios**

C.1 Wave modeling

Climate change is expected to drive changes to mean and extreme wave climates in many areas (Morim et al., 2019, 2021), which should ideally be accounted for when predicting long-term coastal evolution. The current shoreline model is forced with a variety of wave hindcast and wave projection products (as depicted in Figure 18 A and B, respectively), according to their spatiotemporal availability. Across the vast majority of the hindcasted period (1995-2020), hindcasted wave conditions (e.g., time series of significant wave height period and direction) come from the California Coastal Data Information Program – CDIP hindcast (O'Reilly et al., 2016), which is coincident with model transects and is available from 2000 to 2020. From 1995-2000, hindcasted wave conditions (Figure 18 A) come from different offshore sources (shown in the superscripts in Figure 18) including (1) the CFSRR-wind driven WW3 hindcast (http://polar.ncep.noaa.gov/waves/hindcasts/nopp-phase2.php), (2) the US Army Corps of Engineers Wave Information Studies (WIS; http://wis.usace.army.mil/), (3) the CaRD10 reanalysis and projection of winds and sea level pressures. (Scripps Institute of Oceanography, University of California at San Diego, 2015), (4) Buoy observations from the National Data Buoy Center (NDBC) site (https://www.ndbc.noaa.gov/), which are downscaled to the coast using look-up tables (5-6: Hegermiller et al., 2016-2017) when the CDIP hindcast (7: O'Reilly et al., 2016) was unavailable. Beyond 2020, the model is driven by projected time series (2020 to 2100) of daily mean wave heights and corresponding wave periods and directions generated from a global-to-regional wave model (WaveWatch III; Erikson et al., 2015, depicted using superscript 8 in Figure 18), which uses wind forcing from the GFDL-ESM2M climate model

(Delworth et al., 2006, depicted with superscript 9 in Figure 18) under the "moderate" representative concentration pathway (RCP) 4.5 emissions scenario (Stocker, 2014). Offshore wave conditions (Figure 18 B) are, once again, downscaled to each shoreline model transect using the look-up-table approach of Hegermiller et al. (2016, 2017).

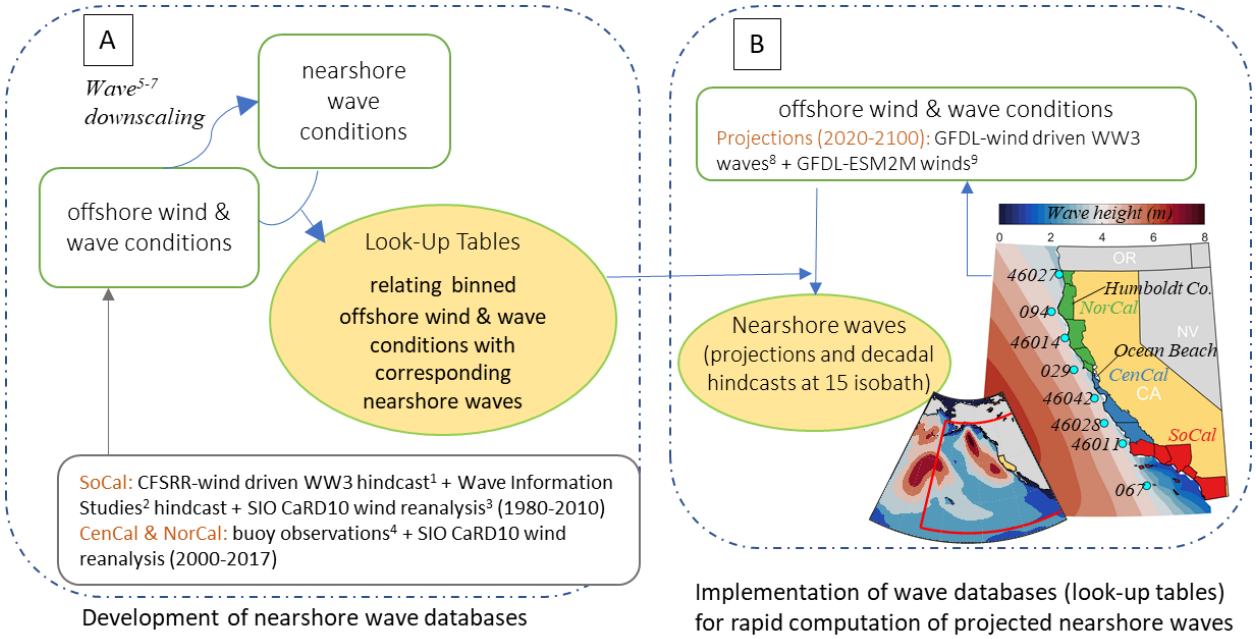

Figure 18 – Overview of the method used to compute nearshore (15 m isobath) wave time-series for the years 2020 to 2100. A) Look-up tables that relate binned offshore wind (magnitude and direction) and wave (height, period, and direction) conditions to nearshore waves were developed by finding corresponding nearshore wave conditions generated from high resolution nearshore wave downscaling models. Downscaling of nearshore wave conditions was achieved with high spatiotemporal resolution SWAN models for southern California and ray tracing techniques for central and northern California (i.e., the CDIP hindcast). B) Implementation of the look-up tables for rapid downscaling of projected offshore wind and wave conditions to the nearshore. Projected offshore wave conditions were derived with the numerical wave model WaveWatch III (NOAA) forced with winds from the GFDL-ESM2M RCP 4.5 climate model. The WaveWatch III model consists of a global and nested regional Eastern North Pacific grid (0.25° resolution; red line shown in inset). Wave buoys used to translate offshore conditions to the nearshore are shown with cyan circles (5- and 3-digit numbers refer to NDBC- and CDIP-owned buoys, respectively. Wave height maps represent a sample time-point from January 10th, 2044.

Accurate hindcasts and projections of nearshore wave conditions are needed in the current application because the model formulations in Eq. (1) are highly sensitive to wave conditions. In particular, anomalies/variations in wave angle and wave energy can significantly affect the calculation of longshore transport (via Eq. (8); e.g., Chataigner et al., 2022) and equilibrium shoreline response (via Eqs. (10) - (11); e.g., Vitousek et al., 2021), respectively. In the current application, the shoreline model is forced with a single projected time series of wave conditions (from Hegermiller et al., 2016). However, this wave forcing time series represents only a single realization of the stochastic wave climate system. Use of an ensemble wave forcing approach (e.g., Davidson, et al. 2017, Cagigal et al., 2020) would likely improve the range of potential short-term shoreline positions and estimates of uncertainty as shown in Vitousek et al. (2021). However, the uncertainty of long-term wave-driven shoreline change (e.g., due to longshore transport) and sea-level rise will still generally be well captured by the 'single realization' approach used here since the long-term processes are driven more by the mean wave climatology rather than the instantaneous weather/wave conditions. Nevertheless, to compensate for not applying ensemble wave conditions, we provide (at each transect location) estimates of intrinsic/aleatoric uncertainty in shoreline position associated with annual, 20-year, and 100-year return period wave events, following Davidson et al. (2017), as demonstrated in Figure 19. The method used here fits a Generalized Extreme Value (GEV) distribution (see Coles et al., 2001) to the annual maxima in the short-term shoreline position, Y_{st} , as shown in the red dots in Figure 19 C and D. 1-year, 20-year, and 100-year erosion events are the estimated from the fitted GEV distribution (purple line in Figure 19 D). Finally, storm-driven erosion uncertainty bands corresponding to 1-year, 20-year, and 100-year erosion event levels are then superimposed onto

the model projections at each transect (as shown in the yellow, red, and brown bands of panel Figure 19 E, respectively).

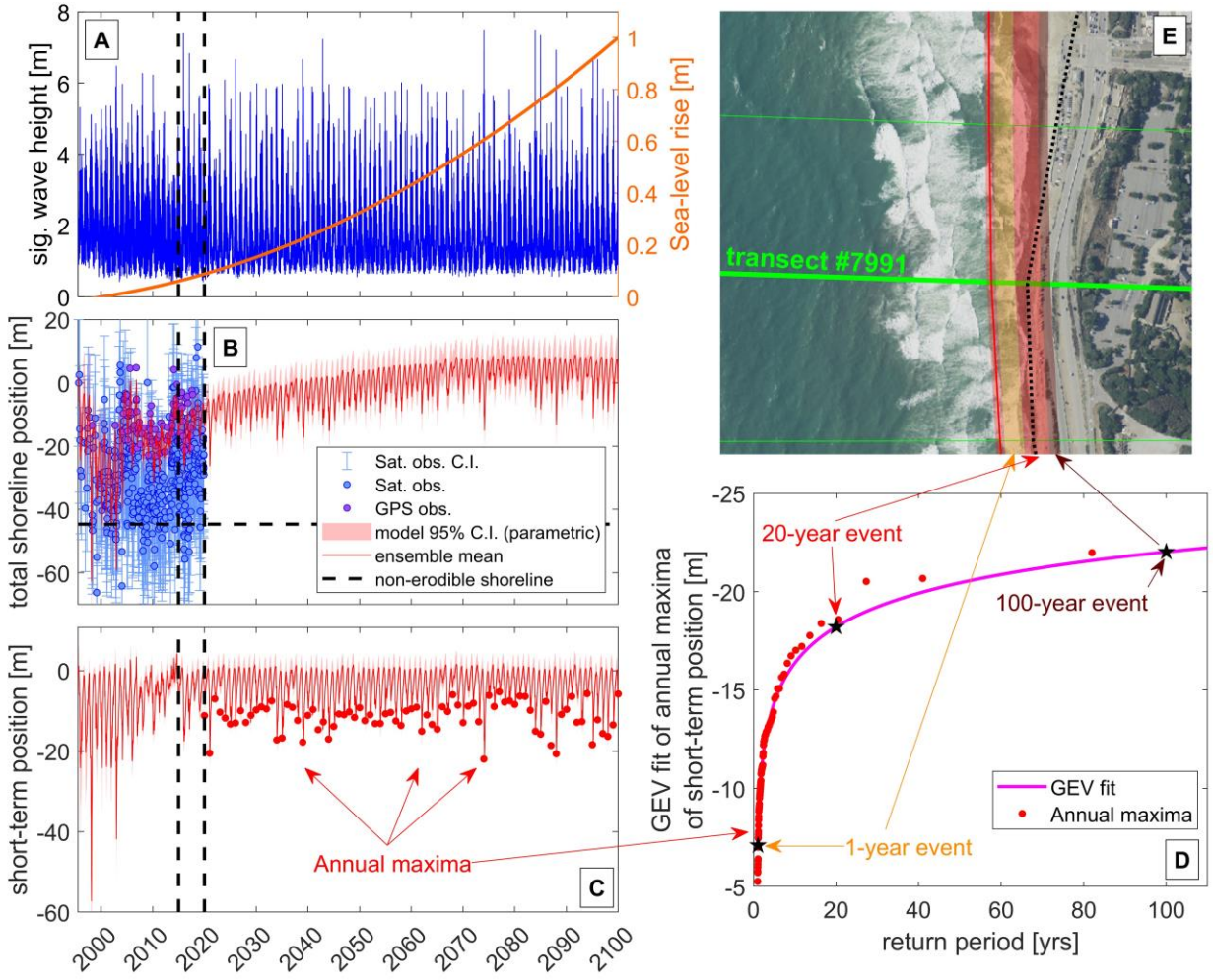

Figure 19 – An example of CoSMoS-COAST simulations of total shoreline position (panel B) and short-term shoreline position (panel C) in response to projected wave and sea-level conditions (panel C) at transect 7991 at Ocean Beach, California. A Generalized Extreme Value (GEV) distribution (purple line in panel D) is fit to the annual maxima in the short-term shoreline position (red dots in panels C and D). 1-year, 20-year, and 100-year erosion events are estimated from the fitted GEV distribution (panel D), and storm-driven erosion uncertainty bands corresponding to these event levels are then mapped onto each transect (as shown in the yellow, red, and brown bands of panel E, respectively). (Basemap is from a current, high-resolution aerial photograph of Ocean Beach available through NOAA Digital Coast).

C.2 Sea-level rise scenarios

The uncertainty of future coastal erosion is intimately linked to sea-level rise (Anderson et al., 2015; Vitousek et al., 2017; Le Cozannet et al., 2019; Vousdoukas et al., 2020; D'Anna et al., 2021a, 2022). In the current application, we consider nine sea-level rise scenarios: 0.5, 0.75, 1.0, 1.25, 1.5, 1.75, 2.0, 2.5, and 3.0 m (shown in Figure 20), which cover the range of physically tenable sea-level outcomes in California over the 21st century (e.g., Griggs et al., 2017, Sweet et al., 2022). The high-end sea-level scenarios, used here, as shown in Figure 20, are consistent with the so-called 'H++' scenario (Sweet et al., 2017), which represent a scenario of extreme ice melt in the West Antarctic ice sheet. As in Vitousek et al. (2017), sea level versus time is modeled as a quadratic function. The three unknown coefficients of the quadratic curve are obtained via three equations: (1) The mean sea level in 2000 is assumed to be at zero elevation, (2) the rate of SLR in 2000 is assumed to be 3 mm/yr, which is consistent with global mean values of sea-level rise observed via satellites, (3) future sea-level elevation at 2100 is assumed to be 0.5, 0.75, 1.0, 1.25, 1.5, 1.75, 2.0, 2.5, or 3.0 m based on the scenarios considered (see Figure 20). We note that, in the current application, sea level only forces equilibrium profile changes via the third term on the right-hand side of Eq. (1), which is in line with many recent studies (Anderson et al., 2015; Vitousek et al., 2017; Le Cozannet et al., 2019; Vousdoukas et al., 2020; D'Anna et al., 2021a, 2022)

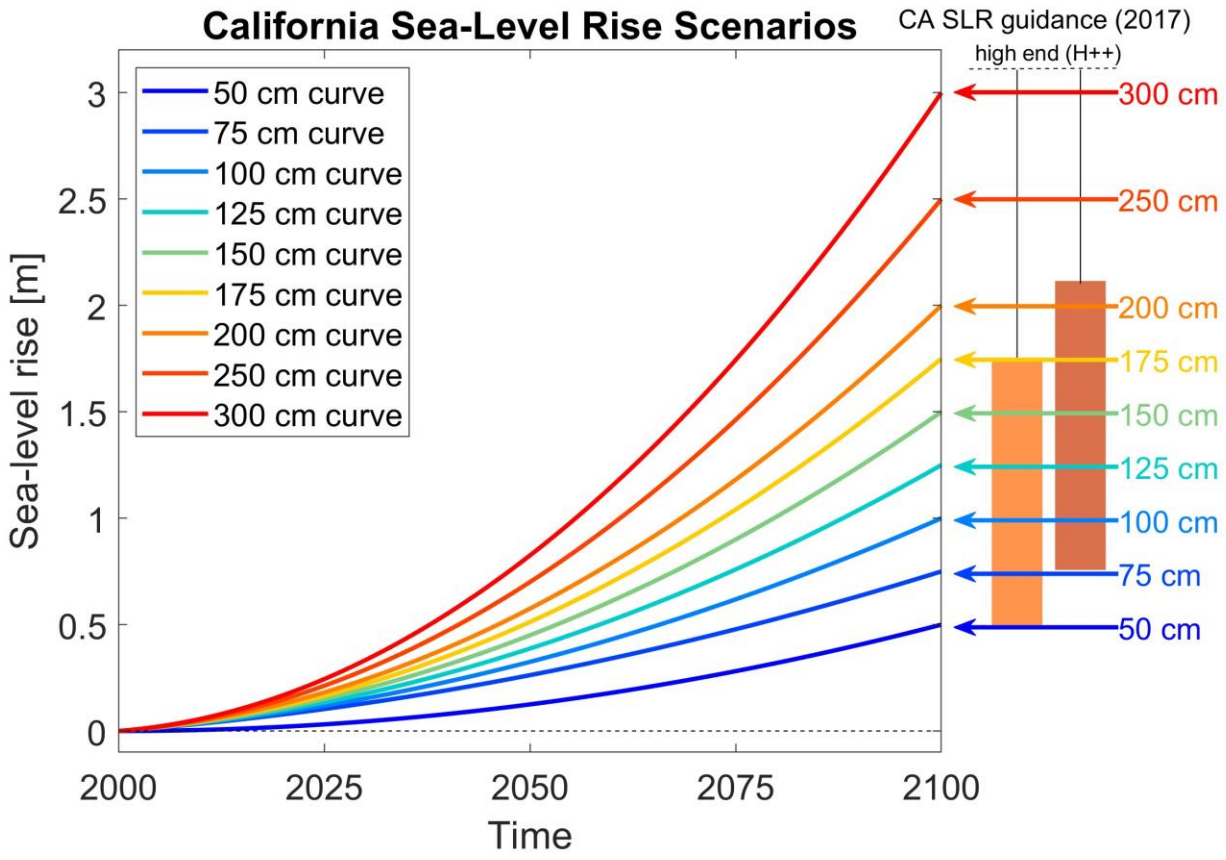

Figure 20 – Scenarios of sea-level rise (i.e., 0.5, 0.75, 1.0, 1.25, 1.5, 1.75, 2.0, 2.5, or 3.0 m) used in the current application, which follow from the California Guidance (Griggs et al., 2017).

C.3 Coastal management scenarios

In this application, we explore the combination of nine sea-level projections (see Figure 20) and four management scenarios. The four management scenarios result from two independent, binary scenarios, namely, "hold the line" and "continued nourishment". The "hold the line" scenario represents the management decision to prevent or allow the shoreline from receding past existing infrastructure (e.g., by permitting or prohibiting shoreline armoring, respectively) or naturally hardened shorelines (e.g., cliffs, bluffs, and headlands). If the line is held, then the modeled shoreline is constrained from eroding past a so-called 'non-erodible shoreline', which is

manually digitized from recent aerial and satellite imagery and represents the division of beach and urban infrastructure, cliffs, or highly vegetated areas (following Vitousek et al., 2017). If the line is not held, then the shoreline is allowed to erode into existing infrastructure and coastal cliffs without impediment as if the eroded substrate is the same as a sandy beach. As in the original CoSMoS-COAST model application (Vitousek et al., 2017), we assume that any dunes or cliffs do not erode landward with the beach, and that the non-erodible shoreline stays fixed through time.

The "continued accretion" scenario represents the management decision to continue or cease the long-term residual shoreline trend (which can be affected by processes such as beach nourishment, fluvial sediment input, and other sources of sediment that contribute to chronic accretion) determined from assimilation of recent historical data (1995-2020). The scenario was previously called "continued nourishment" in Vitousek et al. (2017) when the model domain was limited to southern California, where some nourishment projects have taken place. The current application spans all of California, where nourishments are rare in central and northern California. Hence, the scenario, now referred to as "continued accretion", assumes that both natural (e.g., fluvial) and anthropogenic (e.g., nourishment) accretionary signals will persist or cease. In the model, the "continued accretion" scenario is implemented allowing the data-assimilated value of ν_{lt} to remain unchanged during the forecast period (2020-2100). On the other hand, the "no continued nourishment" scenario forces $\nu_{lt} = 0$ starting in 2020 (at the end of the validation period) for each accreting transect where $\nu_{lt} > 0$. We note that any chronically eroding transects (with $\nu_{lt} < 0$) are held constant at the end of the data-assimilation period, and thus are unaffected by the choice of the "continued accretion" vs "no continued accretion"

scenario. The 9 sea-level scenarios and 4 management scenarios combine to give a total of 36 different models run as part of this effort. For each scenario, we provide time series of expected shoreline change including long-term erosion hazards zone (median projection + 95% confidence intervals for the parametric and structural uncertainty) plus additional storm-driven erosion hazard zones that correspond to annual, 20-year, and 100-year return period wave-driven erosion events. Above, the 'Data availability statement' contains information on where the model-projections, produced as part of this study, can be accessed.

Appendix D: Satellite-derived shoreline error and 'proxy-datum bias'

The so-called 'proxy-datum bias' (Moore et al., 2006; Ruggiero & List, 2009) is a well-known source of error in historical shoreline analyses that combine data sets of both elevation/datum-based surveys (e.g., Lidar/GPS) and visual/proxy-based (e.g., digitized shorelines from aerial photos) shoreline observations. In short, there can often be a slight offset or 'bias' between the two different sources of data, which should ideally be accounted/corrected for. The proxy-datum bias remains poorly understood in the context of satellite derived shoreline observations. Below, we seek to explore the proxy-datum bias of satellite-derived shorelines with the aid of monthly GPS observations at Ocean Beach, California.

Figure 21 shows a histogram of the median error in tide-corrected satellite derived shoreline position (i.e., GPS shoreline position minus the satellite-derived shoreline position) for all Ocean Beach transects as a function of month. Hence, positive values of the error indicate that the satellite-derived shorelines are consistently located farther landward than GPS-derived MSL shoreline contour. We hypothesize that the landward bias of the tide-corrected satellite

observations shown in Figure 21 is due to wave setup (i.e., the persistent increase in nearshore water levels due to wave breaking, which can be corrected for). This hypothesis is supported by comparing the shoreline error (y-axis on the left side of Figure 21) to the median significant wave height (y-axis on the right side of Figure 21, which recorded at the NOAA National Data Buoy Center's San Francisco wave buoy #46026, located 33 km offshore from Ocean Beach). The pink bands on Figure 21 represent the 20th to 80th percentiles of the monthly wave height about the median monthly significant wave height (solid red line). Figure 21 demonstrates that the bias is correlated with wave height: the bias is largest in February when the waves are generally the largest, and conversely, the bias is smallest in August when the waves are generally the smallest.

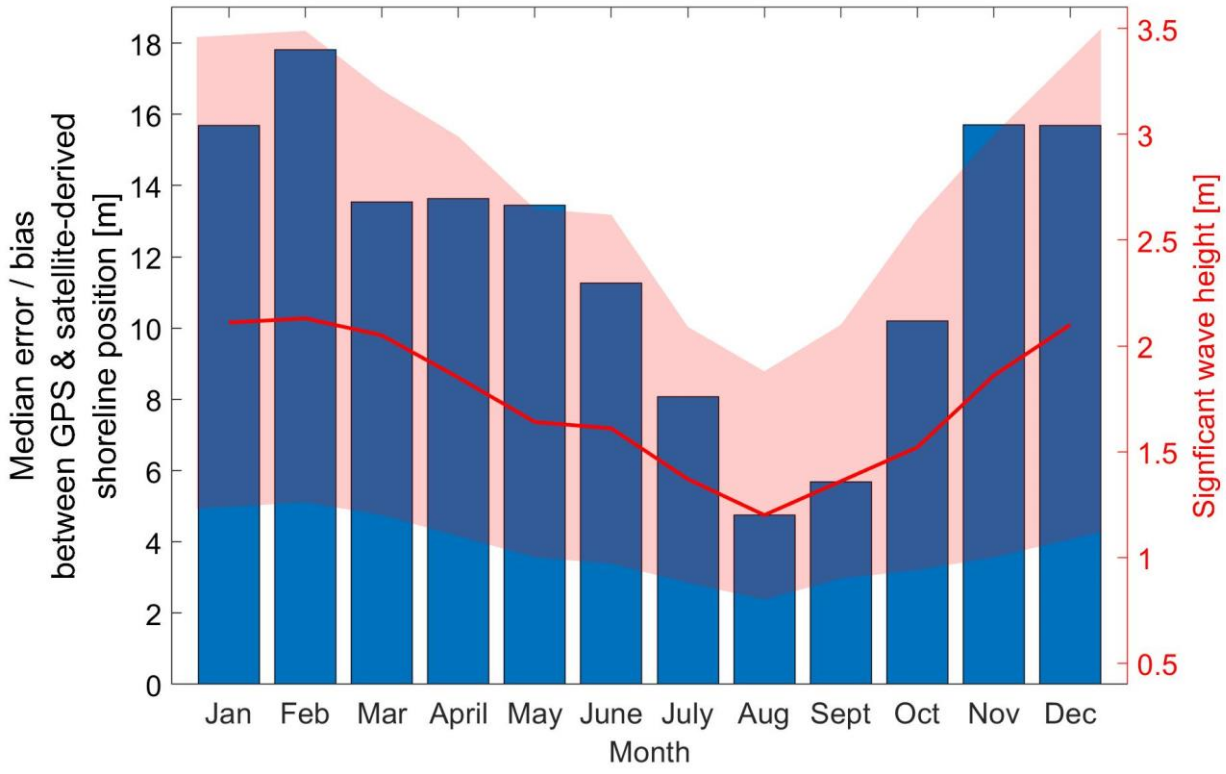

Figure 21 – The error/bias in meters between the GPS surveys and the satellite-derived shoreline position at Ocean Beach, San Francisco, California as a function of month. The median of the monthly significant wave height is shown as a solid red line with the pink envelope representing the 20% to 80% percentiles of the monthly wave height.

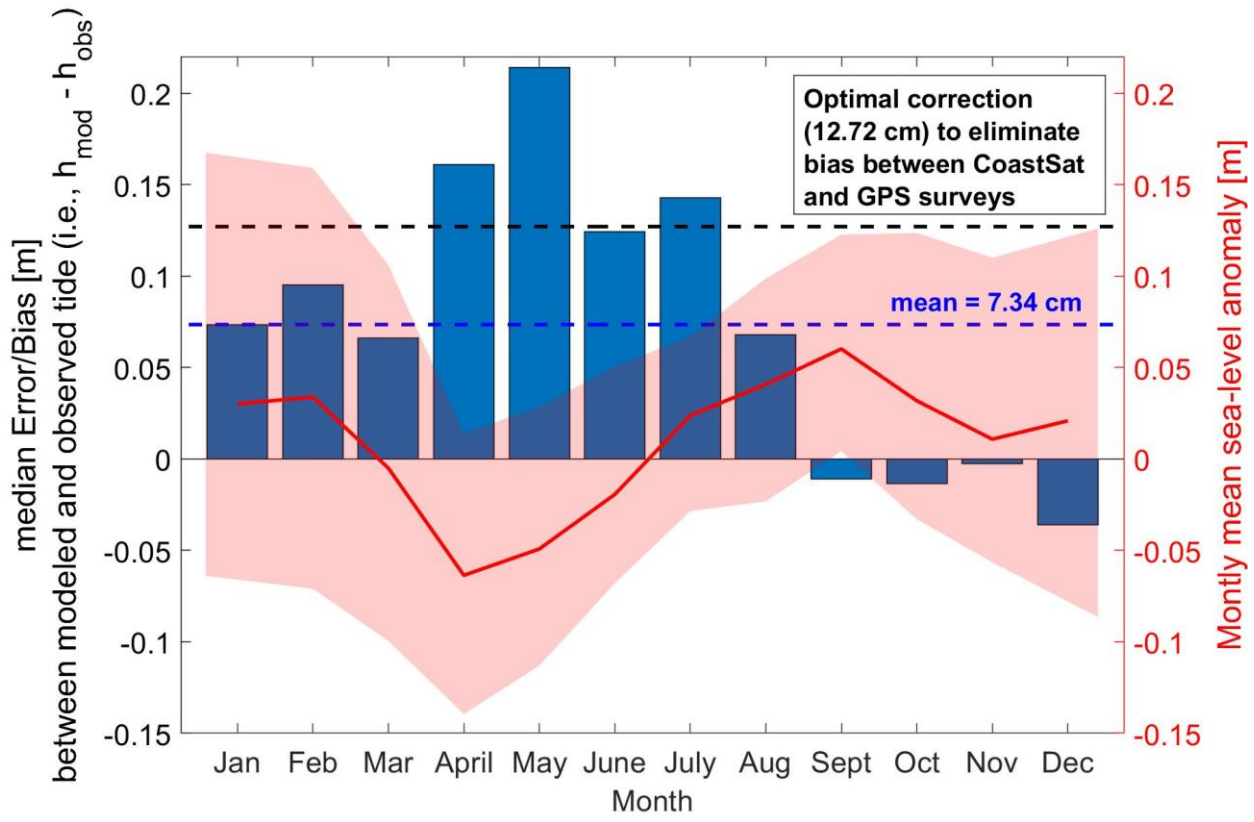

Figure 22 – The median error / bias between the modeled and observed tide at Ocean Beach, San Francisco, California as a function of month (blue bars). The bias is likely due to (negative) monthly mean sea-level anomalies (typically associated with upwelling-favorable winds in spring), shown in red with 80% confidence bands in pink, which are not resolved in the tidal model.

As discussed in Section 2.3, much of the error/bias between (water-level-dependent, proxy-based) satellite derived shorelines and (water-level invariant, datum-based) GPS shorelines can

be attributed to the instantaneous water level. Figure 22 shows the median difference between modeled (using the Finite-Element Solution (FES) ocean model – Lyard et al., 2021) and observed water levels (using the San Francisco tide-gauge station #9414290) near Ocean Beach, San Francisco, California, as a function of month. We also compare the modeled-water-level error (y-axis on the left) to the monthly mean sea-level anomaly (y-axis on the right) on Figure 22, where the pink bands represent the 20 to 80% percentiles of the monthly wave height about the median (solid red line). The mean difference between the modeled and observed water level across all months is 7.34 cm, which is compared to the optimal correction value of 12.72 cm, found in Section 2.3. This indicates that more than half of the proxy-datum bias (after correcting for tide, setup, and monthly-mean sea-level anomalies) of satellite-derived shorelines is likely due to the water-level offset between the modeled and observed water. The difference between modeled and observed water level may be due to dynamic, oceanographic processes (which may be difficult to rectify via modeling) and/or datum issues (which may be easy to rectify via an appropriate, additive constant determined from observations). It is well known (Gill & Clarke, 1974; Schwing, 2000) that upwelling-favorable winds on the California coast during spring and early summer months decrease nearshore sea levels (see red line on Figure 22), which are not resolved in the FES-modeled astronomical tidal predictions and may contribute to the model's over-prediction of spring/summer water levels in Figure 22. It is also possible that the image-processing algorithm that identifies the shoreline (i.e., the division between water and sand) may be slightly biased toward detecting wet sand (i.e., a landward bias) or subaqueous shoreline features (i.e., seaward bias), as is known to occur in certain settings like macrotidal environments (Castelle et al., 2021). However, the relative contributions to the overall bias are difficult, if not impossible, to diagnose in the absence of additional 'ground-truth' observations. Nevertheless,

we find (in Figure 21 and Figure 22) that both waves and water levels play strong roles in the identification of shoreline position in satellite imagery at Ocean Beach. As shown here and in Section 2.3, with the aid of some corrections, we can obtain nearly unbiased estimate of the shoreline position at Ocean Beach from satellite imagery. Further, we can apply these water-level-correction methods more broadly to (presumably) obtain more accurate satellite-derived shoreline observations in otherwise data-deficient locations.

References:

1. Alessio, P., & Keller, E. A. (2020). Short-term patterns and processes of coastal cliff erosion in Santa Barbara, California. *Geomorphology*, *353*, 106994.

2. Alvarez-Cuesta, M., Toimil, A., & Losada, I. J. (2021). Modelling long-term shoreline evolution in highly anthropized coastal areas. Part 1: Model description and validation. Coastal Engineering, 169, 103960.

3. Alvarez-Cuesta, M., Toimil, A., & Losada, Y. I. (2021). Reprint of: Modelling long-term shoreline evolution in highly anthropized coastal areas. Part 2: Assessing the response to climate change. Coastal Engineering, 169, 103985.

4. Anderson, D., Ruggiero, P., Antolínez, J. A., Méndez, F. J., & Allan, J. (2018). A climate index optimized for longshore sediment transport reveals interannual and multidecadal littoral cell rotations. Journal of Geophysical Research: Earth Surface, 123(8), 1958-1981.

5. Anderson, T. R., Fletcher, C. H., Barbee, M. M., Frazer, L. N., & Romine, B. M. (2015). Doubling of coastal erosion under rising sea level by mid-century in Hawaii. Natural Hazards, 78(1), 75-103.

6. Antolínez, José AA; Méndez, Fernando J; Anderson, Dylan; Ruggiero, Peter; Kaminsky, George M; Predicting climate driven coastlines with a simple and efficient multi-scale model. Journal of Geophysical Research: Earth Surface (2019)

7. Armstrong, S. B., & Lazarus, E. D. (2019). Masked shoreline erosion at large spatial scales as a collective effect of beach nourishment. Earth's Future, 7(2), 74-84.

8. Ashton, A., Murray, A. B., & Arnoult, O. (2001). Formation of coastline features by large-scale instabilities induced by high-angle waves. Nature, 414(6861), 296-300.

9. Ashton, A. D., & Murray, A. B. (2006). “High-angle wave instability and emergent shoreline shapes: 1. Modeling of sand waves, flying spits, and capes.” Journal of Geophysical Research: Earth Surface (2003–2012), 111(F4).

10. Bannister, RN; A review of operational methods of variational and ensemble-variational data assimilation. Quarterly Journal of the Royal Meteorological Society. 143 703 607-633 (2017)

11. Banno, M.; Kuriyama, Y.; Hashimoto, N; Equilibrium-based foreshore beach profile change model for long-term data. In The Proceedings of the Coastal Sediments 2015 (2015).

12. Banno, M., Nakamura, S., Kosako, T., Nakagawa, Y., Yanagishima, S. I., & Kuriyama, Y. (2020). Long-Term Observations of Beach Variability at Hasaki, Japan. Journal of Marine Science and Engineering, 8(11), 871.

13. Barnard, P. L., Hansen, J. E., & Erikson, L. H. (2012). Synthesis study of an erosion hot spot, Ocean Beach, California. Journal of Coastal Research, 28(4), 903-922.

14. Barnard, P. L., van Ormondt, M., Erikson, L. H., Eshleman, J., Hapke, C., Ruggiero, P., Adams P. N., & Foxgrover, A. C. (2014). Development of the Coastal Storm Modeling System (CoSMoS) for predicting the impact of storms on high-energy, active-margin coasts. Natural hazards, 74(2), 1095-1125.

15. Bruun, P. (1962). Sea-level rise as a cause of shore erosion. Journal of the Waterways and Harbors division, 88(1), 117-132.

16. Cagigal, L.; Rueda, A.; Anderson, D.; Ruggiero, P.; Merrifield, M. A.; Montaño, J., Coco, G.; Méndez, F. J.; A multivariate, stochastic, climate-based wave emulator for shoreline change modelling. Ocean Modelling, 101695. (2020).

17. Calkoen, F., Luijendijk, A., Rivero, C. R., Kras, E., & Baart, F. (2021). Traditional vs. machine-learning methods for forecasting sandy shoreline evolution using historic satellite-derived shorelines. Remote Sensing, 13(5), 934.

18. Castelle, B., Marieu, V., Bujan, S., Ferreira, S., Parisot, J. P., Capo, S., ... & Chouzenoux, T. (2014). Equilibrium shoreline modelling of a high-energy meso-macrotidal multiple-barred beach. Marine Geology, 347, 85-94.

19. Castelle, B., Masselink, G., Scott, T., Stokes, C., Konstantinou, A., Marieu, V., & Bujan, S. (2021). Satellite-derived shoreline detection at a high-energy meso-macrotidal beach. Geomorphology, 383, 107707.

20. Castelle, B., Ritz, A., Marieu, V., Lerma, A. N., & Vandenhove, M. (2022). Primary drivers of multidecadal spatial and temporal patterns of shoreline change derived from optical satellite imagery. Geomorphology, 108360.

21. Callaghan, David P; Ranasinghe, Roshanka; Roelvink, Dano; Probabilistic estimation of storm erosion using analytical, semi-empirical, and process based storm erosion models. Coastal Engineering 82 64-75(2013)

22. Chataigner, T., Yates, M. L., Le Dantec, N., Harley, M. D., Splinter, K. D., & Goutal, N. (2022). Sensitivity of a one-line longshore shoreline change model to the mean wave direction. Coastal Engineering, 172, 104025.

23. Coastal Data Information Program (CDIP) (2016) Scripps Institution of Oceanography, Integrative Oceanography Division, San Diego, http://cdip.ucsd.edu

24. Coles, S., Bawa, J., Trenner, L., & Dorazio, P. (2001). An introduction to statistical modeling of extreme values (Vol. 208, p. 208). London: Springer.

25. Cooper, J. A. G., & Pilkey, O. H. (2004). Sea-level rise and shoreline retreat: time to abandon the Bruun Rule. Global and planetary change, 43(3), 157-171.

26. Cooper, J. A. G., Masselink, G., Coco, G., Short, A. D., Castelle, B., Rogers, K., ... & Jackson, D. W. T. (2020). Sandy beaches can survive sea-level rise. Nature Climate Change, 10(11), 993-995.

27. Dabees, M. A. (2000). Efficient modeling of beach evolution. PhD Thesis. Queen's University.

28. Davidson-Arnott, R. G. (2005). Conceptual model of the effects of sea level rise on sandy coasts. Journal of Coastal Research, 1166-1172.

29. Davidson-Arnott, R. G., & Bauer, B. O. (2021). Controls on the geomorphic response of beach-dune systems to water level rise. Journal of Great Lakes Research, 47(6), 1594-1612.

30. Davidson, MA; Splinter, KD; Turner, IL; A simple equilibrium model for predicting shoreline change. Coastal Engineering 73 191-202 (2013)

31. Davidson, Mark A; Turner, Ian L; Splinter, Kristen D; Harley, Mitchel D; Annual prediction of shoreline erosion and subsequent recovery. Coastal Engineering 130 14-25 (2017)

32. D'Anna, Maurizio; Idier, Déborah; Castelle, Bruno; Rohmer, Jeremy; Le Cozannet, Goneri; Robinet, Arthur. Impact of model free parameters and sea-level rise uncertainties on 20-years shoreline hindcast: the case of Truc Vert beach (SW France). Earth Surface Processes and Landforms (2020)

33. D'Anna, M., Castelle, B., Idier, D., Rohmer, J., Le Cozannet, G., Thiéblemont, R., & Bricheno, L. (2021a). Uncertainties in Shoreline Projections to 2100 at Truc Vert Beach (France): Role of Sea-Level Rise and Equilibrium Model Assumptions. Journal of Geophysical Research: Earth Surface, 126(8), e2021JF006160.

34. D'Anna, M., Idier, D., Castelle, B., Vitousek, S., & Le Cozannet, G. (2021b). Reinterpreting the Bruun rule in the context of equilibrium shoreline models. Journal of Marine Science and Engineering, 9(9), 974.

35. D'Anna, M., Idier, D., Castelle, B., Rohmer, J., Cagigal, L., & Mendez, F. J. (2022). Effects of stochastic wave forcing on probabilistic equilibrium shoreline response across the 21st century including sea-level rise. Coastal Engineering, 175, 104149.

36. Debreu, L., Marchesiello, P., Penven, P., & Cambon, G. (2012). Two-way nesting in split-explicit ocean models: Algorithms, implementation and validation. Ocean Modelling, 49, 1-21.

37. East, A. E., Stevens, A. W., Ritchie, A. C., Barnard, P. L., Campbell-Swarzenski, P., Collins, B. D., & Conaway, C. H. (2018). A regime shift in sediment export from a coastal watershed during a record wet winter, California: Implications for landscape response to hydroclimatic extremes. Earth Surface Processes and Landforms, 43(12), 2562-2577.

38. Evensen, Geir; Sequential data assimilation with a nonlinear quasi-geostrophic model using Monte Carlo methods to forecast error statistics. Journal of Geophysical Research: Oceans 99 C5 10143-10162. (1994)

39. Flick, R. E. (1993). The myth and reality of southern California beaches. Shore and Beach, 61(3), 3-13.

40. Gill, A. E., & Clarke, A. J. (1974, May). Wind-induced upwelling, coastal currents and sea-level changes. In Deep Sea Research and Oceanographic Abstracts (Vol. 21, No. 5, pp. 325-345). Elsevier.

41. Griggs, G., Patsch, K., Lester, C., & Anderson, R. (2020). Groins, sand retention, and the future of Southern California's beaches. Shore & Beach, 88(2), 14-36.

42. Griggs, G, Árvai, J, Cayan, D, DeConto, R, Fox, J, Fricker, HA, Kopp, RE, Tebaldi, C, Whiteman, EA (California Ocean Protection Council Science Advisory Team Working Group). Rising Seas in California: An Update on Sea-Level Rise Science. California Ocean Science Trust, April 2017

43. Hagenaars, G., Luijendijk, A., de Vries, S., & de Boer, W. (2017). Long term coastline monitoring derived from satellite imagery. In Coastal Dynamics (Vol. 122, pp. 1551-1562).

44. Hamill, T. M., Whitaker, J. S., & Snyder, C. (2001). Distance-dependent filtering of background error covariance estimates in an ensemble Kalman filter. Monthly Weather Review, 129(11), 2776-2790.

45. Hansen, J. E., & Barnard, P. L. (2010). Sub-weekly to interannual variability of a high-energy shoreline. Coastal Engineering, 57(11-12), 959-972.

46. Hapke, C. J., Reid, D., Richmond, B. M., Ruggiero, P., & List, J. (2006). National assessment of shoreline change Part 3: Historical shoreline change and associated coastal land loss along sandy shorelines of the California Coast. US Geological Survey Open File Report, 1219, 27.

47. Hegermiller, Christie A; Erikson, Li H; Barnard, Patrick L; Nearshore waves in Southern California: Hindcast, and modeled historical and 21stcentury projected time series. US Geological Survey summary of methods to accompany data release. (2016)

48. Hegermiller, C.A., et al, 2017, Controls of multi-modal wave conditions in a complex coastal setting: Geophysical Research Letters, https://doi.org/10.1002/2017GL075272.

49. Hersbach, H., Bell, B., Berrisford, P., Hirahara, S., Horányi, A., Muñoz-Sabater, J., ... & Thépaut, J. N. (2020). The ERA5 global reanalysis. Quarterly Journal of the Royal Meteorological Society, 146(730), 1999-2049.

50. Hunt, E., Davidson, M., Steele, E. C., Amies, J. D., Scott, T., & Russell, P. (2023). Shoreline modelling on timescales of days to decades. Cambridge Prisms: Coastal Futures, 1-26.

51. Hurst, M. D., Barkwith, A., Ellis, M. A., Thomas, C. W., & Murray, A. B. (2015). Exploring the sensitivities of crenulate bay shorelines to wave climates using a new vector-based one-line model. Journal of Geophysical Research: Earth Surface.

52. Ibaceta, R., Splinter, K. D., Harley, M. D., & Turner, I. L. (2020). Enhanced coastal shoreline modeling using an ensemble kalman filter to include nonstationarity in future wave climates. Geophysical Research Letters, 47(22), e2020GL090724.

53. Kaergaard, K., & Fredsoe, J. (2013). A numerical shoreline model for shorelines with large curvature. Coastal Engineering, 74, 19-32.

54. Kroon, Anna, Matthieu de Schipper, Pieter van Gelder, and Stefan Aarninkhof. Ranking uncertainty: Wave climate variability versus model uncertainty in probabilistic assessment of coastline change. Coastal Engineering 103673 (2020)

55. Larson, M., & Kraus, N. C. (1994). Temporal and spatial scales of beach profile change, Duck, North Carolina. Marine Geology, 117(1-4), 75-94.

56. Larson, M., Hanson, H. and Kraus, N.C. (1997). Analytical solutions of one-line model for shoreline change near coastal structures. Journal of Waterway, Port, Coastal, and Ocean Engineering 123 (4), 180-191.

57. Lazarus, E. D., & Goldstein, E. B. (2019). Is there a bulldozer in your model?. Journal of Geophysical Research: Earth Surface, 124(3), 696-699.

58. Le Cozannet, G., Bulteau, T., Castelle, B., Ranasinghe, R., Wöppelmann, G., Rohmer, J., ... & Salas-y-Mélia, D. (2019). Quantifying uncertainties of sandy shoreline change projections as sea level rises. Scientific reports, 9(1), 1-11.

59. Lentz, E. E., & Hapke, C. J. (2011). Geologic framework influences on the geomorphology of an anthropogenically modified barrier island: Assessment of dune/beach changes at Fire Island, New York. Geomorphology, 126(1-2), 82-96.

60. Limber, P. W., & Murray, A. B. (2011). Beach and sea-cliff dynamics as a driver of long-term rocky coastline evolution and stability. Geology, 39(12), 1147-1150.

61. Limber, P. W., Barnard, P. L., Vitousek, S., & Erikson, L. H. (2018). A model ensemble for projecting multidecadal coastal cliff retreat during the 21st century. Journal of Geophysical Research: Earth Surface, 123(7), 1566-1589.

62. Long, Joseph W; Plant, Nathaniel G; Extended Kalman Filter framework for forecasting shoreline evolution. Geophysical Research Letters 39 13 (2012)

63. Lorensen, W. E., & Cline, H. E. (1987). Marching cubes: A high resolution 3D surface construction algorithm. *ACM siggraph computer graphics*, *21*(4), 163-169.

64. Ludka, B. C., Guza, R. T., O'Reilly, W. C., Merrifield, M. A., Flick, R. E., Bak, A. S., ... & Boyd, G. (2019). Sixteen years of bathymetry and waves at San Diego beaches. Scientific data, 6(1), 1-13.

65. Lyard, F. H., Allain, D. J., Cancet, M., Carrère, L., & Picot, N. (2021). FES2014 global ocean tide atlas: design and performance. Ocean Science, 17(3), 615-649.

66. Moin, P. (2010). Fundamentals of engineering numerical analysis. Cambridge University Press.

67. Montaño, Jennifer; Coco, Giovanni; Antolinez, Jose A.A; Beuzen, Tomas; Bryan, Karin R.; Cagigal, Laura; Castelle, Bruno; Davidson, Mark; Goldstein, Evan B.; Ibaceta, Raimundo; Idier, Déborah; Ludka, Bonnie; MasoudAnsari, Sina; Mendez, Fernando; Murray, A. Brad; Plant, Nathaniel G.; Ratliff, Katherine; Robinet, Arthur; Rueda, Ana; Senechal, Nadia; Simmons, Joshua; Splinter, Kristen; Stephens, Scott; Townend, Ian; Vitousek, Sean; Vos, Kilian. Blind testing of shoreline evolution models. Scientific Reports 10(1), 1-10. (2020)

68. Moore, L. J., Ruggiero, P., & List, J. H. (2006). Comparing mean high water and high water line shorelines: should proxy-datum offsets be incorporated into shoreline change analysis?. Journal of Coastal Research, 22(4 (224)), 894-905.

69. Morim, J., Hemer, M., Wang, X. L., Cartwright, N., Trenham, C., Semedo, A., ... & Andutta, F. (2019). Robustness and uncertainties in global multivariate wind-wave climate projections. Nature Climate Change, 9(9), 711-718.

70. Morim, J., Vitousek, S., Hemer, M., Reguero, B., Erikson, L., Casas-Prat, M., ... & Timmermans, B. (2021). Global-scale changes to extreme ocean wave events due to anthropogenic warming. Environmental Research Letters, 16(7), 074056.

71. Murray, A. B., Gasparini, N. M., Goldstein, E. B., & Van der Wegen, M. (2016). Uncertainty quantification in modeling earth surface processes: more applicable for some types of models than for others. Computers & Geosciences, 90, 6-16.

72. Nelson, T. R., & Miselis, J. L. (2019). Method For Observing Breach Geomorphic Evolution: Satellite Observation of the Fire Island Wilderness Breach. In Coastal Sediments 2019-Proceedings Of The 9th International Conference (p. 71). World Scientific.

73. O'Reilly, W. C., Olfe, C. B., Thomas, J., Seymour, R. J., & Guza, R. T. (2016). The California coastal wave monitoring and prediction system. Coastal Engineering, 116, 118-132.

74. Otsu, N. (1979). A threshold selection method from gray-level histograms. IEEE transactions on systems, man, and cybernetics, 9(1), 62-66.

75. Pape, L., Kuriyama, Y., & Ruessink, B. G. (2010). Models and scales for cross-shore sandbar migration. Journal of Geophysical Research: Earth Surface, 115(F3).

76. Pardo-Pascual, J. E., Almonacid-Caballer, J., Ruiz, L. A., & Palomar-Vázquez, J. (2012). Automatic extraction of shorelines from Landsat TM and ETM+ multi-temporal images with subpixel precision. Remote Sensing of Environment, 123, 1-11.

77. Pelnard-Considere, R. (1956). Essai de theorie de l'evolution des formes de rivage en plages de sable et de galets. 4th Journees de l'Hydraulique, Les energies de la Mer, Paris, 3(1), 289-298.

78. Sweet, W., Horton, R., Kopp, R., & Romanou, A. (2017). Sea level rise.

79. Turner, I. L., Harley, M. D., Almar, R., & Bergsma, E. W. (2021). Satellite optical imagery in Coastal Engineering. Coastal Engineering, 167, 103919.

80. Ranasinghe, Roshanka; Callaghan, David; Stive, Marcel JF; Estimating coastal recession due to sea level rise: beyond the Bruun rule. Climatic Change 110 4-Mar 561-574 (2012)

81. Ranasinghe, Roshanka. On the need for a new generation of coastal change models for the 21st century. Scientific Reports 10, no. 1 (2020).

82. Reeve, DE; Fleming, CA; A statistical-dynamical method for predicting long term coastal evolution. Coastal Engineering 30 4-Mar 259-280 (1997)

83. Reeve, Dominic E; Karunarathna, Harshinie; Pan, Shunqi; Horrillo-Caraballo, Jose M; Różyński, Grzegorz; Ranasinghe, Roshanka; Data-driven and hybrid coastal morphological prediction methods for mesoscale forecasting. Geomorphology 256 49-67 (2016)

84. Regard, V., Prémaillon, M., Dewez, T. J. B., Carretier, S., Jeandel, C., Godderis, Y., ... & Fabre, S. (2022). Rock coast erosion: an overlooked source of sediments to the ocean. Europe as an example. Earth and Planetary Science Letters, 579, 117356.

85. Robinet, A.; Idier, D.; Castelle, B.; & Marieu, V.; A reduced-complexity shoreline change model combining longshore and cross-shore processes: the LX-Shore model. Environmental modelling & software, 109, 1-16. (2018)

86. Roelvink, Dano; A guide to modeling coastal morphology 12 (2011)

87. Roelvink, D., Huisman, B., Elghandour, A., Ghonim, M., & Reyns, J. (2020). Efficient modeling of complex sandy coastal evolution at monthly to century time scales. Frontiers in Marine Science, 7, 535.

88. Rosati, J. D., Dean, R. G., & Walton, T. L. (2013). The modified Bruun Rule extended for landward transport. Marine Geology, 340, 71-81.

89. Ruggiero, P., Kaminsky, G. M., Gelfenbaum, G., & Cohn, N. (2016). Morphodynamics of prograding beaches: A synthesis of seasonal-to century-scale observations of the Columbia River littoral cell. Marine Geology, 376, 51-68.

90. Ruggiero, P., & List, J. H. (2009). Improving accuracy and statistical reliability of shoreline position and change rate estimates. Journal of Coastal Research, 25(5 (255)), 1069-1081.

91. Ruggiero, Peter; List, Jeff; Hanes, Dan; Eshleman, Jodi; Probabilistic shoreline change modeling. Coastal Engineering 2006: (In 5 Volumes) 3417-3429 (2007)

92. Saha, S., Moorthi, S., Pan, H. L., Wu, X., Wang, J., Nadiga, S., ... & Goldberg, M. (2010). The NCEP climate forecast system reanalysis. Bulletin of the American Meteorological Society, 91(8), 1015-1058.

93. Schwing, F. B. (2000). Record coastal upwelling in the California Current in 1999. CalCOFI Rep., 41, 148-161.

94. Smith, K. E., Terrano, J. F., Pitchford, J. L., & Archer, M. J. (2021). Coastal Wetland Shoreline Change Monitoring: A Comparison of Shorelines from High-Resolution WorldView Satellite Imagery, Aerial Imagery, and Field Surveys. Remote Sensing, 13(15), 3030.

95. Splinter, Kristen D; Turner, Ian L; Davidson, Mark A; Barnard, Patrick; Castelle, Bruno; Oltman-Shay, Joan; A generalized equilibrium model for predicting daily to interannual shoreline response. Journal of Geophysical Research: Earth Surface 119 9 1936-1958 (2014)

96. Sweet, W.V., Hamlington, B.D., Kopp, R.E., Weaver, C.P., Barnard, P.L., Bekaert, D., Brooks, W., Craghan, M., Dusek, G., Frederikse, T., Garner, G., Genz, A.S., Krasting, J.P., Larour, E., Marcy, D., Marra, J.J., Obeysekera, J., Osler, M., Pendleton, M., Roman, D., Schmied, L., Veatch, W., White, K.D., and Zuzak, C., 2022. Global and regional sea level rise scenarios for the United States: updated mean projections and extreme water level probabilities along U.S. coastlines. NOAA Technical Report NOS 01. National Oceanic and Atmospheric Administration, National Ocean Service, Silver Spring, MD, 111 pp., https://oceanservice.noaa.gov/hazards/sealevelrise/noaa-nos-techrpt01-global-regional-SLR-scenarios-US.pdf

97. Taylor, B. N., & Kuyatt, C. E. (1994). Guidelines for evaluating and expressing the uncertainty of NIST measurement results (Vol. 1297). Gaithersburg, MD: US Department of Commerce, Technology Administration, National Institute of Standards and Technology.

98. Toimil, A., Losada, I. J., Camus, P., & Díaz-Simal, P. (2017). Managing coastal erosion under climate change at the regional scale. Coastal Engineering, 128, 106-122.

99. Toimil, A., Camus, P., Losada, I. J., Le Cozannet, G., Nicholls, R. J., Idier, D., & Maspataud, A. (2020a). Climate change-driven coastal erosion modelling in temperate sandy beaches: Methods and uncertainty treatment. Earth-Science Reviews, 202, 103110.

100. Toimil, A., Losada, I. J., Nicholls, R. J., Dalrymple, R. A., & Stive, M. J. (2020b). Addressing the challenges of climate change risks and adaptation in coastal areas: A review. Coastal Engineering, 156, 103611.

101. Toimil, A., Camus, P., Losada, I. J., & Alvarez-Cuesta, M. (2021). Visualising the uncertainty cascade in multi-ensemble probabilistic coastal erosion projections. Frontiers in Marine Science, 8, 683535.

102. Troy, C. D., Cheng, Y. T., Lin, Y. C., & Habib, A. (2021). Rapid lake Michigan shoreline changes revealed by UAV LiDAR surveys. Coastal Engineering, 170, 104008.

103. Turner, I. L., Harley, M. D., Short, A. D., Simmons, J. A., Bracs, M. A., Phillips, M. S., & Splinter, K. D. (2016). A multi-decade dataset of monthly beach profile surveys and inshore wave forcing at Narrabeen, Australia. Scientific data, 3(1), 1-13

104. Turner, I. L., Harley, M. D., Almar, R., & Bergsma, E. W. (2021). Satellite optical imagery in Coastal Engineering. Coastal Engineering, 167, 103919.

105. Vitousek, Sean and Patrick L. Barnard; A nonlinear, implicit one-line model to predict long-term shoreline change. The Proceedings of the Coastal Sediments. (2015).

106. Vitousek, Sean; Barnard, Patrick L; Limber, Patrick; Can beaches survive climate change? Journal of Geophysical Research: Earth Surface 122 4 1060-1067 (2017a)

107. Vitousek, Sean; Barnard, Patrick L; Limber, Patrick; Erikson, Li; Cole, Blake; A model integrating longshore and cross-shore processes for predicting long-term shoreline response to climate change. Journal of Geophysical Research: Earth Surface 122 4 782-806 (2017b)

108. Vitousek, S., Buscombe, D., Vos, K., Barnard, P. L., Ritchie, A. C., & Warrick, J. A. (2023). The future of coastal monitoring through satellite remote sensing. Cambridge Prisms: Coastal Futures, 1, e10.

109. Vitousek, S., Vos, K., Splinter, K., Erikson, L., Barnard, P., & O'Neill, A. Coastal Storm Modeling System coastal change projections (CoSMoS-COAST) for California, (ver. 1): U.S. Geological Survey data release, https://doi.org/xx.xxxx , (2023 - under review) [data set]
(*The data set produced as part of the current under-review paper will be made publicly available on USGS ScienceBase with a valid DOI upon provisional acceptance of this manuscript and subject to USGS internal review protocols. For purposes of peer review only, the provisional data set is currently available here: https://drive.google.com/drive/folders/1FH6IkC7OND55qiNTdf2XlWAyMMOkwvuM?usp=share_link)

110. Vitousek, S. CoSMoS-COAST: The Coastal, One-line, Assimilated, Simulation Tool of the Coastal Storm Modeling System, (ver. 1): U.S. Geological Survey software release, https://doi.org/xx.xxxx , (2023 - under review) [software]
(*The modeling software produced as part of the current under-review paper will be made publicly available on the USGS code.usgs.gov repository with a valid DOI upon provisional acceptance of this manuscript and subject to USGS internal review protocols. For purposes of peer review only, the provisional software is currently available here: https://drive.google.com/drive/folders/1hYCACddm2mVRNHLTssAx4WdytWm1cO3M?usp=share_link)

111. Vos, K., Splinter, K. D., Harley, M. D., Simmons, J. A., & Turner, I. L. (2019a). CoastSat: A Google Earth Engine-enabled Python toolkit to extract shorelines from publicly available satellite imagery. *Environmental Modelling & Software*, *122*, 104528.

112. Vos, K., Harley, M. D., Splinter, K. D., Simmons, J. A., & Turner, I. L. (2019b). Sub-annual to multi-decadal shoreline variability from publicly available satellite imagery. *Coastal Engineering*, *150*, 160-174.

113. Vos, K., Harley, M. D., Splinter, K. D., Walker, A., & Turner, I. L. (2020). Beach slopes from satellite-derived shorelines. *Geophysical Research Letters*, *47*(14), e2020GL088365.

114. Vos, K. (2022). Time-series of shoreline change along the Pacific Rim (v1.3). Zenodo. https://doi.org/10.5281/zenodo.4760144 [data set].

115. Vos, K., Harley, M. D., Turner, I. L., & Splinter, K. D. (2023). Pacific shoreline erosion and accretion patterns controlled by El Niño/Southern Oscillation. *Nature Geoscience*, *16*(2), 140-146.

116. Vousdoukas, M. I., Ranasinghe, R., Mentaschi, L., Plomaritis, T. A., Athanasiou, P., Luijendijk, A., & Feyen, L. (2020). Sandy coastlines under threat of erosion. Nature climate change, 10(3), 260-263.

117. Warrick, J. A., Vos, K., East, A. E., & Vitousek, S. (2022). Fire (plus) flood (equals) beach: coastal response to an exceptional river sediment discharge event. Scientific Reports, 12(1), 3848.

118. Warrick, J. A., East, A. E., & Dow, H. (2023). Fires, floods and other extreme events–How watershed processes under climate change will shape our coastlines. Cambridge Prisms: Coastal Futures, 1, e2.

119. Willmott, C. J. (1981). On the validation of models. Physical geography, 2(2), 184-194.

120. Wright, L. D., & Short, A. D. (1984). Morphodynamic variability of surf zones and beaches: a synthesis. Marine geology, 56(1-4), 93-118.

121. Yates, ML; Guza, RT; O'reilly, WC; Equilibrium shoreline response: Observations and modeling. Journal of Geophysical Research: Oceans 114 C9 (2009)

122. Young, A. P., Guza, R. T., Matsumoto, H., Merrifield, M. A., O'Reilly, W. C., & Swirad, Z. M. (2021). Three years of weekly observations of coastal cliff erosion by waves and rainfall. Geomorphology, 375, 107545.

123. Zarifsanayei, A. R., Antolínez, J. A., Etemad-Shahidi, A., Cartwright, N., & Strauss, D. (2022). A multi-model ensemble to investigate uncertainty in the estimation of wave-driven longshore sediment transport patterns along a non-straight coastline. Coastal Engineering, 173, 104080.